Investigation of Membrane Domains around the B Cell Receptor using Super-Resolution Microscopy

by

Matthew Brossard Stone

A dissertation in partial fulfillment
of the requirements of the degree of
Doctor of Philosophy
(Biophysics)
in the University of Michigan
2016

Doctorial Committee:

Assistant Professor Sarah Veatch, Chair
Assistant Professor Julie S. Biteen
Professor Charles L. Brooks III
Assistant Professor Irina L. Grigorova
Professor Ayyalusamy Ramamoorty

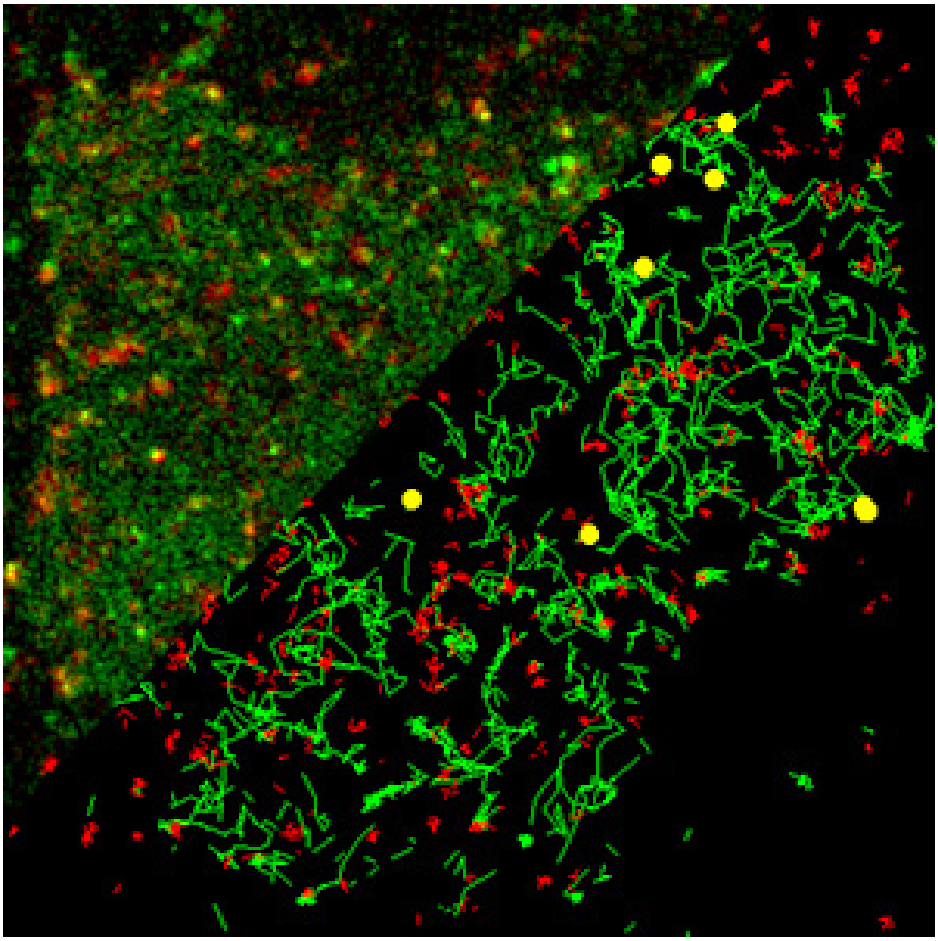

I dedicate this document to my family and friends, especially Carrie Beattie for her tremendous positive impact on my life, my sister Caroline Stone who has always guided me in the right directions, and Ralphie who was always ready to go on a walk with me.

Acknowledgements

Over the past 6 years, I have been lucky enough to be surrounded by many great people who have been fundamentally important to my work. First and foremost, Sarah Veatch has been an amazing leader with keen insight, and I am very grateful for the time and effort that she spent working with me. The postdocs in Sarah's lab have also been extremely helpful; particularly conversations with Sarah Shelby who helped keep me abreast of interesting science, and assistance from Brian DeVree who gave me sage advice for all matters cloning and otherwise. I also thank Jonathan Grover who taught me how to reliably manipulate DNA, his training was solid and was thoroughly tested during multiple cloning projects. The graduate students in Sarah Veatch's lab; Marcos Nunez, Julia Bourg, and Elin Edwald, helped me as collaborators and peers. The lab managers in Sarah's lab, both Jing Wu and Kathleen Wisser, also assisted with many projects. Jing Wu, Sarah Shelby, Kathleen Wisser, and Marcos Nunez helped to gather some of the data in this thesis, and I will always be grateful for their help. I also acknowledge Elly and Erin Gray; collaborating on their highly interesting projects drove me to try new kinds of experiments, and their strong work ethic and excitement pushed my own work in new directions. Experiments with primary cells would not have been possible without Irina Grigorova, who personally helped me to harvest B lymphocytes from a mouse. I also thank Charlie Brooks, Ilya Levental, Akira Ono, Neetu Gupta, Kaushik Choudhuri, and Ben Machta for helpful conversations and their overall support.

Table of Contents

List of Figures

List of Tables

List of Equations

List of Abbreviations

BCR: B cell receptor
Pre-BCR: pre-B cell receptor
IgM: Immunoglobulin type M
IgG: Immunoglobulin type G
ITAM: Immunoreceptor tyrosine-based activation motif
ITIM: Immunoreceptor tyrosine-based inhibition motif
MHC: Major histocompatibility complex
TNF-α: Tumor necrosis factor alpha
BAFF: B cell activating factor
FDC: Follicular dendritic cell
Syk: Spleen tyrosine kinase
SH2: Src homology 2
Blnk: B-cell linker protein
Btk: Bruton's tyrosine kinase
PLCγ2: Phospholipase C gamma 2
PH: Pleckstrin homology
PKC: Protein kinase C
DAG: Diacylglycerol
IP_3: Inositol triphosphate
PIP_2: Phosphatidylinositol 4,5-bisphosphate
ER: Endoplasmic reticulum
SHIP: SH2-containing inositol phosphatase
GPI: Glycosylphosphatidylinositol
CTxB: Cholera Toxin subunit b
LAB: Linker for activation of B cells
LAT: Linker for activation of T cells
GG: Geranylgeranylated peptide bearing a polybasic sequence
PM: Palmitoylated and myristoylated peptide
TM: Transmembrane domain of LAT
TCR: T cell receptor
FRET: Förster resonance energy transfer
PSF: Point spread function
(d)STORM: (Direct) stochastic optical fluctuation microscopy
(f)PALM: (Fluorescence) photoactivation localization microscopy
STED: Stimulated emission depletion
HA: Hemagglutinin
2D: Two dimensional
GUV: Giant unilamellar vesicle
GPMV: Giant plasma membrane vesicle
DC-SIGN: Dendritic Cell-Specific Intercellular adhesion molecule-3-Grabbing Non-integrin
FCS: Fluorescence correlation spectroscopy
MD: Molecular dynamics
L-J: Lennard Jones potential
$f(Ab)_1$: Fragment antibody with only one binding domain

$f(Ab)_2$: Fragment of antibody with two binding domains
PP2: Src kinase inhibitor, 1-tert-Butyl-3-(4-chlorophenyl)-1H-pyrazolo[3,4-d]pyrimidin-4-amine
PDF: Probability density function
MSD: Mean-squared displacement
TIRF: Total internal reflection fluorescence (microscopy)
RAG: Recombination-activating gene
SHIP: SH2 domain-containing inositol-5'-phosphatase
DMPC: Dimyristol phosphatidylcholine
DPPE: Dipalmitoyl phosphoethanolamine
DOPE: Dioleoyl phosphoethanolamine
DPH: 1,6-Diphenyl-1,3,5-hexatriene

List of Appendices

Abstract

B cells are a crucial component of the mammalian adaptive immune system, and the B cell receptor (BCR) has a significant impact on the cellular fate and immunological response of the B cell. When foreign or self-antigens cluster the BCR, tyrosine residues associated with the receptor are phosphorylated by membrane anchored kinases. This process is initiated by an unknown mechanism and results in the activation of multiple signaling cascades. It is hypothesized that antigen bound BCR clusters create a domain of relatively ordered plasma membrane composition, and this domain acts to induce receptor phosphorylation by recruiting Lyn and other kinases. However, it is unclear if domains exist in the cell and unknown if domains could influence the activation state of receptors. The work in this thesis develops methods for quantitatively observing membrane probe partitioning around receptor clusters and provides evidence that a domain of relatively ordered membrane composition is created by clustered B cell receptors. Observations of domain formation show remarkable consistency with a critical fluctuation model for domain formation, and this model also reproduces receptor signal initiation in response to clustering the B cell receptor.

Here, I apply multicolor super-resolution fluorescent microscopy to observe the distribution of membrane anchored probes around B cell receptors, and I demonstrate that a domain of altered membrane composition is present around the receptor clusters. To accomplish this task, I develop quantitative multi-color super-resolution microscopy techniques that report on absolute probe enrichment and depletion which can be performed in live or fixed cells. Applying these techniques to the BCR reveals that simple membrane-bound peptides are sorted around BCR clusters according to their phase preference in model systems. The membrane interacting regions of the phosphatase CD45 and the kinase Lyn are also differentially sorted by domains around BCR clusters, and applying these observations to a simulation containing fluctuating domains reproduces phosphorylation in response to BCR clustering. These results support a

critical fluctuation model for domain formation and suggest that protein clustering may couple to membrane domains to perform a variety of tasks.

Chapter 1: Introduction

The work presented in this Dissertation examines whether a compositionally distinct domain is formed around receptor clusters and provides evidence that B cell receptor signaling may be initiated by membrane domains. In this chapter, I introduce the B cell receptor (BCR) as central to the development of B cells, and I highlight the molecular interplay that regulates B cell receptor signaling. I review evidence that suggests membrane domains impact BCR signaling, and I introduce super-resolution microscopy methodologies that can potentially observe nanoscale membrane compositional heterogeneities. Finally, I introduce the critical fluctuation model which guides the predictions and interpretations of this research.

1.1: B cell development requires a functioning B cell receptor and BCR signaling apparatus

B cells are a central part of the adaptive immune system and the B cell receptor is indispensable for the functioning of B cells. B cells recognize intact antigens in the blood and lymph, internalize and process antigen which is subsequently presented to T cells, and differentiate into antibody producing plasma cells. More than 60 billion B cells attempt to develop from the bone marrow every day of an adults life[1], however, many B cells do not produce an antigen receptor with correct functionality and are culled through apoptosis or anergy, resulting in far fewer mature B cells produced per day. Developing B cells in the bone marrow, referred to as pre-B cells, must pass checkpoints to ensure that the surface-expressed B cell receptor is functional and not auto-reactive[2]. Once a functioning B cell receptor is expressed, the cell can leave the bone marrow as an immature B cell. Immature B cells must also express a B cell receptor that is not auto-reactive or cells will undergo apoptosis. B cells that reach a primary lymphoid follicle from

the marrow and interact with the follicular dendritic cells present in the follicle are then considered mature, and these cells will then search for their antigen mainly in the secondary lymphoid organs such as the lymph nodes and the spleen[3] over a period of 50-100 days[1]. Upon binding an antigen, mature B cells will attempt to present that antigen to T cells, expand their clones in germinal centers, and subsequently differentiate into plasma and other effector cells.

1.1.1: Pro- and pre-B cells are rearranging antigen receptor genes in the bone marrow

B cells are genetically rearranging the B cell receptor gene loci early in B cell development. These genetic rearrangements rely upon the expression of recombination-activating gene (RAG) and other DNA modifying enzymes, and without this machinery B cell development will be halted at early stages. Pro-B cells rearrange their immunoglobulin type M (IgM) heavy chain genes in the bone marrow while interacting with stromal cells through adhesion molecules and growth factors. Once the heavy chain is successfully expressed, the pre-B cell receptor (pre-BCR) is assembled in the endoplasmic reticulum and is expressed on the cell surface. At this point, the B cell has not genetically rearranged the light chain loci of the immunoglobulin, thus the pre-BCR is assembled with a surrogate light chain. Signaling of the pre-BCR complex through the immunoreceptor tyrosine-based activation motifs (ITAMs) of the non-covalently associated heterodimer CD79a and CD79b (CD79a,b) transmembrane proteins allows the developmental progression from pro-B cell to pre-B cell[4]. Pre-BCR signaling is elicited in part through the binding of pre-BCR to stromal cell surface presented galectin-1 which results in a structure similar to the canonical immune-synapse[5], however pre-BCR alone is also able to provide some survival signals to the pre-B cell[6,7] without clustering by extracellular ligand. Small pre-B cells subsequently rearrange their light chain genes. If the genetic rearrangement is successful, fully assembled BCR will be expressed on the cell surface and the cell is referred to as an immature B cell.

1.1.2: Immature B cells undergo negative selection for self-reactive B cell receptors

Transportation of the fully assembled IgM to the cell surface signals gene rearrangement to stop and initiates the immature B cell stage. At this stage, B cells undergo negative selection, also referred to as clonal deletion, in the bone marrow and the peripheral circulation. Glycolipids,

glycoproteins, and proteoglycans found in blood and lymph can act as multivalent antigens. Immature cells that bind these antigens and activate BCR signaling will either undergo receptor editing or apoptosis, depending on where immature cells are located. Autoreactive B cells in the bone marrow may have a second chance to express a receptor that is not self-reactive through genetic editing of the existing light chain[8], or they may undergo apoptosis or become anergic in a process known as central tolerance[9]. Immature B cells that encounter self-antigen outside the bone marrow undergo apoptosis or anergy with no chance of receptor editing in a process referred to as peripheral tolerance[10]. Interestingly, the majority of developing B cells are autoreactive and a large majority of these are selected against by anergy in the immature B cell stage[11]. The removal of these cells by anergy is thought to be important to prevent autoimmunity such as Lupus and type 1 diabetes[12]. A large proportion of developing B cells undergo apoptosis every day due to either autoreactivity or failure to make a functional B cell receptor[1,10].

1.1.3: B cells reach maturity by interacting with follicular dendritic cells

Immature B cells must interact with follicular dendritic cells (FDCs) in secondary lymphoid tissues to avoid apoptosis and anergy and to progress into mature B cells. These secondary lymphoid tissues include the spleen, the lymph nodes, and Payer's patches in the gut. B cells recognize cytokines CCL21 with their CCR7 receptor which leads them into the secondary lymphoid tissues and also acts to coordinate the expression of adhesion molecules specific for peripheral lymphatic tissues. Importantly, cells must interact with follicular dendritic cells in the primary follicle and bind to tumor necrosis factor (TNF-α)[13] and B cell activating factor (BAFF) with their BAFF receptor (BAFF-R)[14] for continued survival, and failure to interact with follicular dendritic cells acts to further cull immature B cell populations. Those B cells that are unable to bind BAFF have an attenuated half-life, whereas patients with non-Hodgkin's lymphoma and the autoimmune disease Sjoegren's syndrome often have overproduction of BAFF which allows B cells to evade apoptosis[15]. Additionally, FDCs contain numerous complement receptors on their surface, which will bind to complement that has been fixed on antigen surface through the complement system in the blood and lymph[13]. FDCs thus serve as repositories of antigens that are being displayed to B cells, and may maximize the potential for the correct B cell to encounter the particular antigen, although this is not necessary for B cells to

become mature. Those B cells that do not immediately recognize their cognate antigen will circulate in the blood and lymph system for 50-100 days until they find their cognate antigen or undergo apoptosis. Interestingly, mature naïve B cells need tonic survival signals that originate from the BCR to continue develop and live[16,17], but potentially not through ITAMs[18], suggesting that a novel type of tonic signaling may drive BCR survival during this time.

1.1.4: Mature B cells proliferate and specialize while interacting with T cells

When mature naïve B cells encounter antigen in the secondary lymphoid organs, they will internalize it, process it, and present antigen fragments on their surface in major histocompatibility complex (MHC) class II proteins. In the lymph nodes, T cells that recognize this MHC bound antigen fragment form an immunogical synapse with B cells and release cytokines and surface ligands, specifically CD40 ligand, that motivate the B cell to divide, forming the primary focus at a separate location in the secondary lymphoid organs[19]. This primary focus gives rise to early but short-lived plasma cells that secrete some IgM which can start to battle an immune challenge faster than the subsequently produced immunoglobulin type G (IgG). Some cells from the primary focus move to primary follicles in the lymph node to become a germinal center. Here, B cells are rapidly dividing, large, and in constant battle with other B cells to maintain contact with a smaller T cell population. These cells are also undergoing somatic hypermutation to create slight variations in their antibody repertoire, and B cells are isotype-switching to create different antibody types such as IgA and IgE. These cells then develop into either antibody secreting plasma cells or memory B cells[1].

1.2: B cell receptors signal in response to antigen

The B cell receptor recognizes intact antigen which can have a very wide distribution of molecular features, valency, and spatial patterns. B cell receptors are thought to signal in response to the clustering of receptors, making their activation independent of the specific nature of the antigen being bound[20]. This requirement can be fulfilled by multivalent antigen in solution or on surfaces, or it can be fulfilled by monovalent antigen displayed on surfaces[21]. Monovalent antigen in solution, however, does not stimulate receptor activation, because it cannot cluster receptors[20]. B cell receptor signaling is propagated by the phosphorylation of

intracellular tyrosine activating motifs (ITAMs) on the CD79a and CD79b heterodimer which is non-covalently associated with the antigen receptor immunoglobulin[22]. Signal propagation is modified by a variety of co-receptors that can communicate specific details about the antigen being encountered, and these modifications may lead to various outcomes for BCR signaling including anergy, apoptosis, and cell activation[23,24].

1.2.1: The propagation of signals from the B cell receptor starts with ITAM phosphorylation

The B cell receptor is assembled in the endoplasmic reticulum where antigen receptor and the signaling subunits CD79a and CD79b are brought together. This association allows for the surface expression of the BCR, which generally refers to the complete assemblage. Once BCR are expressed on the cell surface, receptors can bind and become clustered by antigen, leading to ITAM phosphorylation[25] and downstream signaling. The Src family kinase Lyn is responsible for this initial phosphorylation[26], but it can also be fulfilled by other Src kinases[27]. Lyn binds to the phosphorylated BCR, increasing Lyn's kinase activity[28], which leads to spleen tyrosine kinase (Syk) binding to dually phosphorylated BCR[29,30]. The binding of Syk via tandem Src homology 2 (SH2) domains allows for Syk auto phosphorylation[31] which greatly increases Syk's kinase activity. Syk binding and activation allows the BCR signalosome to assemble via the phosphorylation of B-cell linker protein (Blnk) which initially binds to the BCR via phosphorylated non-ITAM tyrosines[32]. Blnk binding to the activated BCR allows for its phosphorylation by Syk. Phosphorylated Blnk is bound by Bruton's tyrosine kinase (Btk), the Dbl family guanine nucleotide exchange factor Vav 1, and phospholipase C gamma 2 (PLCγ2). These early evens in BCR activation are depicted in **Figure 1**. Btk, Vav1, and PLCγ2 also contain Pleckstrin homology (PH) domains which bind to phosphatidylinositol lipids[33] as well as some proteins such as heterotrimeric G proteins and protein kinase C (PKC)[34]. This signalosome assembly initiates diacylglycerol (DAG) and inositol triphosphate (IP_3) production from phosphatidylinositol 4,5-bisphosphate (PIP_2)[35], leading to calcium release from the endoplasmic reticulum (ER) and subsequently entry of calcium from the extracellular environment into the ER and cytoplasm[36,37]. Subsequent downstream responses are coordinated with other signals from T cell interaction, adhesion molecules, and cytokine receptors to determine B cell action and fate.

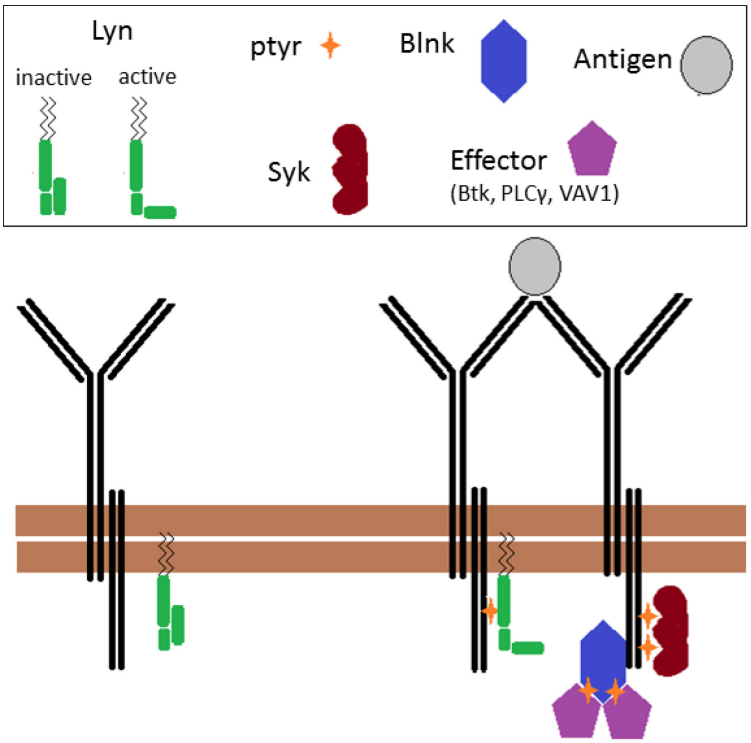

Figure 1: Phosphorylation initiates BCR signalling

BCR is phosphorylated by Lyn kinase. Lyn can then bind to the phosphorylated ITAM of the BCR with its SH2 domain. If an ITAM is phosphorylated twice, Syk can bind and subsequently phosphorylate Blnk which allows effector proteins such as Btk, Vav1, and PLCγ to bind to BCR.

1.2.2: Co-receptors modulate BCR signaling

Co-receptors are an important way for the B cell to determine the type of antigen it is encountering and in what context. FcγRIIb-1 receptors are specifically expressed on B cells and bind to the Fc region or IgG antibodies, however other types of Fc receptors are widespread across other immune cells[38]. When BCR binds an antigen that is already bound by an IgG antibody, it brings the Fc receptor close to the BCR. The close proximity of FcγRIIb-1 to BCR attenuates BCR signaling either by disrupting the membrane around the BCR[39,40] or bringing immunoreceptor tyrosine-based inhibition motif (ITIMs) associated with FcγRIIb-1 close to the BCR[41], recruiting SH2-containing inositol phosphatase (SHIP) which hydrolizes phosphoinositols and prevents the membrane binding of PH domain containing proteins[38]. Genetic deletion or modifications of FcγRIIb leads to autoimmunity diseases of autoreactive

antibodies[42]. Similarly, the co-receptor CD22 also inhibits BCR signals through its ITIM domains. CD22 binds glycosylated proteins, including 2,6 sialic acid, which is present on IgM as well as the transmembrane phosphatase CD45 (also known as PTPRC, Protein Tyrosine Phosphatase Receptor Type C) and the surface of many cells, and acts to inhibit BCR tyrosine phosphorylation and calcium mobilization when expressed in B cells[43].

In contrast, co-receptors can also mediate enhanced stimulation, such as the complement binding CD19 co-receptor, which has been shown to enhance BCR signaling when encountering antigen on surfaces and in solution[44]. In fact, Batista et al showed that CD19 does not need to be co-ligated with BCR in order to be recruited to BCR clusters formed in response to encountering membrane displayed multivalent antigen. Further, the deletion of CD19 severely impacts calcium release, receptor phosphorylation, and recruitment of Syk in response to membrane-bound antigen, but does not impact the response to soluble antigen[44]. Thus, co-receptors can have specific effects on BCR signaling depending on the context antigen is encountered.

1.2.3: The activation state of Lyn and the BCR is highly regulated

CD45 is a transmembrane phosphatase with a large extracellular domain that influences BCR signaling directly and by altering the activation state of Src kinases. CD45 is also known as B220 pan-B cell marker, and isoforms are also expressed in T cells such as CD45RO and CD45RA[45], whereas B cells express the CD45RABC and CD45R isoforms[46]. CD45 has a large glycosylated extracellular domain and two intracellular protein tyrosine phosphatase domains. CD45 can dephosphorylate tyrosine residues on CD79a,b, as evidenced by mixing receptor and phosphate complexes *in vitro*[47] and by co-immunoprecipitation of CD45 and BCR[48]. CD45 can also dephosphorylate both the inhibitory and activating tyrosine of Lyn[49], but does not associate strongly with other Src kinases[48]. Experiments using CD45 deletion or high expression models are difficult to interpret. Batista et al showed that upon deleting CD45 from the A20 human cell, calcium baseline was consistently shifted upwards prior to, during, and after antigen stimulation[44]. CD45 deletions from mice can also result in the inability of BCR to signal[47], but addition of CD45 to 15% of the levels in mature cells results in full recovery of calcium response[47]. In addition, C-terminal Src kinase (Csk) phosphorylates the inhibitory tyrosine of Lyn and other Src kinases, preventing the kinase domain from phosphorylating targets[50]. While

CD45 can regulate the phosphorylation and activation of both the BCR and Src kinases, Csk only phosphorylates Src kinases. These regulatory mechanisms control the activation state of both the receptor and Src kinases.

1.2.4: Clustering is induced by antigen in solution and on surfaces

B cells often encounter antigens presented on membrane surface rather than solution since self-antigens are usually expressed on cell surfaces, and foreign antigen presented to B cells on follicular dendritic cells are also tethered to the follicular dendritic cell plasma membrane. When a B cell encounters antigen on a surface, it spreads out to search for and draw in more antigen, and the B cell subsequently clusters these antigens into a centrally located immune synapse[51]. Immune synapses also allow the transfer of material including antigen[21] and virus[52] between two cells. Interestingly, membrane antigens do not need to be multivalent to induce immune responses, and when BCR encounters monovalent antigen on a fluid membrane it induces receptor phosphorylation[21]. Further, B cell are even more sensitive to membrane bound antigens since a weakly binding antigen presented on a membrane acts to stimulate cells at 3 orders of magnitude lower concentration than in solution[53]. CD45 and other proteins with large extracellular domains are excluded from the membrane synapse, since B cell receptor is highly dense and the tight adhesion between the B cell and the antigen presenting cell act to push out CD45 large transmembrane domain in a process coined "kinetic segregation" [54]. It was also shown that the constant region of the IgM antigen receptor undergoes a conformational change when encountering membrane presented antigens[55], which may help receptors cluster and immobilize after binding to monovalent membrane bound antigen.

1.2.5: The mechanism of BCR signal initiation is unclear

The molecular details leading to phosphorylation of ITAMs on CD79a,b after B cell receptor clustering are not completely understood. The receptor bears no intrinsic kinase and is not associated with Lyn or other kinases in a constitutive manner[22]. It is possible that a transition in the ITAM protein structure could alter the accessibility of ITAMs to kinses in T cells[56,57] and B cells[58,59], however this has not yet been shown to play a role in signal initiation. It has also been postulated that BCRs are clustered and held in an inactive state prior to antigen binding,

whereupon binding antigen allows the release of receptor from this inhibited and clustered state[60], however, this hypothesis does not match other research groups' observations[61]. Finally, it is also hypothesized that BCR clusters alter the local membrane composition, often called "lipid rafts", leading to receptor phosphorylation. This hypothesis will be discussed at greater length in the following section.

1.3: B cell receptor signaling is hypothesized to occur through a membrane domain mediated mechanism

Non-uniform distributions of plasma membrane composition are thought to impact a variety of biological events taking place at the membrane. Composition differences between apical and basal membranes of endothelial cells were identified early on as an important feature of polarized cells[62,63], and membrane compositional heterogeneity was recognized to be feature of other cell types including lymphocytes[64]. Today, compositionally distinct membrane domains are thought to impact a diverse array of biological processes including protein and vesicle trafficking[65,66], immune receptor signaling[67–69], and viral formation and release[70], to name a few. Lipid domains have also been hypothesized to occur in plants[71], bacteria[72], and yeast[73], although the biological implication for membrane domains in plants and microbes is still unclear. A variety of methodologies have been employed to gain knowledge on the nature of membrane domains. In this section, I review fundamental experiments that shed light on lipid rafts and focus on how they impact B cell antigen receptor signaling.

1.3.1: Plasma membrane derived vesicles and cell membrane extracts exhibit compositional heterogeneity

Evidence that the cell membrane can exhibit a spatially heterogeneous composition comes in part from vesicles derived from cellular and purified lipids. Giant unilamellar vesicles (GUVs) composed of a saturated lipid, an unsaturated lipid, and cholesterol can exhibit liquid-ordered liquid-disordered phase coexistence, where the ordered phase is enriched in saturated lipids and has greater amount of acyl chain alignment compared to a disordered phase which is depleted of saturated lipids and has less acyl chain alignment. The transition temperature, the temperature

above which two phases do not coexist, as well as thermodynamic properties such as the correlation length of fluctuations and line tension of phases can be determined from images of vesicles[74,75]. GUVs made from three or more purified lipids have a composition space that can exhibit a solid phase and two liquid phases, either alone or in coexistence, and can also have a miscibility critical point. Interestingly, giant plasma membrane vesicles (GPMVs) harvested from cellular plasma membranes exhibit liquid-ordered and liquid-disordered phase coexistence, suggesting that the plasma membrane of the cell may also be able to exhibit compositional heterogeneity. Vesicles allow the phase partitioning behavior of peptides and membrane components to be determined. For instance, cholera toxin subunit B (CTxB, which binds the ganglioside GM1) partitions into the ordered phase[76], whereas a geranylgeranylated peptide (GG)[76] as well as the transmembrane domain of LAT[65] partitions into the disordered phase in phase separated vesicles. GPMVs are also useful for observing how small molecules[77] and adhesion[78] can alter the phase behavior of the membrane.

The cellular plasma membrane is not always uniform in composition as was suggested by Singer and Nicholson[79]. Non-uniform distributions of membrane composition are observed in the basal and apical membranes of polarized epithelial cells, where biased trafficking and tight junctions enrich NBD-labeled glucosylceramide in the apical membrane by twofold and slightly deplete NBD-labeled sphingomyelin[62,80,81]. It has been hypothesized that apical membrane fractions can be biochemically isolated by Triton-X insolubility, since dissolving the cell plasma membrane with Triton-X detergent does not solubilize viral hemagglutinin[82], ganglioside[83], or glycosylphosphatidylinositol (GPI) anchored proteins and other proteins enriched in the apical membrane[84]. The detergent insolubility of sphingolipids and other selective membrane proteins is unexpected since these hydrophobic proteins and lipids should in theory partition into Triton-X micelles. Detergent insoluble membrane fractions contain important signaling molecules including Src kinases[85], G proteins[86,87], and linker for activation of B[88] and T[89] cells (LAB and LAT). It has been suggested that the insolubility of some proteins in Triton-X is due to favorable interactions between saturated lipids and other membrane components, and the environment around the protein is similar to the liquid-ordered domains observed in synthetic giant unilamellar vesicles[90]. Generally, this evidence supports a theory that certain components of the

plasma membrane are non-uniformly distributed, and suggests they may play a role in biochemical processes happening at the membrane[91].

1.3.2: Literature evidence that BCR signaling involves ordered membrane domains

Ordered membrane domains are thought to play a role in BCR signaling based on evidence that B cell receptor and membrane proteins that regulate the BCR's activation state are insoluble when extracted from plasma membranes with Triton-X detergent. The BCR transitions from detergent soluble to detergent insoluble membrane fractions following the binding of antigen and initiation of BCR signaling[83,92]. This has been interpreted as the BCR partitioning into ordered membrane domains after binding antigen. Additionally, Lyn, the Src kinase that phosphorylates BCR, is also found in detergent insoluble membrane factions, whereas the phosphatase CD45[83,93] and the inhibitory co-receptor CD22[93] have been found to be detergent soluble. The different solubility of these regulatory proteins in Triton-X suggests that ordered domains around BCR clusters may enrich the kinase Lyn and deplete the phosphatase CD45, and thus domains may serve to facilitate phosphorylation of the BCR. After antigen stimulation, phosphorylated BCR and phosphorylated Lyn are heavily enriched in insoluble fractions[83], supporting the idea that domains act to facilitate BCR phosphorylation. Additionally, antigen-bound BCR is found in the detergent resistant fraction even in the absence of receptor phosphorylation by Src kinases or when actin is perturbed[94], indicating that ordered domain formation is largely independent of BCR signaling, and could thus serve as an initiator of phosphorylation.

The detergent resistance of BCR and co-receptors may indicate that ordered membrane domains play a role in regulating the inhibition and regulation of BCR signaling. FcγRIIb is detergent insoluble under normal conditions, and colligation of FcγRIIb with the BCR does not alter the detergent resistance of either protein[95], indicating that the membrane around both may be relatively ordered under normal conditions. However, FcγRIIb transmembrane domain polymorphisms associated with Lupus are more detergent soluble and do not inhibit BCR signaling as does wild type[96], and mutant FcγRIIb is not phosphorylated after being clustered, unlike wild type[97], which can be interpreted to mean that the ordered domain partitioning of FcγRIIb is necessary for its phosphorylation and thus inhibition of potentially autoreactive B cells. In addition, Lupus patients have an isoform of CD45 that is present in detergent insoluble

membrane fractions and is retained at the immune synapse[98], further suggesting that altered partitioning of regulatory proteins into membrane domains is a feature of Lupus.

Developmental stages of B cells also have distinct BCR raft partitioning. A large fraction of pre-BCR is detergent insoluble prior to BCR clustering, in contrast to the mature B cell receptor which is not detergent insoluble until after BCR clustering[99]. This increased insolubility was hypothesized to assist the small number of pre-BCR in eliciting cellular activation following initial surface expression. Additionally, BCR from tolerant B cells does not become detergent insoluble after antigen binding, perhaps explaining why BCR clustering does not cause signaling responses in these cells[93]. These results suggest that the membrane environment around the B cell receptor may be used to make BCR more or less excitable, and may be used to control B cell activation at different points in B cell's lifecycle.

These experiments support that B cell receptor is associated with a different plasma membrane composition following antigen clustering; however, investigating membrane domains using detergent solubility has been largely discounted. Triton-X can induce large scale changes in plasma membrane morphology[100,101], and experiments must be performed at 4^{o}C, which may not reflect the structure of the plasma membrane at physiological temperatures[102]. Despite these limitations, this work has helped to lay a foundation for the study of membrane domains and lipid rafts in B cells, and indicate that membrane structure may be important for the initiation and regulation of signaling through the B cell receptor[67].

1.3.3: Biophysical methods support that the B cell membrane composition is heterogeneously distributed

Cholera toxin B (CTxB) membrane binding is used to reveal the locations of ordered membrane in the cell since CTxB partitions into the ordered phase of GPMVs and GUVs, and co-localization between CTxB and another protein can indicate that proteins are in an ordered membrane domain. Fluorescence co-localization between the BCR and CTxB indicates capped and internalized BCR is surrounded by relatively ordered membrane. The actin network acts to cluster BCR bound to antigen, resulting in a "capped" distribution of BCR when encountering soluble antigen[103]. Capped BCR is spatially correlated with CTxB[104] as well as the filipin

labeled cholesterol[105], suggesting that the membrane composition around receptor clusters is relatively ordered. Additionally, CTxB is internalized with BCR following antigen binding, which may indicate that ordered membrane domains play a role in the internalization and trafficking of BCR[83]. These results suggest that BCR is co-localized with ordered membrane domains at long times after antigen stimulation and during receptor internalization.

Förster resonance energy transfer (FRET) has been used to examine the immediate plasma membrane environment around the BCR and order preferring probes. FRET utilizes energy transfer between two fluorophores which occurs on a very small length scale, generally less than 10 nm[106]. FRET between two fluorescently labeled proteins in the cell, one of which that has a known preferential partitioning into order or disordered phases can be used to infer local membrane composition changes around a protein of interest[107,108]. In this way, FRET between the BCR and a membrane probe with ordered phase partitioning can be used to observe changes in BCR proximal membrane composition during antigen stimulation[109,110]. After clustering BCR with soluble antigen, FRET increased between BCR and an order preferring palmitoylated and myrisotylated peptide (PM). Increased FRET between BCR and PM occurs for about 1-minute post stimulation, slightly longer than the intracellular calcium spike observed with Fluo-4, however there is no increase in FRET between the BCR and either a myristolated or geranylgaranylated peptide after stimulation. Interestingly, FRET between BCR and PM is also prolonged by co-ligation with CD19[110], indicating that clustering of BCR due to binding soluble antigen create an ordered domain that is enhanced by the presence of CD19.

FRET between BCR and PM is also transiently increased when BCR is clustered by a membrane bound antigen in a supported bilayer, a system that mimics the B cell encountering tethered antigen on the surface of another cell. Increased FRET between BCR and PM following antigen binding is also observed after treatment with a kinase inhibitor (PP2) or an actin polymerization inhibitor (latrunculin). FRET between the PM probe and the BCR peaks around 40 seconds after antigen encounter, whereas the FRET between BCR and Lyn peaks around 2 minutes after antigen encounter[109], which may reflect the longer timescale for Lyn binding to BCR in this system compared to the time it takes for the BCR clusters to stabilize an altered membrane environment. These results indicate that the membrane around nascent BCR clusters is enriched

in PM and therefore Lyn, however these results are an indirect measure of local composition and are less sensitive to the depletion of composition around receptor clusters. **Table 1** reviews the evidence that ordered domains exist around BCR, and provides a short description of the results that suggest ordered domains exist around BCR.

Table 1: Evidence that ordered domains exist around BCR

TECHNIQUE	OBSERVATION	REFERENCE
CO-CAPPING WITH BCR	Fillipin is co-capped with BCR	105
	CTxB is co-capped with BCR	104
FRET BETWEEN BCR AND PM	Soluble Ag increases BCR-PM FRET in a PP2 and latrunculin independent manner	110
	Membrane Ag increases BCR-PM FRET, for Lyn-BCR FRET in presence of PP2	109
DETERGENT RESISTANCE	BCR + Lyn are detergent resistant	83,92
	CD45 is detergent soluble	83,93
	CD22 is detergent soluble	93
	FcγRIIb is detergent resistant	95

1.4: Super resolution microscopy methods are an important tool for the study of membrane domains

Super resolution microscopy is a useful tool for observing small sized and low contrast cellular features such as membrane domains. Membrane domains in resting cells cannot be observed directly with fluorescence microscopy, and are thought to be smaller than the diffraction limit of

light[111]. Additionally, membrane composition heterogeneities in resting cells are thought to be very transient, making them difficult to directly observe[112]. Microscopic-scale composition heterogeneity is generally only seen in specialized cell types such as the epithelial layers, however, sub-microscopic composition fluctuations are hypothesized to be a feature of many cell types. Microscopy techniques that provide resolution beyond the diffraction limit are thus an important method for observing evidence for membrane domains; either through the altered diffusion of probes or spatial distributions of probes within membrane domains. In this section, I will introduce super-resolution techniques and also review where they have been applied in the study of membrane domains in cells. This section focuses on the use of point-based super-resolution microscopy techniques to examine protein clustering, as well as particle tracking and STED microscopy techniques to examine membrane protein and lipid diffusion.

1.4.1: An introduction to single molecule and super-resolution microscopy methods

Fluorescence microscopy allows the subcellular location of many fluorescently-tagged biomolecules to be directly visualized at once and is thus very useful for understanding cellular and molecular behavior. The sub-diffraction location and dynamics of single fluorescent molecules can be determined, either by observing individual fluorescent molecules at one time or by exciting only a very small volume. Single molecule tracking experiments tag a small subset of proteins with very bright and photostable fluorophores such that when excited, individual fluorophores can be seen[113–115]. The intensity pattern of individual fluorophores is an Airy disk due to diffraction of light waves as they travel through the circular objective aperture and into the far-field. The observed intensity pattern of single fluorophores is referred to as the point spread function (PSF). This PSF can be fit by a function that approximates an Airy disk, generally a Gaussian is used, and the center of this Gaussian is an estimate of a fluorescent particle's center, referred to as a localization[116]. The standard deviation of a localization improves upon the original PSF standard deviation by a factor of $\frac{1}{\sqrt{N}}$, where N is the number of photons observed for a single PSF[117]. Thus, by collecting many fluorophores in a single PSF, the location of a spatially isolated fluorescently tagged protein can be known with very high precision, generally with resolutions of 20-50 nanometers.

The point-localization based super-resolution microscopy techniques (direct) stochastic optical reconstruction microscopy, (d)STORM[118,119], and (fluorescence) photoactivation localization microscopy, (f)PALM[120,121], observe single fluorescent molecules at a time to afford better resolution than the diffraction limit. These techniques stochastically switch dyes between fluorescent and non-fluorescent states, allowing sampling of many molecular positions. Density is controlled such that only a small subset of a large pool of fluorescently labeled targets are observed at one time so that fluorophores are spatially distinct from one another and can be fit by approximations to the PSF. Stochastic sampling over some time allows the positions of many labeled targets to be determined at resolutions greater than the original fluorophore PSF. For organic fluorophores, this is referred to as (d)STORM, and often involves the use of special buffers to help the majority of fluorophores achieve a transient and reversible dark triplet state[122,123]. A similar routine can be performed with photoactivatable fluorescent proteins[124], where the technique is referred to as PALM, and a small subset of photoactivatable fluorescent proteins are activated at a time such that individual fluorophores can be observed and fit by approximations to the PSF[120,121]. These techniques can be used to determine the spatial distribution of proteins in live and fixed cells, which reveals previously unresolvable structures, such as the periodic actin structure in neuronal axons[125] or the distribution of proteins around nascent viral capsids[126].

Stimulated emission depletion (STED) microscopy[127,128] can also be used to achieve high spatial resolution. In this technique, the fluorescence of molecules is spatially controlled by simultaneously exciting fluorophores into the excited state, as well as stimulating emission from the fluorophore. Stimulated emission photons are matched in wavelength to the wavelength of the STED beam, and this wavelength is discarded, creating a tunable depleted area that is not visible[127]. The laser that stimulates emission (STED beam) is patterned in such a way so that there is a minimum in one or more[129] very small spots. This results in fluorescence being observed only from the very small minima that are present in the STED beam, allowing for extremely small excitation volumes to be created. This technique can be used to observe the sub-diffraction distribution of proteins and labeled molecules in cells[130], and can also be used to create a very small excitation volume that fluorescently labeled molecules can diffuse in and out

of[131], in a similar fashion as fluorescence correlation spectroscopy (FCS), except that the size of the excitation volume is not diffraction limited in the case of STED.

1.4.2: Point localization based super-resolution microscopy can measure the clustering and co-clustering of membrane components

Point localization based super-resolution microscopy methods such as STORM and PALM can be used to determine the nanoscale clustering of membrane probes and their co-localization with other membrane probes. Strong protein domain partitioning in heterogeneous membranes is thought to result in confined diffusion within domains and an observed clustered distribution since proteins should be enriched in domains[90]. Influenza hemagglutinin (HA), an outer capsid protein that mediates viral entry which has been previously shown to exhibit detergent insolubility[132] was shown to be clustered and exhibit anomalous diffusion[133]. The clustering of palmitoylated and mutant LAT was also assayed with PALM, and unexpectedly showed that mutant LAT that did not contain palmitoyl groups was more clustered than wild type LAT[134]. Since palmitoylations generally drive proteins into ordered membrane domains[135], this result may indicate that protein-protein interaction between transmembrane domains drives observed clustering. Similar methods were applied to the N-terminal domains of Src and Lck, two kinases which are anchored to the plasma membrane through either two palmitoylations and one myristoylation (Lck) or with one myristoylation (Src). The partitioning of Lck into ordered domains is predicted to be higher than Src due to the greater number of palmitoylations it bears. Clusters of Lck around 50 nm in radius were apparent, in support of the notion that strong partitioning into domains leads to clustering[136]. The clustering of HA has been reproduced by another group, however question remain regarding the mechanism for HA clustering[137]. It should be noted that over-counting and reversible photoactivation of probes skews point-based super-resolution microscopy measurements towards observing apparent clusters, even in monodisperse samples[138]. This effect can be filtered out[139], however, it is unreliable and often the point spread function of the overcounting peak (generally the resolution of the experiment) is close to the size of the structure in question (20-100 nm). Additionally, the expected amount of clustering of ordered-domain preferring membrane components may be small since domains are

thought to coalesce and stabilize only after clustering from protein-protein interactions during biological events[112].

1.4.3: Single molecule tracking can capture transient confinement

High speed, high precision tracking of membrane probes having different phase partitioning suggests that in some cases ordered phase preferring proteins and lipids tend to be confined to a greater degree. Many of these experiments utilize probes chemically conjugated to lipids that are enriched in the ordered phase of GUVs and GPMVs such as 1,2-dipalmitoyl-sn-glycero-3-phosphoethanolamine (DPPE), and the ganglioside GM1; and these studies often also use lipids that are enriched in the disordered phase of GUVs and GPMVs such as 1,2-dioleoyl-sn-glycero-3-phosphoethanolamine (DOPE) as comparison. Trajectories from proteins or lipids tracked at very high speeds can exhibit a short length scale confinement termed hop diffusion; proteins or lipids will sample one area in space and then move, or hop, to another region. For instance, Kusumi et al found that DOPE lipids labeled with a colloidal gold molecule tracked at extremely fast rates exhibited hop diffusion in the plasma membrane of live cells. This partial confinement in an estimated 250 nm area was attributed to the actin and other cytoskeleton, since the confinement area was increased by perturbing actin polymerization and was not evident in vesicles isolated from cells or in vesicles prepared form purified lipids[140]. Gold labeled GPI-linked protein Thy-1 and gold labeled GM1 were confined to a greater degree than DOPE and DPPE, suggesting that this confinement was somehow linked to the detergent resistant fractions of membrane isolate which were defined by their enrichment in GPI linked proteins and GM1[141]. These experiments must be carefully controlled to ensure that probes are not multivalently attached to single gold molecules, which could result in complex diffusion due to the binding of multiple targets[142]. Overall, these results provide further indication that the plasma membrane is not uniform, and suggest that cytoskeleton elements as well as membrane domains may restrict the diffusion of components in the plasma membrane.

1.4.4: STED and FCS observe the diffusion of ordered-domain partitioning probes

Ordered membrane components also exhibit confined diffusion as seen by their transit times through very small excitation volumes. Stimulated emission depletion (STED) microscopy[127]

uses a depletion laser to prevent observations of fluorophores outside of a very small spot. This technique can be used in live cells to create extremely small excitation volumes through which molecules can diffuse and transit times can be determined in a similar manner as traditional FCS. Anomalous diffusion of sphingomyelin was detected with both STED[143,144] as well as advanced FCS[145] with three detectors to better spatially resolve trajectory positions. By varying the intensity of the STED depletion laser, the effective spot size can be fined tuned, allowing the lipid and proteins transit time to be examined for a range of excitation areas[131]. These studies conclude that the diffusion of sphingomyelin as well as GPI linked proteins is confined within an area of less than 20 nm in diameter, and the confinement of sphingomyelin is reduced after treatment with sphingomyelinase[143,145], or cholesterol oxidase[130]. Interestingly, the magnitude of ordered phase partitioning of fluorescently labeled lipids and membrane proteins does not change their apparent confinement in a small 1000 nm^2 area[144], indicating that there are interactions besides phase partitioning drives the confinement of some membrane components.

1.5: Membrane domains need additional characterization

1.5.1: The existence of domains in cells is still debated due to a lock of direct evidence

Fundamental questions about domains have not been addressed, and even the existence of compositionally distinct domains and their potential role in membrane biology is debated. This is due in part to a lack of direct evidence of small-scale compositional heterogeneity in cells. The confined diffusion of ordered-preferring membrane anchors is suggestive of ordered membrane domains existing in cells[144], however, the ultimate cause of this confinement has yet to be shown. Additionally, detergent resistance is suggestive of stronger associations between some membrane components[91], but results from these experiments may be driven by other hidden variables as well[100,101]. FRET between liquid-ordered favoring membrane probes is also suggestive of preferential interactions between some components[110,146], although it is difficult to know the absolute enrichment or depletion in these experiments[106]. Finally, point localization-based methods have thus far been focused on detection of membrane component clustering, which is complicated by the potential overcounting of individual fluorphores[138]. Thus, it has yet to be shown whether ordered-disordered compositional coexistence is a feature of cells or how

much domains could theoretically influence the spatial distributions and activation states of proteins.

1.5.2: A critical fluctuation model for the plasma membrane

The cellular membrane could form domains in the absence of large scale phase separation by tuning its plasma membrane composition near a critical point for liquid-ordered and liquid-disordered phase miscibility[74,147,148]. Membranes isolated from the cell plasma membrane exhibit critical fluctuations that quantitatively agree with the correlation length and boundary shape of the expectations from a two-dimensional (2D) critical fluid[74]. The near critical system has a high susceptibility, thus a small amount of energy applied to the near-critical membrane can alter its composition[149,150]. For biological membranes, this applied energy might come in the form of clustering a component, such as a protein, that couples to one or the other phase, and clustering of a phase preferring protein would lead to the stabilization of an ordered or disordered domain around the clustered protein in a near-critical membrane. Thus, proximity to a critical point may allow biological responses to clustering stimuli by reducing the energy cost for forming a domain.

We will use the critical Ising model to guide the interpretations and expectations of critical membrane systems. The two dimensional Ising model is an excellent model for critical membrane systems, is solved analytically[151], and only depends on a few variables such as temperature and interaction strength between neighboring components. The effects of enforcing specific spatial configurations of ordered or disordered components can also be investigated, such as pinning a component to the cytoskeleton[152] and the shape of membrane inclusions[150]. Although cell membrane derived vesicles exhibit critical phenomena, it is unclear whether the intact and live cell membrane also behaves as a critical fluid. The work in Chapter 3 uses insights from the Ising model to guide experiments examining the existence of ordered domains in the B cell plasma membrane.

1.5.3: This work applies multicolor super-resolution microscopy co-localization to the B cell receptor and simple membrane probes

Here, we directly show that the membrane around B cell receptor clusters stabilizes an altered composition consistent with the liquid-ordered domain around the receptor clusters. We develop super-resolution microscopy techniques to quantitatively measure distance dependent density changes of fluorescently tagged membrane probes around the B cell receptor in both live and fixed cells. This experiment is quantitative meaning that we observe the absolute value of enrichment or depletion of membrane probes around the BCR. We utilize this technical advance to observe the distance dependent concentration of various ordered and disordered preferring membrane anchors around the B cell receptor clusters, and we find that B cell receptor clusters are enriched in ordered-favoring probes and depleted of disordered-favoring probes in fixed and live cells. This ordered domain sorts proteins involved in the regulation of B cell receptor phosphorylation, and we show that the formation of a domain alone may be sufficient to stimulate the receptor. Overall, our results fill a critical gap in existing knowledge by directly showing that non-uniform distributions of membrane composition can indeed exist in the cell and can function in regulating the spatial distribution of proteins that regulate signaling processes at the plasma membrane.

Chapter 2: Far-red organic fluorophores contain a fluorescent impurity

The work presented in this chapter has been published in the following paper:

Stone, M. B. & Veatch, S. L. Far-Red Organic Fluorophores Contain a Fluorescent Impurity. ChemPhysChem 15, 2240–2246 (2014).

Far-red organic fluorophores commonly used in traditional and super-resolution localization microscopy are found to contain a fluorescent impurity with green excitation and near-red emission. This near-red fluorescent impurity can interfere with some multi-color STORM/PALM measurements in live cells and produce subtle artifacts in chemically fixed cells, and prevents precise quantification of multicolor super-resolution microscopy data without bleed correction of this bleed through. Here, I describe alternative dyes which do not contain fluorescent impurities in order to avoid artifacts in super-resolution localization microscopy, and also show methods to correct correlation functions when bleed through is present.

2.1: Introduction

The far-red dyes Cy5 and Alexa 647 are popular choices for diverse fluorescence applications because they have large extinction coefficients, high quantum yields, and excitation maxima at frequencies with low cellular absorption. These dyes and their structural analogs are a preferred choice for (direct) stochastic optical reconstruction microscopy ((d)STORM) because they exhibit highly favorable photoswitching characteristics[119,122,153,154], allowing densely labeled

proteins to be stochastically sampled and localized as single molecules. It is possible to conduct quantitative, two-color super-resolution microscopy experiments by imaging a far-red photoswitchable organic dye together with a spectrally distinct organic dye or fluorescent protein[155–160]. Two-color super-resolution microscopy experiments reveal the nanoscale locations of two independently-labeled sets of biomolecules, allowing quantitative analysis of co-clustering, oligomerization, and relative diffusion[161–164]. However, we observed that the dyes Cy5 and Alexa 647 exhibit fluorescence in the green emission channel when excited by either 532 or 561 nm lasers, which can interfere with sensitive multicolor experiments.

2.2: Results

2.2.1: A near-red fluorescence signal is detected in far-red dye stocks

Here we describe a fluorescent anomaly associated with Cy5, Alexa 647 and structurally related dyes that can interfere with quantitative two-color super-resolution microscopy measurements. This anomaly is demonstrated in **Figure 1a** where endogenous B cell receptor (BCR) is labeled with $f(Ab)_1$ fragment conjugated to either Alexa 647 or Cy5. Live CH27 cells are simultaneously illuminated with both 640 nm and 561 nm lasers under total internal reflection while far-red (660 nm–740 nm) and near-red (576 nm–630 nm) emissions are collected. Receptors diffusing in the image plane are detected in the far-red emission channel as expected. Surprisingly, a diffusing fluorescent signal is also observed in the near-red emission channel, even though this sample is only labeled with Alexa 647 or Cy5 dyes, both having emission spectra far removed from the near red emission channel. Fluorescent signals in the near-red emission channel can be observed by viewing raw data (Movie S1 in reference 165), reconstructed super-resolved images (**Figure 2a**), or by counting the rate of events that occur per unit area (**Figure 2b**).

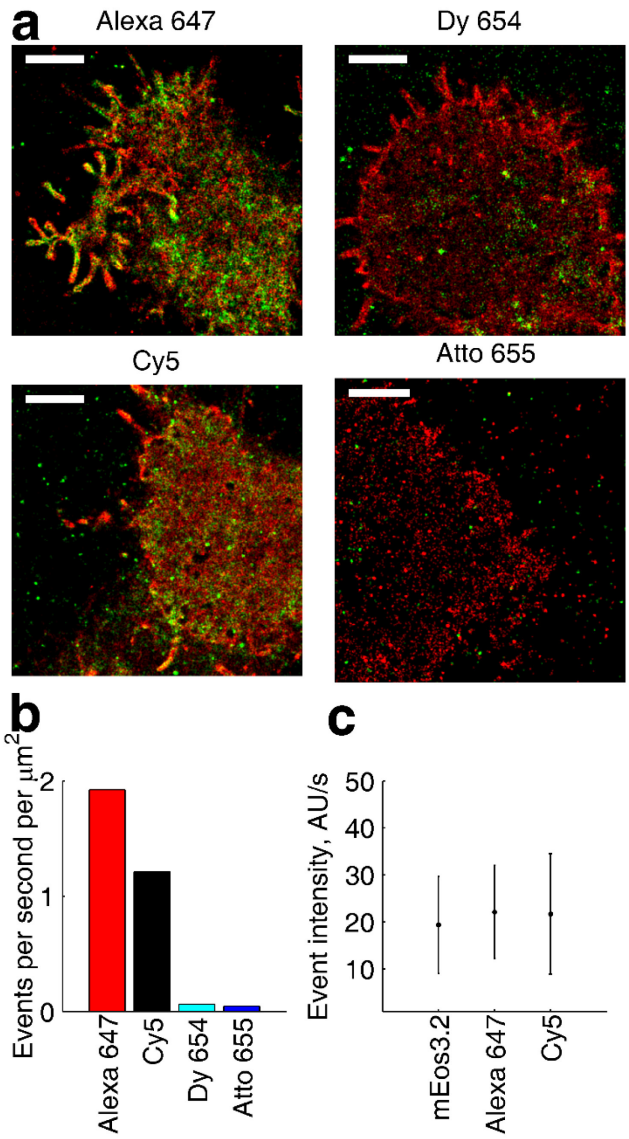

Figure 2: Near- and far-red emission is observed with simultaneous 640 nm and 561 nm excitation

(a) CH27 cells are labelled with $f(Ab)_1$ anti BCR conjugated to the indicated dye and observed through simultaneous illumination with 561 nm and 640 nm laser light. Emission was separated using a dichroic and bandpass filter set, and reconstructed images of near-red emission (576 nm–630 nm) are shown in green and far-red emission (660 nm—740 nm) shown in red. Scale bars are 3 µm. **(b)** The number of events per second per μm^2 in the near-red emission channel detected during the simultaneous excitation. **(c)** The average event intensity per second for mEos3.2, Alexa 647, and Cy5 excited by 561 nm laser light. Laser intensity and camera settings were kept constant between measurements. Error bars indicate one standard deviation.

Here, an event is defined as a local maximum with intensity greater than 5 times the standard deviation of the image noise and is also well fit by a defined Gaussian, as detailed in **Methods Section 2.4.4**. A similar population of near-red emitting fluorophores is observed when antibodies are conjugated to reactive fluorophores of different batch numbers, when antibodies are conjugated to fresh reactive dye stocks or stocks that have been stored in DMSO at -80^{o}C for >1 year, when antibodies or toxins are purchased pre-conjugated to fluorophores, or when supported membranes are labelled with DiD-C_{18}, a fluorescent lipid analog that is structurally similar to Cy5 (Movie S2 and S3 in reference 165). We performed 2 color super-resolution imaging with identical excitation and acquisition conditions to compare the density and intensity of near-red fluorescent events between four different far-red dyes. Endogenous BCR expression levels do not vary dramatically between cells therefore the density of fluorescent events can be compared, and the density of near-red events is reflective of the amount of fluorescent impurity labeling the $f(Ab)_1$ fragment and thus the BCR. The intensities of near-red fluorescent events from Alexa 647 and Cy5 are comparable to those of mEos3.2[124,166] when either fluorophore is excited by 561 nm light. However, the number of events observed in the near-red channel is dramatically reduced when the alternative STORM dyes Dyomics 654 and Atto 655 are used (**Figure 2**).

Near-red fluorescent events from Alexa 647 and Cy5 are also apparent when cells are illuminated with 532 nm light and near-red emission is collected between 545 and 620 nm. The intensity of near-red fluorescent events from Alexa 647 and Cy5 are comparable to those from Alexa 532 under the same illumination conditions. We find that the density of near-red events does not vary with time over the course of an experiment and do not depend on the presence of 640 nm excitation, suggesting that they are not induced by the laser excitation. Fluorescent events detected in both channels are diffusive under our imaging conditions and are not correlated in space. This observation suggests that the fluorescent anomaly is an impurity present in the reactive dye stock with blue-shifted spectral characteristics, and not simply bleed through of fluorescence between channels. We find that this fluorescent moiety does not photo-switch in the presence of the oxygen depleted and reducing imaging buffer, leading to long

single molecule trajectories. This photo-stability results in a large number of fluorescent events in the near-red emission channel when compared to the far-red emission channel. This occurs even when the relative concentration of the near-red fluorescent moiety is a small fraction of total dye since near-red fluorophores are visible at all times whereas the vast majority of far-red fluorophores are in a reversible dark state. Again, fewer fluorescent events are observed in the near-red emission channel when cells are labelled with antibodies conjugated to Dyomics 654 or Atto 655 and excited with 532 nm light (**Figure 3a-c**).

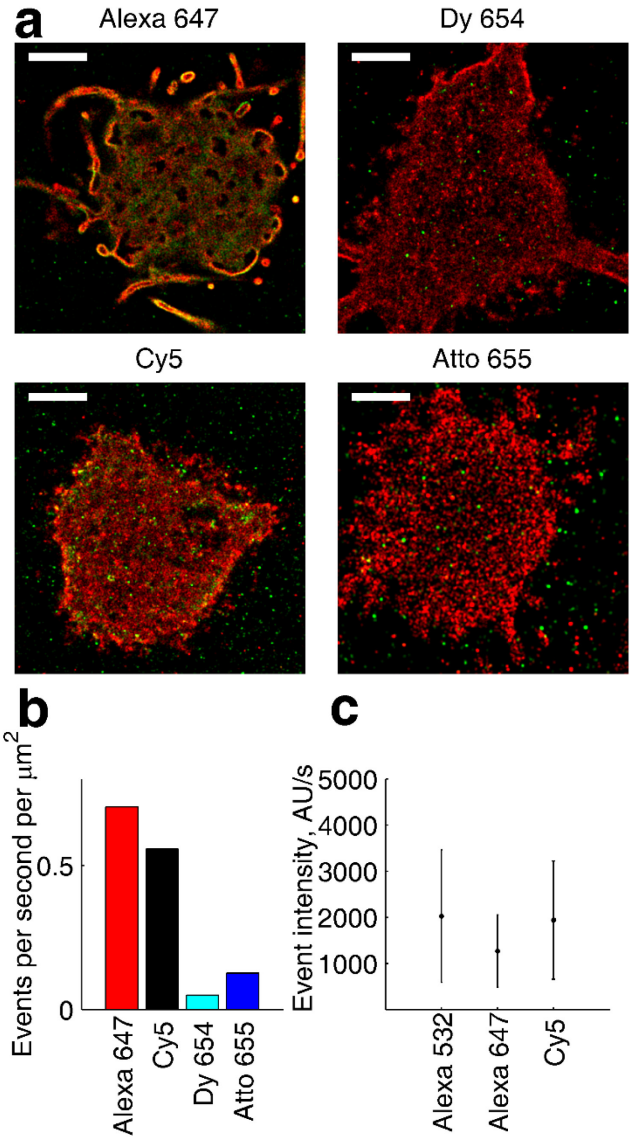

Figure 3: Near- and far-red emission is observed with simultaneous 640nm and 532 nm excitation

(a) CH27 cells are labeled with $f(Ab)_1$ anti BCR that was conjugated to the indicated dye and observed through simultaneous illumination with 532 nm and 640 nm laser light. Emission was separated using a dichroic and bandpass filter set, and reconstructed images of near-red emission (545 nm—620 nm) are shown in green and far-red emission (660 nm—740 nm) shown in red. Scale bars are 3 μm. **(b)** The number of events per second per μm^2 detected during the simultaneous excitation as bar plots. **(c)** The average event intensity per second for Alexa 532, Alexa 647, and Cy5 excited by 532 laser light. Laser intensity and camera settings were kept constant between measurements. Error bars indicate one standard deviation.

2.2.2: Alternative STORM dyes are free of near-red impurities

The number of events observed in the near-red channel is dramatically reduced when the alternative STORM dyes Dyomics 654 and Atto 655 are used (**Figure 2** and Movie S4 in reference 165). The intensities of near-red fluorescent events from Alexa 647 and Cy5 are comparable to those of mEos3.2[124,166] when either fluorophore is excited by 561 nm light. Near-red fluorescent events from Alexa 647 and Cy5 are also apparent when cells are illuminated with 532 nm light and near-red emission is collected between 545 and 620 nm. Again, fewer fluorescent events are observed in the near-red emission channel when cells are labelled with antibodies conjugated to Dyomics 654 or Atto 655 and excited with 532 nm light (**Figure 3a-c**). The intensity of near-red fluorescent events from Alexa 647 and Cy5 are comparable to those from Alexa 532 under the same illumination conditions. We find that the density of near-red events does not vary with time over the course of an experiment and do not depend on the presence of 640 nm excitation, suggesting that they are not induced by the laser excitation. Fluorescent events detected in both channels are diffusive under our imaging conditions (Movie S1, S2, and S3 in reference 165) and are not correlated in space. This observation supports that the fluorescent anomaly is an impurity present in the reactive dye stock with blue-shifted spectral characteristics and not simply bleed through of fluorescence between channels. We find that this fluorescent moiety does not photo-switch in the presence of the oxygen depleted and reducing imaging buffer, leading to long single molecule trajectories. This photo-stability results in a large number of fluorescent events in the near-red emission channel when compared to the far-red emission channel. This occurs even when the relative concentration of the near-red fluorescent moiety is a small fraction of total dye since near-red fluorophores are visible at all times whereas the vast majority of far-red fluorophores are in a reversible dark state.

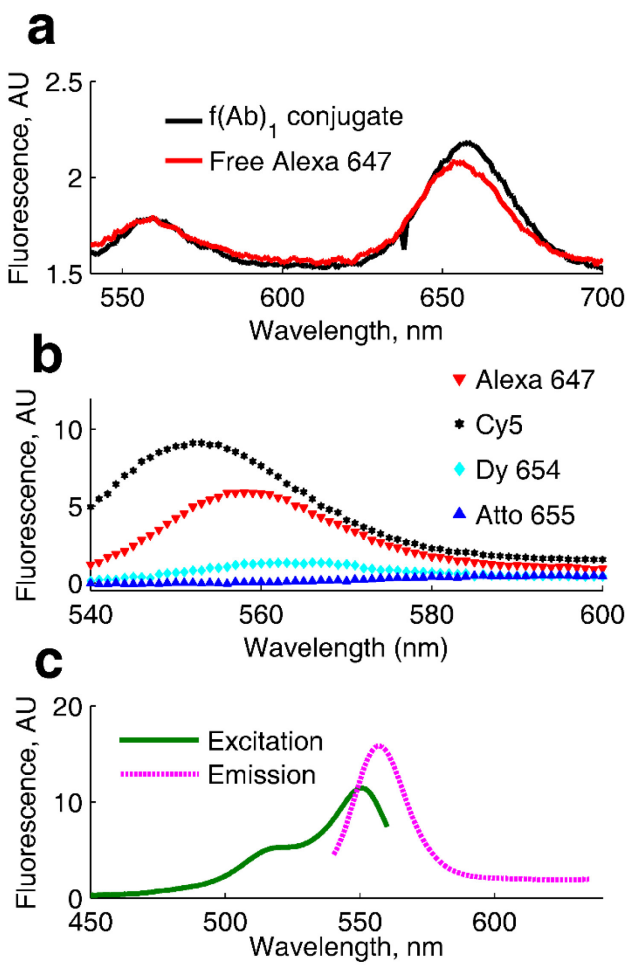

Figure 4: Near-red emission is observed in bulk fluorescence measurements

(a) The fluorescence emission spectrum of Alexa 647 either as the unconjugated NHS ester (800nM) or conjugated to $f(Ab)_1$ fragments (50 µg/ml). Samples are excited by 530 nm light with identical gain and bandwidth. The magnitude of near-red emission and the overall shape of the spectra are comparable between the two samples. **(b)** Fluorescence emission spectra of the four dyes with excitation at 530 nm. All dyes are diluted to 1 µM in PBS and the near-red portion of the spectrum is shown. **(c)** Fluorescence excitation and emission spectra of the near-red moiety in Alexa 647 NHS ester. The excitation spectrum is acquired by monitoring emission at 575±2 nm over a range of excitation wavelengths. The emission spectrum is acquired by exciting at 530 nm. The gain is held constant within but not between each subfigure.

2.2.3: Near-red fluorescence is detected in bulk fluorescence assays

Near-red fluorescence is also observed in bulk fluorescence assays of Alexa 647 conjugated to antibodies, and in unconjugated Alexa 647 diluted in PBS (**Figure 4a**). The 560 nm peak in these emission spectra of Alexa 647 arises from the near-red fluorescent species, while the

second peak at 660 nm corresponds to the expected far-red emission maxima of Alexa 647. These spectra confirm that the near-red fluorescent species is present in the reactive dye stock prior to c onjugation and is not a consequence of antibody conjugation. This also confirms that the near-red fluorescent species can conjugate to antibodies. The expected Alexa 647 emission peak is of roughly equal magnitude to the near-red emission because these probes are excited far from their excitation maxima, and not because these species are of roughly equal concentration in solution (see below). Unconjugated Cy5 also shows an emission maximum near 560 nm with a similar magnitude to Alexa647 when diluted to the same concentration (1μM; **Figure 4b**). In contrast, the emission intensity in this spectral region is greatly reduced for the case of Dyomics 654 and Atto 655, in good agreement with the single molecule observations shown in **Figure 2 and Figure 3**.

The excitation spectrum of unconjugated Alexa 647 in PBS was measured using emission collection at 575 nm in order to view the excitation spectra of the anomalous fluorescent peak. The shape of the excitation spectrum is similar to other fluorophores with an excitation peak near 550 nm and a shoulder from 520-530nm (**Figure 4c**). The near-red emitting species has excitation and emission maxima near 550 nm and 560 nm respectively, which is similar to the Cy3 fluorophore but with a smaller Stokes shift. These bulk fluorescence measurements are consistent with our observations of single molecule intensities. We find that near-red single molecule event intensities are roughly 2 orders of magnitude greater when excited using a Cy3 filter-set (Ex: 532 nm / Em: 545 nm—620 nm) than when excited with a RFP filter set (Ex 561 nm / Em 576 nm–630 nm). This occurs because the emission window for the Cy3 filter set are more centered on prominent regions of the fluorescent impurity's emission spectra. Unfortunately, the single molecule intensities of these anomalous near-red events are comparable to those of the common super-resolution probes using both filter-sets (**Figure 2c and Figure 3c**). When excited with 532nm light, the anomalous near-red single molecule intensities are indistinguishable from Alexa 532 acquired under the same imaging conditions, and when excited at 561nm, the anomalous near-red fluorescence intensity closely resembles that of the commonly used PALM probe mEos3.2. These similar intensities prevent separating the impurity from either Alexa 532 or mEos3.2 events post processing.

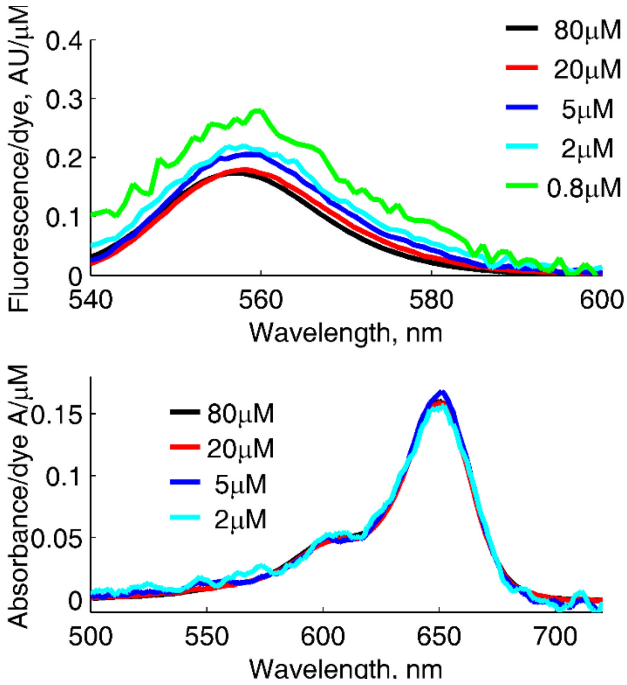

Figure 5: Fluorescence and absorbance spectra are not concentration dependent

(a) Fluorescence emission spectra at 530 nm excitation of unconjugated Alexa 647 NHS ester diluted into PBS at various concentrations. Fluorescence intensity is normalized by the concentration of the dye. **(b)** Absorbance spectra of unconjugated Alexa 647 NHS ester diluted into PBS at various concentrations. Absorbance is normalized by the concentration of the dye.

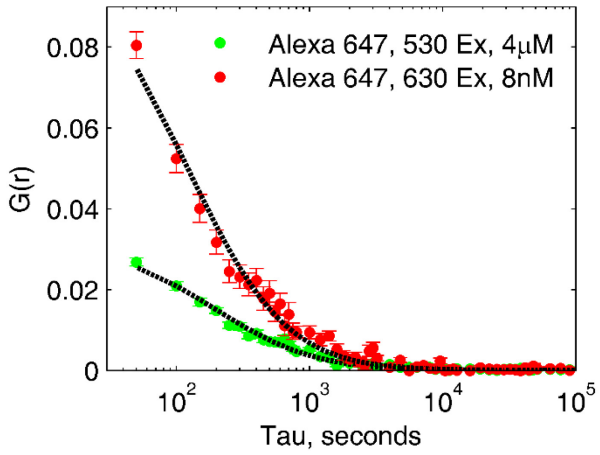

Figure 6: FCS correlation curves for unconjugated Alexa 647

Time correlation curves for Alexa 647 far-red and near-red emission were determined by diluting Alexa 647 to 8 nM and exciting with 630 nm light, or by diluting Alexa 647 to 4 μM and exciting with 530 nm light. Dotted black lines are fits to Equation 1, and are used to extract fit parameters for Table 2.

Table 2: Concentrations of fluorescent impurity in Alexa 647 determined by FCS

Excitation	$C_{dilution}$	C_{FCS}	$C_{dilution}/C_{FCS}$
630 nm	8 nM	6 nM	1.1
530 nm	4 μM	12 nM	308

Previous work has demonstrated that cyanine dyes can dimerize and aggregate in aqueous solution, changing their absorption and emission spectra[167]. To determine if the observed near-red fluorescence is a result of dye aggregation, the fluorescence and absorbance of unconjugated Alexa 647 NHS ester was examined over a range of dye concentrations. The molar intensity of the near-red emission is weakly quenched at higher dye concentrations (**Figure 5a**), indicating that the anomalous fluorescence is not a result of aggregation. If this were the case, higher concentrations should increase the fraction of dimers or higher order aggregates. Additionally, we do not detect the emergence of strong H-band absorbance[168,169] at concentrations relevant for dye conjugation to labeling antibodies (**Figure 5b**), again suggesting that dyes are not aggregating in large quantities.

Finally, we characterize the diffusion and number of near-red and far-red fluorophores of Alexa 647 NHS ester in aqueous dilutions using fluorescence correlation spectroscopy (**Figure 6**). From the acquired FCS spectra we extract both the concentration and diffusion coefficient of both species, as described in **Methods Section 2.4.4**. We find that there is approximately one green fluorescent moiety for every 300 far-red Alexa 647 fluorophores, indicating that the fluorescent impurity is present at 0.3%, well within the quoted purity of the commercially acquired compound. We additionally observe similar rates of diffusion for the two fluorescence species, 240 $\mu m^2/s$ for the near-red emission and 270 $\mu m^2/s$ for the far-red emission. This again

supports the conclusion that the near red impurity is not an aggregate, since Alexa 647 and the green fluorescent moiety have roughly the same hydrodynamic radius.

2.3: Discussion

These studies indicate that Alexa 647 and Cy5 are potential sources of significant cross-talk when used together with organic Alexa 532 or Cy3 fluorophores with 532 nm excitation, or when used in conjunction with less intense protein based fluorophores excited with 561 nm light. We do not expect that the near-red fluorescence would be problematic in traditional single molecule measurements, since the relative concentration of near-red to far-red fluorophore is low. However, this near-red fluorescence could lead to substantial artifacts in multi-color super-resolution experiments since Cy5 or Alexa 647 fluorophores are densely labeled, with most dyes residing in a reversible dark state for the majority of the measurement. Since the near-red moiety does not photo-switch, a significant number of fluorophores can be visualized at any given time. This is expected to only lead to minor artifacts in chemically fixed cells, since fluorescence signals that do not vary with time are typically removed in image processing. Aberrant signals could still subtly contaminate images if there is significant stage drift or if the excitation intensity is not stable with time. The presence of the near-red fluorescence more significantly complicates measurements when probes are mobile, as is the case when imaging membrane proteins within live cells. Under these conditions, background subtraction does not remove long lived near-red fluorescence as these probes can explore large areas over a given measurement.

Multi-color super-resolution imaging in live cells has been accomplished previously by a large number of different groups[170–180], and in most cases this impurity could not have impacted stated results. Our findings have no bearing on studies that exclusively used fluorescent proteins[161,164,170–173], or proteins in combination with quantum dots[174], since these probes are not investigated here. As far as we are aware, existing studies using mEos2 or mEos3.2 proteins in live cells combination with organic fluorophores have not utilized Cy5 or Alexa 647, and instead have used Atto 655[175,176], which we observe to be free of this fluorescent impurity. Past studies have also used other organic probe pairs in live cells, such as cationic rosamine and BODIPY dyes[177] or Alexa 488 in combination with Alexa 555[178]. Again, we do not expect that these probe pairs

would lead to anomalous results based on our measurements. Several past studies have used Alexa 647 or Cy5 in combination with near-red dyes in live cells. In one, Alexa 647 was used in conjunction with Alexa 568 which is excited at 561nm[179]. We do not anticipate that this near-red fluorescence would lead to anomalies in this measurement since single molecule event intensities of Alexa 568 should be orders of magnitude larger than the impurity and would be removed in image processing. At least one past study has used Cy3 and Cy5 in combination for live cell super-resolution imaging[180]. It is possible that aspects of their results could be impacted by our observations, although we have not investigated the tetrazene or azide modified dyes used in this work.

In our own past work, we have imaged mEos3.2 in combination with Alexa 647 in chemically fixed cells[126], and the small number of anomalous near-red fluorophores present in these samples did not impact our results. We only anticipate that results in fixed cells to be adversely affected when imaging Alexa 647 or Cy5 labelled species present at high local density in combination with a near-red labelled species present at low local density, especially when probes are anti-correlated[181]. In this case, an impurity present even at low mol % could adversely impact experimental results for fixed cells.

For multi-color live cell measurements using Alexa532, mEos3.2, or mEos2, we recommend imaging these near-red probes in combination with a far-red probe such as Atto 655 or Dyomics 654 in order to minimize possible artifacts. In principal, it should be possible to use chromatography techniques to separate the far-red Alexa 647 or Cy5 from the near-red dye prior to conjugation to protein. This purification is technically challenging due to the low concentration of the near-red species, the hydrolysis of reactive groups on the dye, and the similarity in size between the two species. Dy654 and Atto 655 photophysical properties are suitable for (d)STORM, however the duty cycle of Dy654 and the photon yield of Atto 655 are less desirable than those of Alexa 647 and Cy5[154]. Overall, these experiments reinforce the need for careful controls in quantitative multi-color imaging measurements.

2.4: Methods

2.4.1: Fluorescence labeling

$f(Ab)_1$ fragment goat antibody to mouse IgM, μ chain specific (Jackson Immuno Research) was chemically modified with either Alexa Fluor 532 carboxylic acid succinimidyl ester, Alexa Fluor 647 carboxylic acid succinimidyl ester (Life Technologies), Atto 655 NHS ester (Sigma), Dyomics-654-NHS-ester (Dyomics GmbH). Modifications were carried out in aqueous solution buffered by 0.01 M NaH_2PO_4 with 0.01 M NaH_2CO_3, pH 8.2 for one hour at room temperature. Reaction was quenched with addition of 10 mM 2-mercaptoethanol (Sigma) prior to gel filtration on illustra NAP-5 columns (GE Healthcare) to remove unbound dye from labeled protein. Typically each $f(Ab)_1$ is labeled with 4 dye molecules. Cy5 modified goat antibody to mouse IgM, μ chain specific was purchased already conjugated to Cy5 (Jackson Immuno Research). Cholera toxin B subunit (Life Technologies) was purchased conjugated to Alexa Fluor 647. Glass supported multilayers containing DiD-C_{18}, (Dioctadecyl Tetramethylindodicarbocyanine) (Invitrogen) and diphytanoylphosphocholine (Avanti Polar Lipids) were prepared by spin-coating lipids from chloroform, drying under vacuum, and hydrating with purified water.

2.4.2: Cells

CH27 cells were maintained in low glucose DMEM (Gibco) containing 15% FBS (Mediatech), 10 mM HEPES, 110 mg/L sodium pyruvate, 50 μM BME, and 1% Pen/Strep in 5% CO_2 at 37°C. Cells were plated at 100,000 / ml and grown overnight on glass bottom wells (MatTek Corporation) before staining with 5 μg/ml labeled $f(Ab)_1$ for ten minutes and extensive washing with PBS prior to imaging. mEos3.2[124] tagged Lyn protein was created using standard cloning techniques from Lyn-eYFP[108] (a gift from Barbara Baird) and mEos3.2 was generated from mEos2[166] and was a kind gift from Akira Ono. 10^6 CH27 cells were transfected with 1 μg mEos3.2 tagged Lyn plasmid DNA (a gift from Akira Ono) in Clontech N1 vector (Clontech) using Lonza Nucleofector electroporation (Lonza) for expression of mEos3.2 in **Figure 2**c.

2.4.3: TIRF microscopy

Imaging was performed on an Olympus IX81-XDC inverted microscope with a cellTIRF module, a 100X UAPO TIRF objective (NA=1.49), active Z-drift correction (ZDC) (Olympus America). Images were acquired at 20 frames per second on an iXon-897 EMCCD camera (Andor). Excitation of Alexa-647 was accomplished using a 640 nm diode laser (CUBE 640-75FP, Coherent) and 561 nm laser excitation. Laser energy density at sample is estimated to be 3kW/cm^2 (561 nm), 14 kW/cm^2 (640 nm), and 20 kW/cm^2 (530 nm). Excitation and emission was filtered using the quadband dichroic mirror LF405/488/561/635-4X-A-000 for 561 nm excitation, or LF405/488/561/635-4X-A-000 for 532 nm excitation (Semrock). Emission was split into two channels using a DV2 emission splitting system (Photometrics) with a T640lpxr dichroic mirror to separate emission, ET605/52m to filter near-red emission, and ET700/75m to filter far-red emission (Chroma). Samples were imaged in a buffer containing: 30 mM Tris, 100 mM NaCl, 5 mM KCl, 1 mM $MgCl_2$, 1.8 mM $CaCl_2$, 50 mM glucose, 12 mM glutathione, 40 μg/ml catylase, and 500 μg/ml glucose oxidase.

2.4.4: Single molecule analysis

Single molecule fluorescent events were determined first finding local maxima with intensity greater than 5 sigma above standard deviation of background subtracted and gaussian filtered images, then fitting background subtracted images to 2D Gaussian functions using nonlinear least squares. The ensemble of events was then culled to remove outliers in brightness, size, and localization error[162]. All data from event intensity analysis were taken with equivalent gain and excitation brightness, and were normalized by acquisition time to give intensity per second. Event intensity is determined by integrating the background subtracted intensity around the center of single molecule localizations with a radius of 560 nm, and intensity per unity time is determined by dividing this intensity by the camera integration time. Microscopy was controlled such that all acquisitions performed at a particular excitation wavelength used the same laser intensity, camera integration time, and gain settings. Super-resolved images were reconstructed by incrementing the intensity of pixels at positions corresponding to localized single molecules after correcting for stage drift and chromatic abberation[156]. All analyses were carried out in MATLAB (The MathWorks).

2.4.5: Fluorescence and absorbance spectroscopy

Fluorescence excitation and emission spectra were collected using a FP-6500 spectrofluorometer (Jasco) with a 150W xenon lamp as excitation source and a 3 nm bandpass filter for excitation and emission. All fluorescence samples were measured in 4 mm pathlength quartz cuvettes (Starna). Fluorescence spectra from Alexa Fluor 647 carboxylic acid succinimidyl ester (Invitrogen), Cy5 Maleimide (GE Healthcare), Dyomics-654-NHS-ester (Dyomics), and Atto 655 NHS ester (Sigma) were acquired in **Figure 4b**. Absorbance spectra were collected with a NanoDrop 2000 Spectrophotometer (Thermo).

2.4.6: Fluorescence correlation spectroscopy

Fluorescence correlation spectroscopy was performed on an Olympus IX-81 microscope equipped with an ALBA dual-channel spectrophotometer (ISS) and U Plan S-APO 60X 1.2 NA water immersion objective (Olympus America). Samples were excited with a WhiteLase Supercontinuum Source SC400-6-PP (Fianium), and excitation wavelengths were selected using an AOTF (Fianium). Excitation and emission were filtered using the quadband dichroic mirror 405/488/532/635 (Alluxa). Fluorescence signals passing through a 50 μm diameter pinhole were detected with an avalanche photo-diode SPCM-AQRH-15 (Perkin Elmer) and time correlated single photon counting was accomplished using a SPCM-830 TCSPC module with a maximum 8MHz detector count rate (Becker-Hickl GmbH). Instrumentation was controlled and data was analyzed using VistaVision software (ISS). Time-averaged correlation functions from dye diffusion through excitation volume were fit to the model for 3-dimensional motion, where N is the mean number of fluorescent molecules in the excitation volume, t is the time lag of the fluorescence correlation, t_D is the characteristic dwell time for a particular molecule and excitation volume, and k is a factor to account for the shape of the excitation volume.

$$G(t) = \frac{1}{\left(N\left(1+\frac{t}{t_D}\right)\right)} \frac{1}{\sqrt{1+\left(\frac{t}{kt_D}\right)}} \qquad \textit{Equation 1}$$

The parameters N and t_D of Equation 1 were fit to G(t), the experimentally determined time correlation function. The diffusion coefficient, D, was calculated using the following equation, where w_{xy} is the beam waist of the focal volume in the xy plane:

$$D = \frac{w_{xy}^2}{4t_D} \qquad \textit{Equation 2}$$

w_{xy} was calibrated using the far-red emission of Cy5 and the near-red emission of Cy3 dye using published diffusion coefficients 250 um^2/s for Cy5[182] and 280 um^2/s for Cy3[183]. The three dimensional excitation volume (V_{EX}) was calibrated using known concentrations, C_{dye}, of the control dyes Cy3 and Cy5 in conjunction with the fit parameter N.

$$V_{EX} = N/C_{dye} \qquad \textit{Equation 3}$$

V_{EX} for 630 nm excitation was 2.33 μm^3, whereas V_{EX} for 530 nm excitation was 3.87 μm^3.

Alexa 647 FCS curves were fit to Equation 1 to obtain N and converted to a concentration using the calibrated excitation volume for each channel. Different dilutions of Alexa 647 ($C_{dilution}$) were used to determine the concentration of the near-red and far-red species (C_{FCS}), as indicated in Table 2. C_{FCS} and $C_{dilution}$ are measured independently but are in good agreement for the far-red excitation of Alexa 647.

Chapter 3: Steady-state cross-correlations for live two-color super-resolution localization data

The work presented in this chapter has been published in the following paper:

Stone, M. B. & Veatch, S. L. Steady-state cross-correlations for live two-colour super-resolution localization data sets. *Nat Commun* **6,** (2015).

Cross-correlation of super-resolution images gathered from point localizations allows for robust quantification of protein co-distributions in chemically fixed cells. Here, this is extended to dynamic systems and live cells through an analysis that quantifies the steady-state cross-correlation between spectrally distinguishable probes. This methodology is used to quantify the co-distribution of several mobile membrane proteins in both vesicles and live cells, including Lyn kinase and the B cell receptor during antigen stimulation.

3.1: Introduction

Super-resolution localization microscopy techniques such as (direct) stochastic reconstruction microscopy, (d)STORM[118,119] and (fluorescence) photoactivation localization microscopy, (f)PALM[120,121] can be used to quantitatively investigate the nanoscale co-clustering of labeled biomolecules in multi-color fluorescence experiments. In images reconstructed from immobilized probes, the spatial co-distributions of spectrally distinct labeled proteins can be quantified using bivariate Ripley's functions[184] or by cross-correlation[138,139,185]. In live cells, however, single molecules can travel over large distances during the time it takes to reconstruct a

single well sampled image, complicating the interpretation of co-localization results. It is possible to quantify the co-distributions of some proteins in live cells when their dynamics are slow compared to the time it takes to reconstruct a super-resolved image[172,179]. However, many proteins undergo fast diffusion making this approximation invalid within the constraints of most image acquisition systems, even considering recent advances[186] in fast image acquisition and multi-emitter fitting.

A robust set of analytical tools has been developed to quantify the time-dependent co-localization of components in diffraction limited images based on image cross-correlation[187,188], although these techniques do not take advantage of the resolution improvement afforded by localization-based super-resolution microscopy. Past work has extended cross-correlation analysis to localized single molecules through a technique named particle image cross-correlation spectroscopy (PICCS)[161]. While powerful, this method was designed to detect co-localization between components over short distances and reports only a single correlation coefficient whose magnitude can vary if the density of observed components changes with time. Here, we present an alternate approach that is quantitative, model-independent, and robust to the variations in signal density inherent in super-resolution localization measurements. The steady-state cross-correlation analysis presented here is equivalent to approaches commonly used in statistical mechanics and condensed matter physics which provide an estimate the magnitude of interactions between components in units of energy, and the statistical significance of the correlation function can be estimated directly from acquired data.

Here, we demonstrate the robustness of the steady-state cross-correlation approach to quantifying point localized datasets in mobile systems ranging from simulated data, an isolated plasma membrane vesicle, and live B cell lymphocytes. Using instantaneous cross-correlation on live two-color super-resolution microscopy data, we observe that Lyn kinase is recruited to B cell receptors (BCR) soon after clustering with a multivalent soluble antigen, and this recruitment is reduced but not ablated in the presence of the Src kinase inhibitor PP2. The degree of co-localization between Lyn and clustered BCR in the absence of the inhibitor corresponds to an effective interaction potential of roughly $1 k_B T$ over the extent of the BCR cluster (~100 nm), where $k_B T$ is the thermal energy, and co-localization decreases with increased stimulation time

when short (20s) steady-state time-intervals are used. By combining the steady-state cross-correlation methodology with a mobility analysis of Lyn, we find that co-localized Lyn proteins diffuse more slowly, consistent with direct binding between Lyn and immobilized components within BCR clusters. We quantify the off-rate of this interaction as well of the fraction of Lyn proteins in the immobilized state as a function of stimulation time. Overall, we conclude that this cross-correlation approach is a powerful tool to probe interactions between labeled proteins in live cell super-resolution microscopy data-sets.

3.2: Results

3.2.1: Cross-correlations quantify mobile and immobile systems

The cross-correlation function, $C(r, \tau)$, measures the probability of finding a pair of differently colored fluorophores as a function of their separation distance r at a time lag τ. In super-resolved datasets of immobile systems, one can quantify co-localization using $C(r, \langle\tau\rangle)$, where $\langle\tau\rangle$ indicates an average over all τ, meaning that all localizations contribute independently of when they were observed[138,139,185]. $C(r,\langle\tau\rangle)$ is evaluated equivalently by tabulating distances between all localized fluorophores of different colors irrespective of time or by reconstructing images of each fluorophore type followed by image cross-correlation using Fourier transform methods (**Figure 7 and Methods Section 2.4.4)**. Generally, the variance in C(r) determines statistical significance, depends on the number of localized molecules in each color channel as well as the magnitude of correlations, and can be determined directly from acquired data as described in **Methods Section 3.4.2** and validated in **Figure 8 and Figure 9**.

The cross-correlation can provide an accurate estimate on the number of correlated molecules if the average density of molecules is known. Importantly, finite localization precision as well as any errors in registering the two image channels act to systematically broaden short-range correlations over longer distances while maintaining the integrated area under C(r)-1[189]. C(r) can be converted to the density of molecules of one type as a function of separation distance from the average labeled molecule of the other type, $\rho(r)$, by simply multiplying C(r) by the average density of that molecule $\langle\rho(r)\rangle$. Several methods have been described to estimate $\langle\rho(r)\rangle$ from super-resolution images[138,190–193] or average densities can be obtained using non-

imaging methods. Integrating ρ(r) allows for quantification of the average number of interacting proteins[139,189]. **Figure 10** demonstrates how to convert between C(r) and ρ(r) when <ρ(r)> is known for several examples described below.

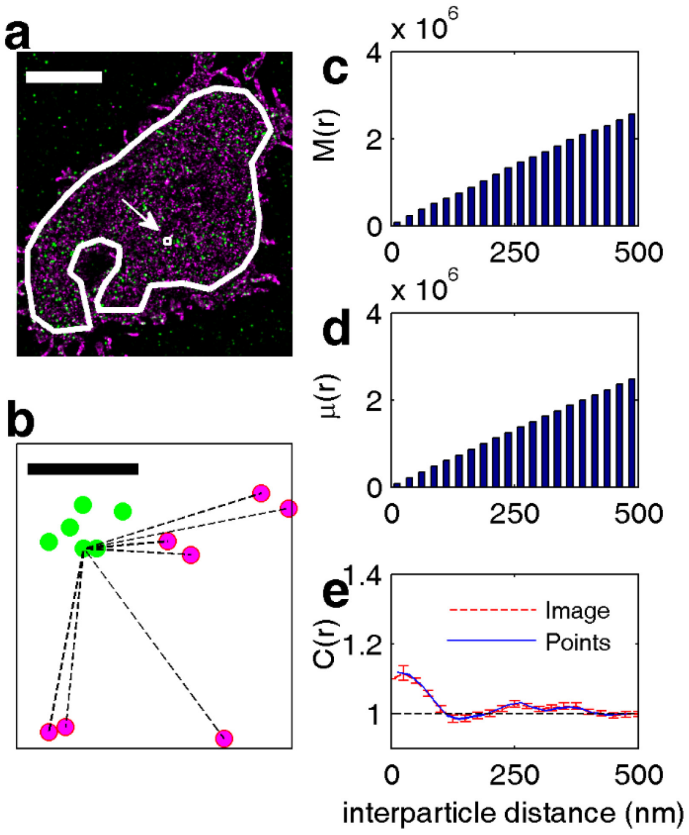

Figure 7: Construction of point by point cross correlation and equivalence to FFT method

(a) A reconstructed image of a chemically fixed B cell showing Lyn-mEos3.2 localizations in green and BCR Dyomics 654 localizations in magenta. Point-by-point and image cross correlations were evaluated within the region of interest (ROI) outlined in white pointed to by white arrow. Scale bar is 5 μm. **(b)** Point-by-point cross-correlations are tabulated by first measuring the distance between all possible pairs of red and green localizations. The sub-region denoted by small white box in (a) is used as an example and the distances between a single green particle and all magenta particles in this sub-region are shown as dotted lines for demonstration purposes. Scale bar is 100 nm. **(c)** The histogram M(r) constructed by binning all observed interparticle distances with a uniform bin width of Δr=25nm. **(d)** The normalization factor μ(r) is the expectation value for the number of interparticle distances observed for each bin in M(r) given a random distribution. **(e)** The point-by-point cross-correlation function C(r) is determined by dividing the observed interparticle distance histogram M(r) by the normalization factor μ(r). Thus, C(r) indicates that the observed interparticle distances is a random distribution when C(r) is equal to 1. Tabulating the cross-correlation using fast Fourier transforms (FFTs) on reconstructed images, shown in red, agrees with the point-by-point method, shown in blue from the same acquired data.

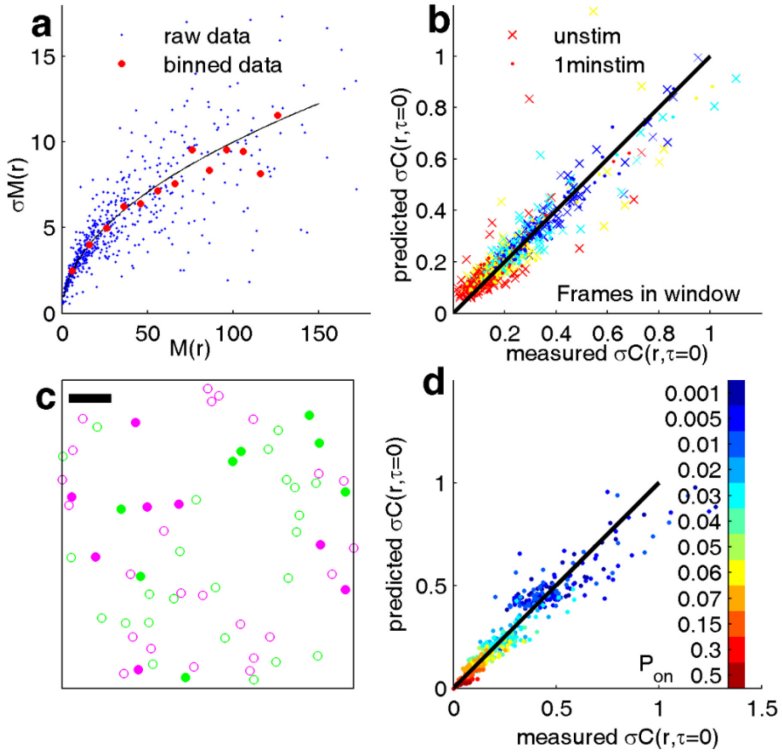

Figure 8: Verification of statistical errors in determining C(r)

(a) The standard deviation of M(r), σM(r), as a function of the average value of M(r), <M(r)>, was determined from point localization data from 7 distinct chemically fixed cells labeled with BCR and Lyn, where single molecules were imaged over an average of 9000 frames per cell. This dataset included both antigen stimulated and unstimulated cells fixed prior to imaging. In order to probe a broad range of <M(r)> values, M(r) was tabulated with Δr=100 nm spatial bins using time windows that were shorter than the total number of frames acquired during an experiment. Time windows of equal size; 250, 500, 1000, or 2000 frames were compared on a cell-by cell basis, and σM(r) vs. <M(r)> is plotted for all time windows and radii bins in all cells as blue dots. Larger red circles show average values of M(r) over a range of <M(r)> values (<M(r)> ±5). The black line is the square root of M(r), illustrating that σM(r) varies as $\langle M(r)\rangle^{0.5}$. **(b)** C(r) was determined from small time windows for the fixed cell data described in (a). The σC(r) between time windows of equal size for individual cells was measured and the error predictor σC(r) was calculated from Equation 6 using average values of <μ(r)> and <M(r)> between time windows as in (a). The black line is of slope 1 through the origin, showing agreement between the predicted error and the measured error obtained from repeated measurements. **(c)** A representative frame from a down-sampled Lennard-Jones (L-J) molecular dynamics (MD) simulation in which only 25% of positions are 'on', illustrated as filled circles, and all other particles are 'off', illustrated as empty circles. Only particles that are 'on' contribute to determining C(r, τ=0). Scale bar is 5σ. **(d)** MD simulation frames were down-sampled at various rates with probability of a particle being on as P_{on}, and sampling for each P_{on} was repeated 15 times with new balls being designated as magenta or green in each repeat. Particles blinked 'on' for 3 frames at a time and blinking was randomized between repeats. C(r, τ=0) was determined from particles on in the same frame using a bin size of Δr=0.061σ, and the standard deviation of all spatial bins of C(r, τ=0) between repeats were determined for all P_{on}. The error predictor σC(r) was calculated using Equation 7. Colors indicate various P_{on} and the black line is of slope 1 through the origin, showing agreement between the predicted error and the measured and error obtained from repeated measurements.

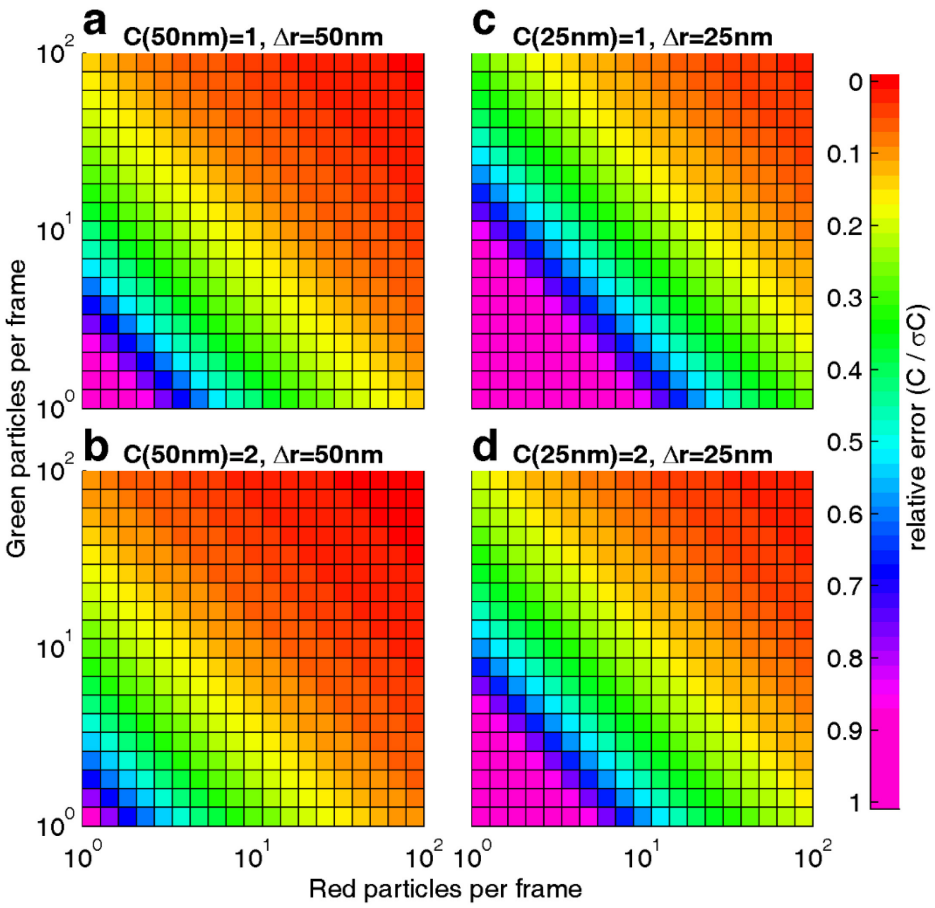

Figure 9: Statistical errors in C(r) are a function of the number of objects detected as well as the spatial bin size, Δr, and the observed correlation function

The surface plots show how $\sigma C(r, \tau))/C(r, \tau)$ given by Equation 7 varies with the number of localized particles per frame collected over 5000 frames, obtained by using $M(r, \tau)=C(r, \tau)\mu(r)$ and set values for $C(r, \tau)$ into the expression for $\sigma C(r, \tau)/C(r, \tau)$ given in Equation 7. We use a 10μm diameter circular mask and either 25nm or 50nm bin size to calculate W(r) and ΔA(r), and here we show only the first point of C(r). Relative error is given by the colorbar at right and relative error > 1 is not distinguished here. **(a,b)** Surface plot of predicted $\sigma C(r<50nm)/C(r<50nm)$ assuming either a random distribution ($C(r<50nm) = 1$) or a weakly co-clustered distribution ($C(r<50nm) = 2$). **(c,d)** Surface plot of predicted $\sigma C(r<25nm)/C(r<25nm)$ assuming either a random distribution ($C(r<25nm) = 1$) or a weakly co-clustered distribution ($C(r<25nm) = 2$). Note that increased spatial resolution requires greater sampling to obtain the same level of statistical significance. Also, optimal sampling is obtained when the same number of localizations are detected in each color channel, but poor sampling in one channel can be compensated for by greater sampling in the second channel.

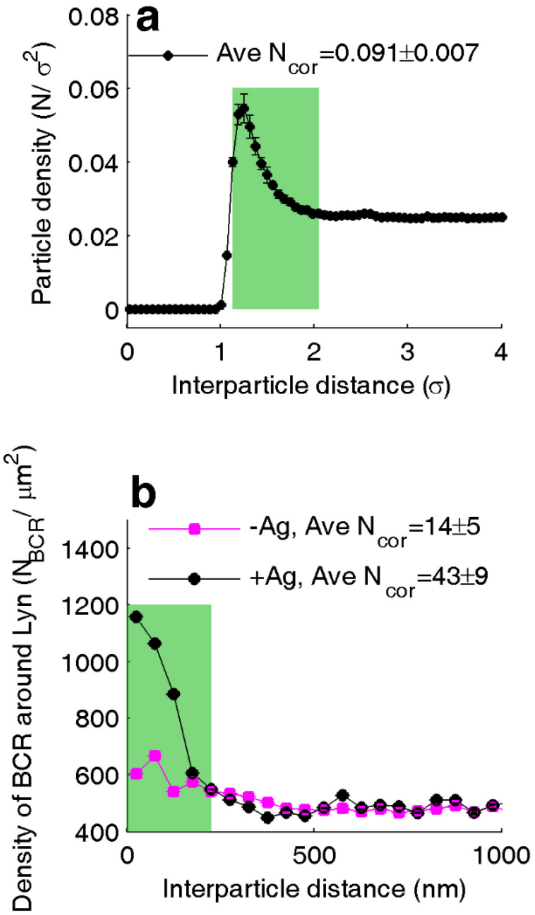

Figure 10: Particle density as a function of interparticle separation

If the average particle density (<ρ >) is known, then C(r) can be converted to the density of that type of particle as a function of separation distance from other particle type through ρ(r)=<ρ>C(r). **(a)** For the L-J MD simulation, <ρ> for both red and green particles is 0.025 particles / σ^2. Multiplying C(r) by this density gives ρ(r) between red and green particles. The particles are correlated between 1.1σ and 2σ where the attractive component of the L-J potential dominates, and the average number of correlated particles, N_{cor}, can be determined by measuring the area under the curve: $N_{cor} = \rho \sum (C(r) - 1) 2\pi r \Delta r$ over the range of 1.1σ to 2σ. In this case, N_{cor} is less than 1 since the particle density in the simulation is low and the interaction is weak. **(b)** For the case of Lyn and BCR in a live cell, the average density of BCR can be estimated from previous work[194,195] to be 500 BCR / μm^2. Multiplying the observed C(r) from a single live cell (also shown in **Figure 12a,b**) by this BCR density yields the density of BCR proteins as a function of separation distance from the average Lyn protein. These proteins are correlated with each other between 0 and 225 nm. $N_{cor}=\rho \sum (C(r) - 1) 2\pi r \Delta r$ is evaluated over this area gives the values shown in the figure legend.

In mobile systems, cross-correlations of reconstructed images, $C(r, \langle\tau\rangle)$, may not reflect a meaningful co-distribution since localizations that occur at different times are compared. This is demonstrated using a molecular dynamics (MD) simulation with particles subject to the Lennard-Jones (L-J) potential or through experimental measurements of cholera toxin B subunit (CTxB) in isolated giant plasma membrane vesicles (GPMVs) (**Figure 11)**. The L-J potential is strongly repulsive for short particle separations ($r<\sigma$) and weakly attractive for larger separations ($\sigma< r<2\sigma$). $C(r, \langle\tau\rangle)$ tabulated from reconstructed images acquired over time yields a nearly uniform distribution, with $C(r, \langle\tau\rangle)$ close to 1 for all radii (magenta line in **Figure 11b**). The steady-state cross-correlation produced by tabulating $C(r, \tau=0)$ from pairs of particles detected simultaneously ($\tau=0$) reflects the actual co-distribution of particles (black line in **Figure 11b**), with exclusion at short radii ($C(r< \sigma)<1$) and enrichment at intermediate radii ($C(\sigma <r< 2\sigma)>1$). A similar observation is made when tabulating cross-correlation functions between single molecule localizations of two spectrally distinct pools of CTxB bound to GPMVs. CTxB partitions strongly into liquid-ordered domains[144] and is highly structured in a diffraction limited image of a phase separated GPMV acquired with a short (0.2 s) integration time (**Figure 11c**). Reconstructed images of single molecule localizations from the bottom surface of the same vesicle appear uniform since domains are mobile over the time-frame of the single molecule measurement (3 minutes). $C(r, \langle\tau\rangle)$ tabulated over all Atto 655 CTxB and Alexa 532 CTxB localizations also appears uniform, however significant cross-correlation is observed when $C(r, \tau=0)$ is calculated using only pairs of probes imaged simultaneously ($\tau=0$) (**Figure 11d** top panel). Both $C(r, \tau=0)$ and $C(r, \langle t\rangle)$ give uniform distributions for CTxB in a second GPMV that has a single liquid phase, since both populations of CTxB explore the entire vesicle surface over both short (0.2 s) and long (3 min) time-scales (**Figure 11e,f**).

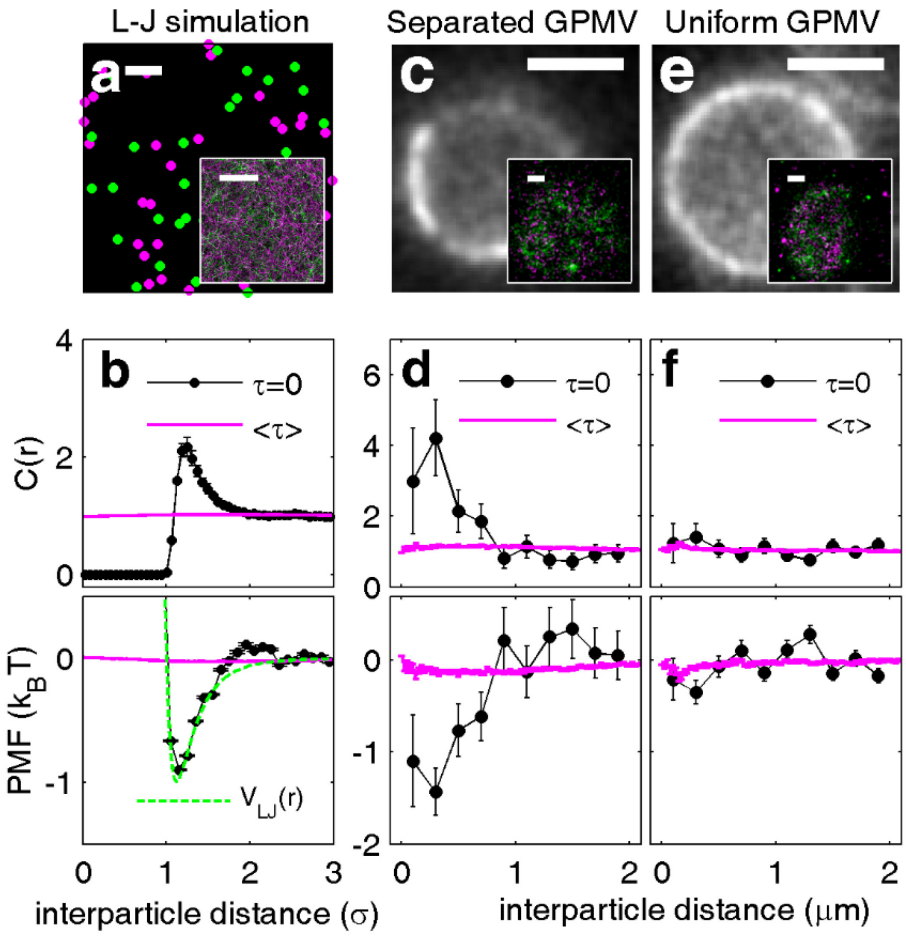

Figure 11: Steady state cross-correlations quantify mobile systems

(a) A snap-shot of a MD simulation of the Lenard-Jones potential. The inset shows a time-averaged reconstructed image of a subset of the simulation. Scale bars are 5σ. **(b)** The simultaneous (C(r, τ=0)) cross-correlation function detects more structure than the time-averaged (C(r, <τ>)) cross-correlation function in this mobile simulation, and the potential of mean force (PMF) tabulated from C(r, τ=0), but not C(r, <τ>), is in good agreement with the L-J potential present in this system. **(c, e)** Diffraction limited images of Alexa 532 CTxB bound to the surface of a GPMV with either coexisting liquid phases (c) or in a single liquid phase (e) acquired with a 0.2 seconds integration time. Two distinct pools of CTxB are simultaneously imaged in a STORM experiment; one conjugated to Atto 655 and the second to Alexa 532. Insets show reconstructed images of single molecule localizations acquired from the bottom surface of vesicles over 3 minutes, magenta for Atto 655 and green for Alexa 532. Scale bars are 5μm in large image and 1μm in inset. **(d, f)** C(r, τ=0) and C(r, <τ>) tabulated between Atto 655 and Alexa 532 localizations for the indicated vesicles. For the phase separated vesicle, C(r, τ=0) detects structure that is not apparent in the time-averaged C(r, <τ>) likely because domains are mobile. This corresponds to a long-range effective potential well of |PMF|>kBT. For the uniform vesicle (f), C(r, τ=0) and C(r, <τ>) both indicate a uniform distribution and a PMF that is indistinguishable from 0 at all radii. Error bars indicate the predicted standard deviation of C(r) as calculated in Equation 7.

This quantification method also yields a model independent measure of the effective interactions between labeled components, frequently referred to as the potential of mean force (PMF) under conditions where it can be reasonably approximated that probe organization is a result of an equilibrium process. The PMF is related to C(r) through $PMF(r) = -k_BT ln(C(r))$, where k_BT is the thermal energy. For the case of the MD simulation of **Figure 11**, the PMF calculated using $C(r, \tau=0)$ reproduces the original L-J potential up to small corrections that arise from many-particle interactions (**Figure 11b,** lower panel). In phase separated vesicles, the measured potential well is greater than k_BT out to separation distances of nearly 1 μm, consistent with the presence of phase separated domains at thermodynamic equilibrium (**Figure 11d,** lower panel). No significant PMF is observed between differently colored CTxB in the single phase vesicle shown in **Figure 11e,f**. We note that the detailed shape of either C(r) or PMF(r) can be used to distinguish models describing interactions between components[138].

3.2.2: Quantifying effective protein interactions in live B cells

We have also applied this analysis to quantify the co-distribution of Lyn kinase and a geranylgeranylated peptide with the B cell receptor (BCR) in the CH27 cell line, which endogenously expresses an IgM isotype of the BCR (**Figure 12a**). The BCR is a crucial component of the human adaptive immune system which is able to bind a wide array of pathogen and self-epitopes. Lyn and other *Src*-family kinases phosphorylate conserved tyrosine residues found in intracellular tyrosine activation motifs (ITAMs) associated with the receptor[22,28,196,197], and Lyn can bind to these phosphotyrosine residues via SH2 domains[22,28]. The association of Lyn with the B cell receptor has been detected using FRET microscopy in live cells[109]. However, the initiation of BCR phosphorylation by Lyn is not fully understood. It has been suggested[198] that Lyn is constitutively associated with BCR, or that Lyn is recruited to BCR only after antigen binding due to either a conformational change or BCR cluster-induced stabilization of ordered lipid domains.

Lyn and BCR were respectively labeled with photoactivatable mEos3.2[124] and a $f(Ab)_1$ fragment conjugated to both biotin and Atto 655[154]. An image reconstructed from all localized single molecule positions acquired after the addition of soluble streptavidin indicates that BCR is strongly self-clustered under this condition (**Figure 12a**), with streptavidin acting as an antigen against biotin labeled BCR. Evaluating $C(r, \tau=0)$ from a single cell dataset (**Figure 12b, top panel**) reveals that Lyn and BCR are weakly cross-correlated at short radii in the absence of antigen (-Ag) and correlations increase significantly in magnitude after antigen addition (+Ag), out to radii corresponding to the largest BCR clusters (200nm). The PMF obtained from $C(r, \tau=0)$ (**Figure 12b, lower panel**) indicates a weak attraction ($|PMF| \ll k_BT$) between BCR and Lyn prior to antigen addition, suggesting that the vast majority of Lyn is not bound to BCR in resting cells. A more significant attractive potential ($|PMF| \approx k_BT$) is found between these proteins after antigen addition, indicating robust Lyn recruitment to BCR clusters following antigen stimulation in agreement with previous reports using FRET[109]. We note that since our fluorophores do not distinguish between internal states of either protein, such as their phosphorylation state, the PMF should not be interpreted as the interaction strength between specific states of these proteins. Instead, it represents time and population weighted average over all states that are present in the system.

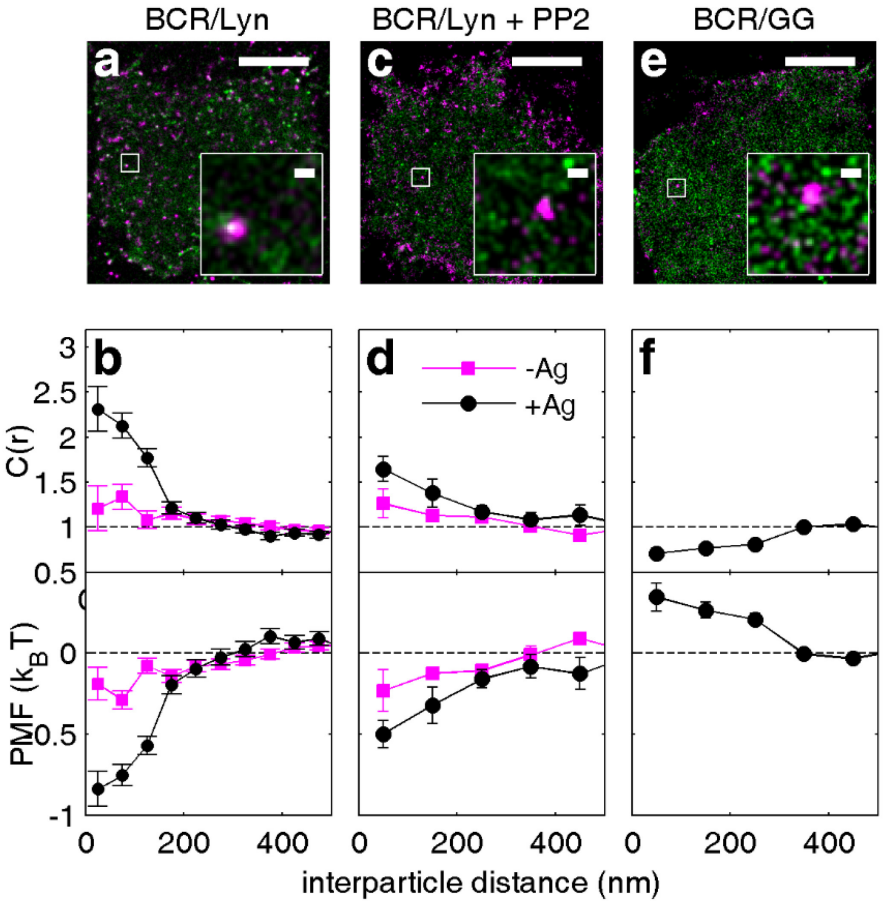

Figure 12: Steady state cross-correlations in live CH27 B cells

(a) Lyn (green) and BCR (magenta) localizations reconstructed into an image from raw data acquired for 4 minutes at room temperature after the addition of 5 μg/mL streptavidin (+Ag) which clusters and stimulates BCR labeled with biotin and Atto 655. **(b)** C(r, τ=0) and PMF(r) tabulated from localizations acquired 4 minutes prior to (-Ag) or 4 minutes following (+Ag) antigen addition in the same cell. Error bars indicate σC calculated from Equation 7. **(c)** Lyn and BCR imaged as in (a) but in the presence of 40 μM PP2, which reduces the magnitude of co-clustering between Lyn and BCR after antigen addition. **(d)** C(r, τ=0) tabulated for 5 distinct cells as in (b) then averaged to obtain statistical significance. Error bars are the standard error of the mean of C(r, τ=0) between the 5 cells and C(r, τ=0) for the cell shown in (c) is shown in **Figure 13**. **(e)** Reconstructed GG (green) and BCR (magenta) localizations acquired for 4 minutes after antigen addition. **(f)** C(r) from the cell shown in (e) tabulated by averaging over 0<τ<3s (100 image frames) to obtain statistical significance. We do not observe τ dependence of C(r, τ), as demonstrated in **Figure 14**, likely because GG does not directly interact with BCR and most BCR-clusters are not mobile over this time-frame. Error bars indicate the standard error of the weighted average as described in **Figure 14a,c,e** All scale bars are 5μm in large images and 200nm in insets.

Lyn-BCR co-clustering and the PMF between these components is reduced in cells imaged in the presence of the small molecule *Src*-family kinase inhibitor PP2 (**Figure 12c,d**), also in agreement with previous FRET results[109]. PP2 inhibits phosphorylation of the BCR by *Src*-family kinases, which includes Lyn, attenuating downstream signaling cascades and reducing the number and strength of potential binding sites between Lyn and BCR. Cross-correlations observed prior to antigen stimulation are comparable between control and PP2 treated cells, suggesting that this weak co-localization is not dependent on *Src*-family kinase phosphorylation. In order to obtain statistically significant correlations under this experimental condition, the curves presented in **Figure 12d** are generated by averaging results from 5 independent cells as shown in **Figure 13**.

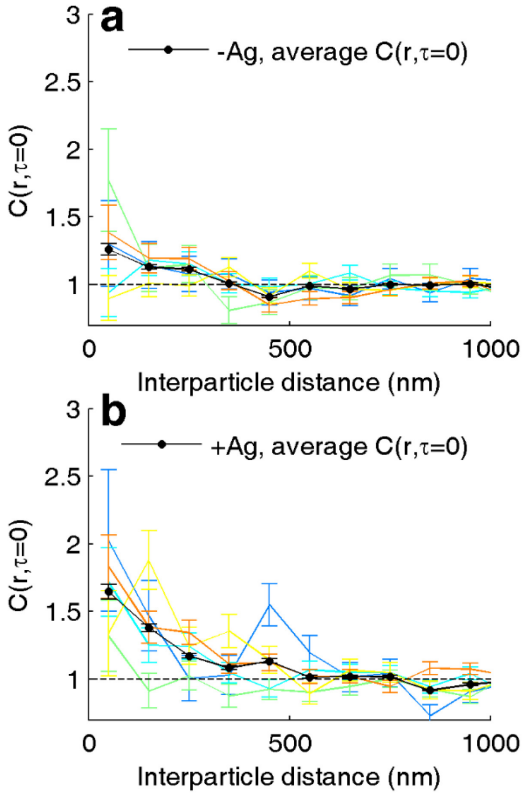

Figure 13: Averaging C(r, τ=0) between cells treated with PP2

Cells expressing Lyn-mEos3.2 and having BCR stained with Atto 655 were pretreated with PP2 for 5 minutes and then stimulated while performing a two-color super-resolution experiment in which the positions of BCR and Lyn were simultaneously collected. Data was collected from 5 cells, with 5000 frames of data collected before antigen stimulation (-Ag) and 5000 frames of data collected after antigen stimulation with streptavidin (+Ag). (a) C(r, τ=0) curves for 5 cells prior to antigen stimulation. Data from individual cells are plotted as colored lines with error bars given by σC and the average of all 5 cells is plotted as a black line with error bars corresponding to the standard error of the mean between the 5 cells. (b) C(r, τ=0) curves for 5 cells following antigen stimulation. Data from individual cells are plotted as colored lines with error bars given by σC and the average of all 5 cells is plotted as a black line with error bars corresponding to the standard error of the mean between the 5 cells. Although individual C(r, τ=0) curves are noisy, averaging individual curves together allows for more reliability when samples can be directly compared.

We additionally imaged a geranylgeranylated peptide (GG) conjugated to mEos3.2 simultaneously with Atto 655 labeled BCR to provide an example of exclusion in this system. GG is weakly excluded from BCR clusters formed after antigen binding, possibly due to steric repulsion from a crowded protein environment, electrostatic repulsion due to the polybasic stretch on this peptide, and/or a lipid-mediated repulsion due to the disorder-preferring geranylgeranylation modification[108] since BCR clusters are hypothesized to stabilize a more ordered local lipid environment[198]. In order to obtain statistical significance for this weak repulsion using data collected from a single cell, we evaluated C(r) by averaging over $0<\tau<3$s, corresponding to 100 image frames. This is appropriate in the case of antigen-clustered BCR since the partitioning of GG around BCR does not vary with τ, likely because BCR clusters do not diffuse a significant distance within this time-frame. It should be noted that this averaging approach will suppress any structure in the correlation function when $C(r, \tau)$ varies quickly with τ. Additional justification for using $C(r, \tau>0)$ to better determine $C(r, \tau=0)$ in this and alternate circumstances is described in **Methods Section 3.4.11 and Figure 14.**

There are quantitative differences between $C(r, \tau=0)$ compared to time-averaged $C(r, <\tau>)$ in chemically fixed samples which can be attributed to the presence of fluorophore bleed-through (**Figures 15,16,17**). Bleed-through occurs simultaneously in both channels, therefore it disproportionally affects $C(r, \tau=0)$ compared to $C(r, <\tau>)$. A similar increase in simultaneous vs. time-averaged C(r) is observed in simulations including a realistic level of bleed-through of mEos3.2 from the near-red to far-red emission channel, where bleed-through does not increase in the number of far-red localized positions but does bias the position of far-red localized centers (**Figure 16**). Several strategies for reducing the adverse effects of bleed-through are discussed in **Methods Section 3.4.11 and Figure 17.**

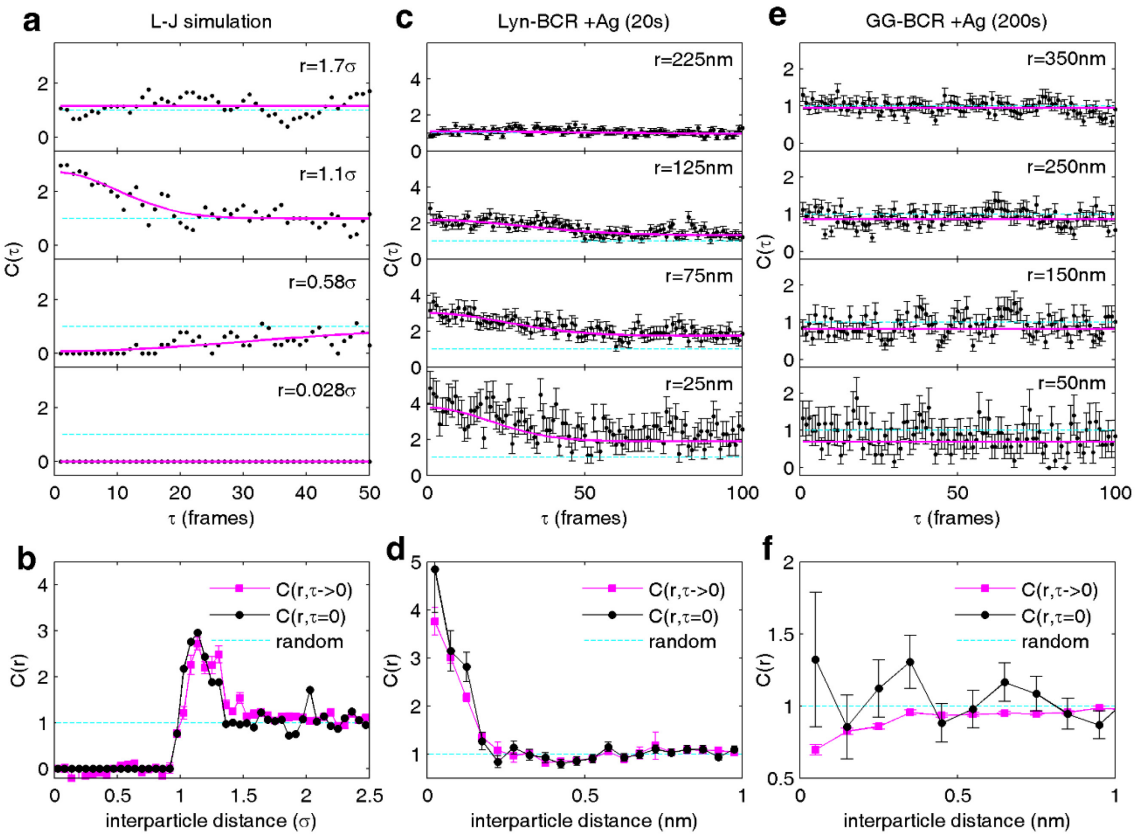

Figure 14: Using C(r, τ) to better define C(r, τ=0)

Tabulated values for C(r, τ) can be used to better specify the value at τ=0 if the dynamics of co-localization are slow compared to the frame rate of acquired data. **(a)** This approach is validated in MD simulations of the L-J potential, where C(r, τ) varies over tens of frames. Here, C(r, τ) was fit to a Gaussian shape in τ (magenta lines). **(b)** The best fit line evaluated at τ=0 (C(r, τ→0) is in good agreement with C(r, τ=0). **(c)** C(r, τ) for several r values tabulated from 500 image frames soon after addition of antigen for the same cell presented in **Figure 12a** and 3 with labeled BCR and Lyn. C(r, τ) varies slowly with τ and again is fit with a Gaussian shape, with weights given by $1/\sigma C^2$ (magenta lines). **(d)** The extrapolated C(r, τ→0) is in good agreement with the raw C(r, τ=0) but exhibits better signal to noise, where error bounds indicate one standard deviation in the Gaussian fit parameters. **(e)** C(r, τ) at several r values tabulated from 5000 frames after antigen addition for the cell shown in Fig 2e labeled GG and BCR. Interestingly, C(r, τ) does not decay with τ over 100 image frames (τ<3s). The magenta lines represent a weighted average over all 100 points, with weights given by $w=1/\sigma C^2$ (magenta lines). **(f)** The weighted average over τ produces a C(r, τ=0) that is much better specified than the raw C(r, τ=0), with error bounds given by $(1/\sum w)^{0.5}$. Note that in d and f, raw C(r, τ=0) are systematically higher than extrapolated C(r, τ→0) in the first spatial bin. This likely is a consequence of bleed-through between image channels, which only affect C(r, τ) at very short τ.

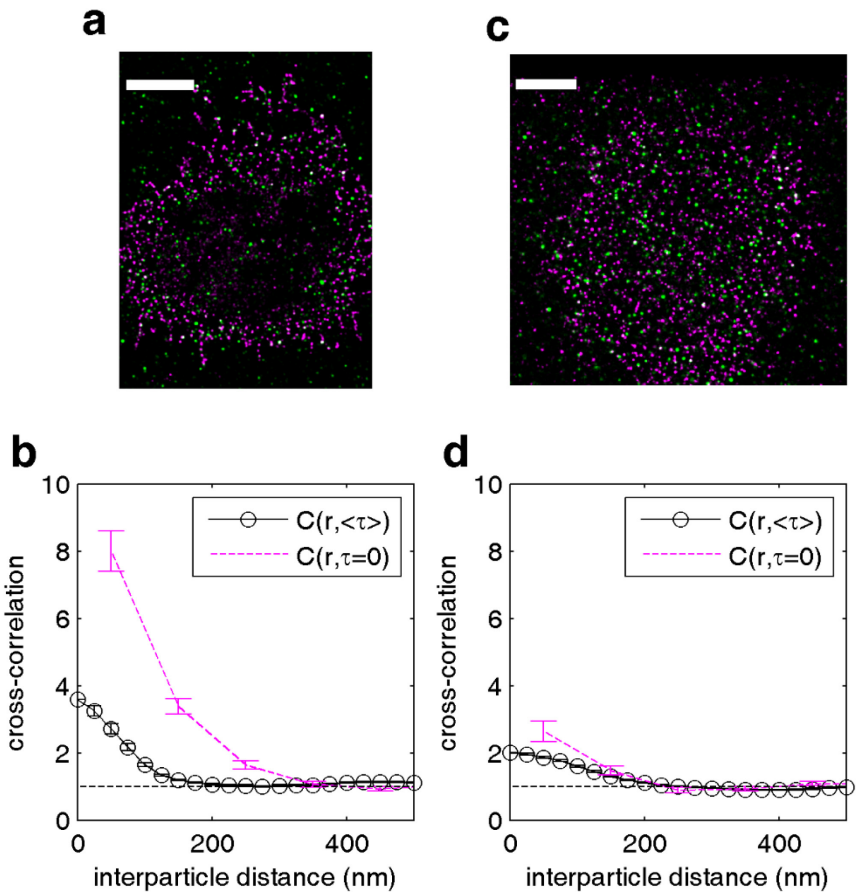

Figure 15: Overestimation of C(r, τ=0) in chemically fixed cells depends on probe pairs used.

(a) Reconstructed super-resolution image from simultaneous two-color imaging with Dyomics 654 labeled BCR and mEos3.2 labeled Lyn in a cell stimulated for one minute before chemical fixation. Magenta pixels represent Dyomics 654 localizations and green pixels represent mEos3.2 localizations. Scale bar is 5 μm. **(b)** Cross-correlation functions calculated from localized positions within the cell footprint. C(r, <τ>) is calculated by comparing all localizations in the entire experimental dataset, and C(r, τ=0) is calculated from only localizations that are imaged simultaneously in the same acquisition frame. Dramatic increases in C(r, τ=0) vs. C(r, <τ>) indicate that signals in the two channels are highly correlated in time, most likely due to bleed-through between spectral channels for this probe pair. **(c)** Reconstructed super-resolution image from simultaneous two color imaging with Atto 655 labeled BCR and mEos3.2 labeled Lyn in a cell stimulated for one minute before chemical fixation. Magenta pixels represent Atto 655 localizations and green pixels represent mEos3.2 localizations. Scale bar is 5 μm. **(d)** Cross-correlation functions calculated from localized positions within the cell footprint. C(r, <τ>) is calculated by comparing all localizations in the entire experimental dataset, and C(r, τ=0) is calculated from only localizations that are imaged simultaneously in the same acquisition frame. Error bars in (b) and (d) reflect σC. While C(r, τ=0) remains slightly elevated compared to C(r, <τ>) with the Atto 655 and mEos3.2 probe pair, it is reduced when compared to cells labeled with Dyomics 654 and mEos3.2, justifying the use of Atto 655 in these measurements.

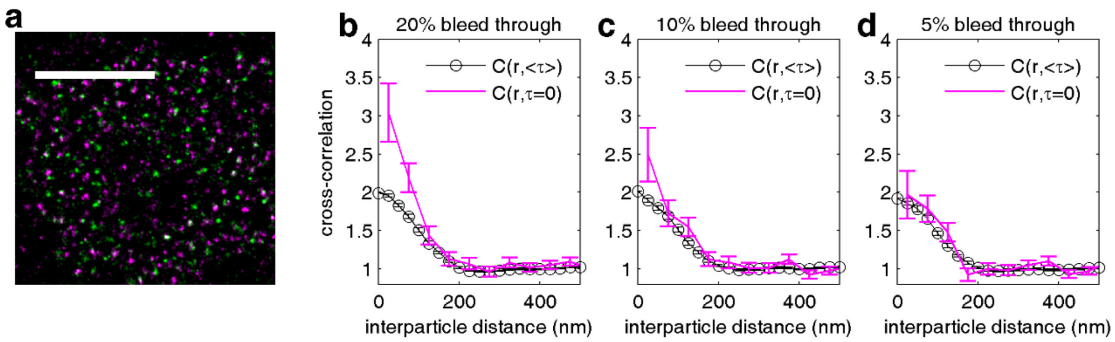

Figure 16: Simulated datasets confirm that bleed-through increases C(r, τ=0) while leaving time-averaged cross-correlations unaffected.

(a) An experimental co-distribution of Lyn (green) and BCR (magenta) was determined from two-color super-resolution microscopy of a chemically fixed CH27 cell where the BCR was labeled with Atto 655 and Lyn was labeled with mEos3.2. Scale bar is 5μm. **(b-d)** Steady state (C(r, τ=0)) and time-averaged (C(r, <τ>)) cross-correlation functions tabulated from simulated data with the specified bleed-through of mEos3.2 fluorescence emission intensity into the far-red acquisition channel with error bars given by σC. Simulated data was generated by randomly selecting localized positions to blink on and off with intensities and off-times sampled from experimentally determined distributions. Fluorophore fluorescence was simulated from experimental localizations using a diffraction limited point spread function, and additionally superimposing mEos3.2 bleed-through intensity at the specified level in the far-red channel. White noise mimicking experimental conditions was also included. Note that the time-averaged cross-correlations are unaffected by the presence of 5%-20% bleed through under these conditions, whereas C(r, τ=0) is increased at short radii due to the presence of 10% and 20% bleed through.

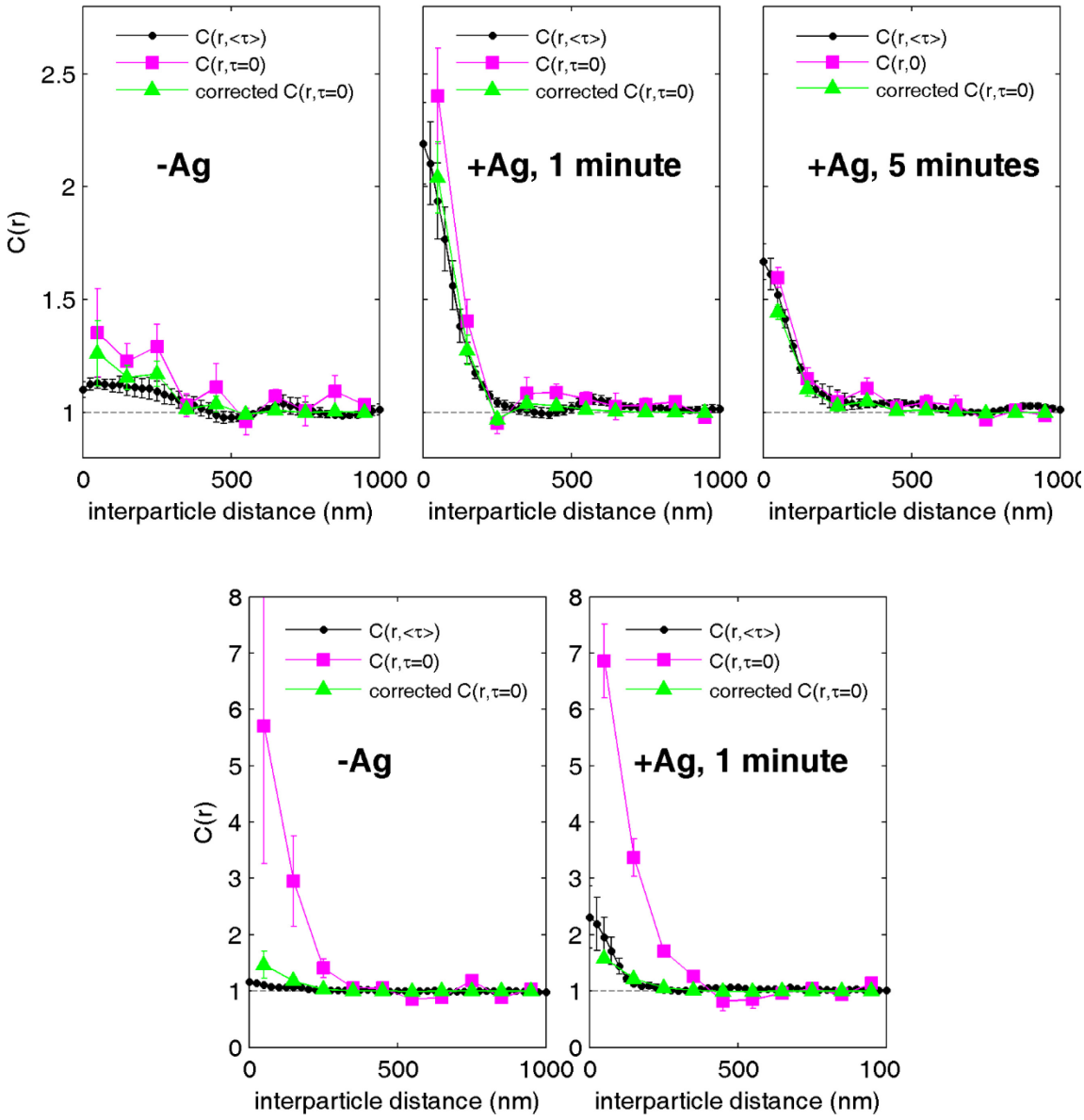

Figure 17: Bleed-through leads to an increase in measured C(r,τ=0) that is roughly proportional to the magnitude of the actual correlation function.

(top panels) Correlation functions averaged over chemically fixed cells (N=5 for left and center panel and N=4 for right panel) each chemically fixed either in the absence of antigen (left), after 1 minute of antigen stimulation (center), or after 5 minutes of antigen stimulation (right). Cells contain Atto 655 labeled BCR and mEos3.2 labeled Lyn. Bleed-through leads to a systematic increase in C(r, τ=0) compared to C(r, <τ>) that is roughly proportional to the magnitude of C(r, <τ>)-1. Here, the corrected C(r, τ=0) drawn is 0.75*(C(r, τ=0)-1)+1. **(bottom panels)** Correlation functions averaged over 3 cells chemically fixed either in the absence of antigen (left) or after 1 minute of antigen stimulation (right). Cells contain Dyomics 654 labeled BCR and mEos3.2 labeled Lyn. Here, the corrected C(r, τ=0) drawn is 0.1*(C(r, τ=0)-1)+1. Error bars represent σC.

3.2.3: Quantifying the dynamics of the BCR-Lyn interaction

The simultaneous cross-correlation approach described above can also reveal time-dependent changes in protein co-localization and dynamics by tabulating $C(r, \tau=0)$ over shorter steady-state time intervals (every 20 sec in **Figure 18a**). By monitoring only correlations for $r<50$nm vs time, it is apparent that Lyn becomes correlated with BCR shortly after antigen is added, concurrent with a dramatic reduction in BCR diffusion and a smaller reduction in Lyn mobility. The short-range correlations decay over 5 minutes following antigen stimulation, in good agreement with previous FRET results[109], findings in chemically fixed cells (**Figure 17),** and trends are reproducible over several live cell measurements (**Figure 19**).

Lyn kinase diffuses on the inner leaflet of CH27 cells at a faster rate than the BCR, thus a strong and long-lived binding of Lyn to BCR should be reflected as a reduced mobility of Lyn. Distributions of single trajectory diffusion coefficients show a reduction in both BCR and Lyn mobility after stimulation (**Figure 20**). We examined Lyn step-size distributions only including steps containing localized positions identified as correlated in the $C(r, \tau=0)$ analysis, meaning that they are observed within 50 nm of a simultaneously localized BCR. These correlated Lyn steps produce a distribution that closely resembles that observed for all Lyn steps prior to antigen addition, but shifts to shorter values after antigen addition to more closely resemble the distribution of all BCR steps (**Figure 18b**). The majority of correlated Lyn localizations after antigen stimulation are found within sections of Lyn trajectories that are transiently confined (**Figure 18c**). These findings indicate that most Lyn do not have long-lived (>0.1s) associations with the BCR in resting cells, but a subset of Lyn becomes associated with BCR after antigen stimulation.

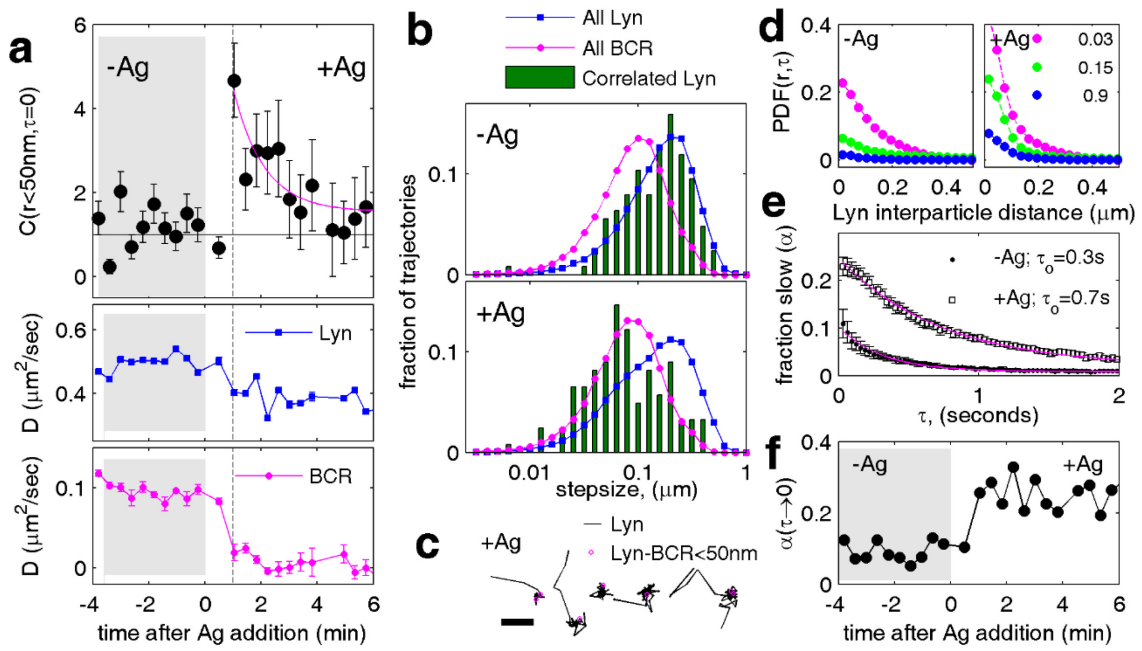

Figure 18: Correlation functions quantify the dynamics of BCR-Lyn co-localization in a single cell.

(a) C(r, τ=0) tabulated over 20 second steady-state time intervals both before and after stimulation with multivalent antigen for the single cell. The solid magenta line is meant to guide the eye and is not a fit to any theory. Increased BCR-Lyn co-localization is coincident with reductions in both BCR and Lyn average diffusion coefficients (D) extracted from single molecule trajectories as described in **Methods Section 3.4.3**. Error bars in the top panel indicate σC, as calculated from Equation 7. Error bars in lower two plots indicate the standard error in determining average D as described in **Methods Section 3.4.10**. **(b)** Distributions of BCR and Lyn displacements between sequential image frames (τ=0.03s) both before (-Ag) and after (+Ag) antigen stimulation for the single cell. Bars indicate the distribution of the subset of Lyn steps adjacent to localizations correlated with BCR satisfying C(r<50nm, τ=0). **(c)** Representative Lyn trajectories imaged after antigen addition show that correlated Lyn localizations (red circles) are found as trajectories are transiently confined. Scale bar is 1μm. **(d)** Probability distribution function (PDF) for correlated displacements occurring in a time-window τ calculated over 4 minute steady-state time intervals before (-Ag) and after (+Ag) antigen addition. Curves are fit to two Gaussian shapes (Equation 11) to extract MSD(τ) for each population as well as the fraction in the slower population (α(τ)) as described in **Methods Section 3.4.3**. **(e)** α(τ) decays with time and is well fit to a single exponential $\alpha(\tau) = \alpha(\tau \rightarrow 0)\exp(-\tau/\tau_o)$ (magenta lines) with τ_o longer after antigen addition. Error bars indicate one standard deviation in determining alpha from fits to the PDF. **(f)** An identical analysis conducted over 20 second steady state time-intervals shows the fraction of Lyn in the slowly diffusing pool as a function of stimulation time.

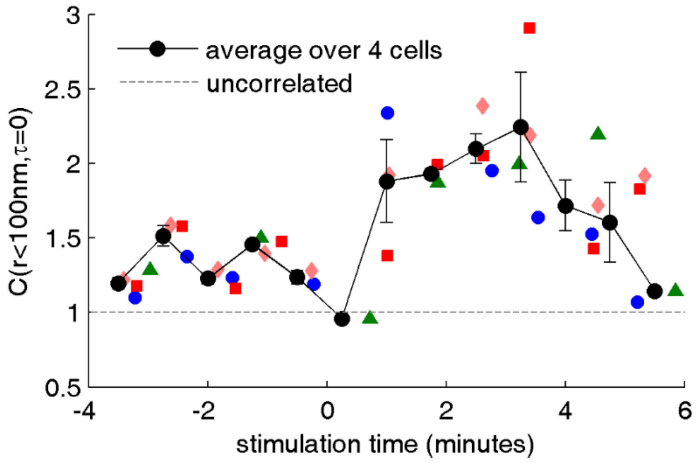

Figure 19: C(r, τ=0) through time between BCR and Lyn is consistent in four independent cells.

Time-course of the steady state cross-correlation of BCR and Lyn between 0 and 100 nm is plotted for 4 independent cells over steady-state time-intervals of 45 seconds. This time interval is approximately twice as large as that from the main text, due to differences in signal density between cells. Each cell is shown as a different color shape combination. The average of this time-course over all 4 cells is shown as solid black circles connected by lines, with error bars given by the standard error of the mean between the 4 cells. Zero stimulation time is when streptavidin was added to cluster and stimulate biotin-labeled B cell receptors.

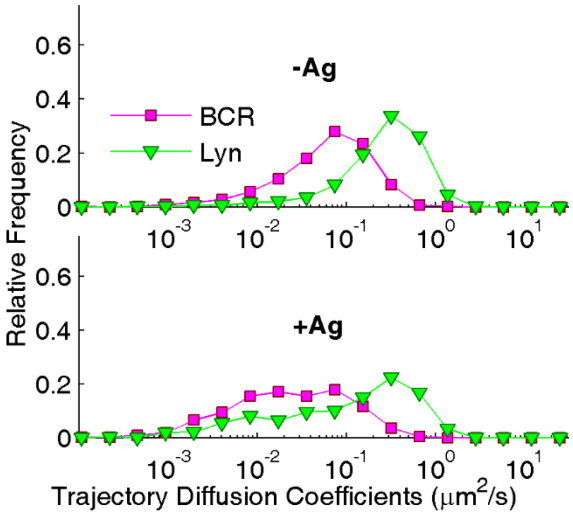

Figure 20: Distributions of trajectory diffusion coefficients for both BCR and Lyn are shifted to lower values following antigen stimulation

Mean squared displacements (MSD) as a function of time-interval τ for individual trajectories of BCR and Lyn were fit to linear regressions for τ between 2 and 4 frames. The determined slope was divided by 4 to give the diffusion coefficient of that individual trajectory. The histogram of these diffusion coefficients is shown for BCR and Lyn in both unstimulated and stimulated frames, indicated by –Ag and +Ag respectively and corresponding to prior or after the addition of streptavidin to cluster and stimulate B cell receptors. Prior to stimulation, Lyn and BCR trajectory diffusion coefficients are centered at 0.4 $\mu m^2/s$ and 0.05 $\mu m^2/s$ respectively (upper panel). After stimulation, BCR trajectory diffusion constants shift to lower diffusion coefficients. This behavior is also seen in trajectory diffusion coefficients for Lyn, however the majority of diffusion coefficients from Lyn trajectories are unaffected by stimulation (lower panel).

The same data used to tabulate spatial correlations between proteins can also be used to quantify protein mobility. The time-resolved auto-correlation function, G(r, τ), is tabulated from localized positions of the same fluorophore type detected at different times and is a convenient measure of the time evolution of particle motion without the need to identify single particle trajectories. This is a localized particle variation of STICS[188] similar to PICS[199] but G(r, τ) is normalized to yield the probability density function (PDF) for correlated steps of displacement r in a time-interval τ. PDF(r, τ) at fixed τ for a single population of diffusers is a Gaussian with width equal to the mean squared displacement (MSD). PDF(r, τ) of Lyn were fit to models containing slow and fast diffusing populations (**Figure 18d and Methods Section 3.4.3**) yielding the MSD of each population and the fraction of diffusers in the slow population (α) as a

function of τ. Diffusion coefficients of Lyn determined by fitting these MSD(τ) are in good agreement with those determined by trajectory MSD analysis (**Figure 21**). α decreases with τ, with a decay time of 0.3 sec prior to BCR stimulation and 0.7 sec following BCR stimulation (**Figure 18e**). Since the slowly diffusing Lyn population is likely bound to BCR or other slowly diffusing adaptor proteins, this decay likely indicates the off-rate of Lyn binding to targets associated with the BCR signaling complex. Finally, the fraction of steps belonging to the slow population extrapolated to zero time-lag, $\alpha(\tau \rightarrow 0)$, is the fraction of Lyn localizations associated with the slower diffusing pool. **Figure 18F** shows that this switches from 9±3% prior to antigen stimulation to 25±6% after stimulation, and does not exhibit the decay at late stimulation times observed for C(r, τ<50nm) shown in **Figure 18a**. This suggests that Lyn associates with other slowly moving components that are spatially distinct from BCR at later stimulation times, consistent with Lyn's roles in phosphorylating other components during BCR stimulation such as CD19, CD22, and FcγRIIB[22].

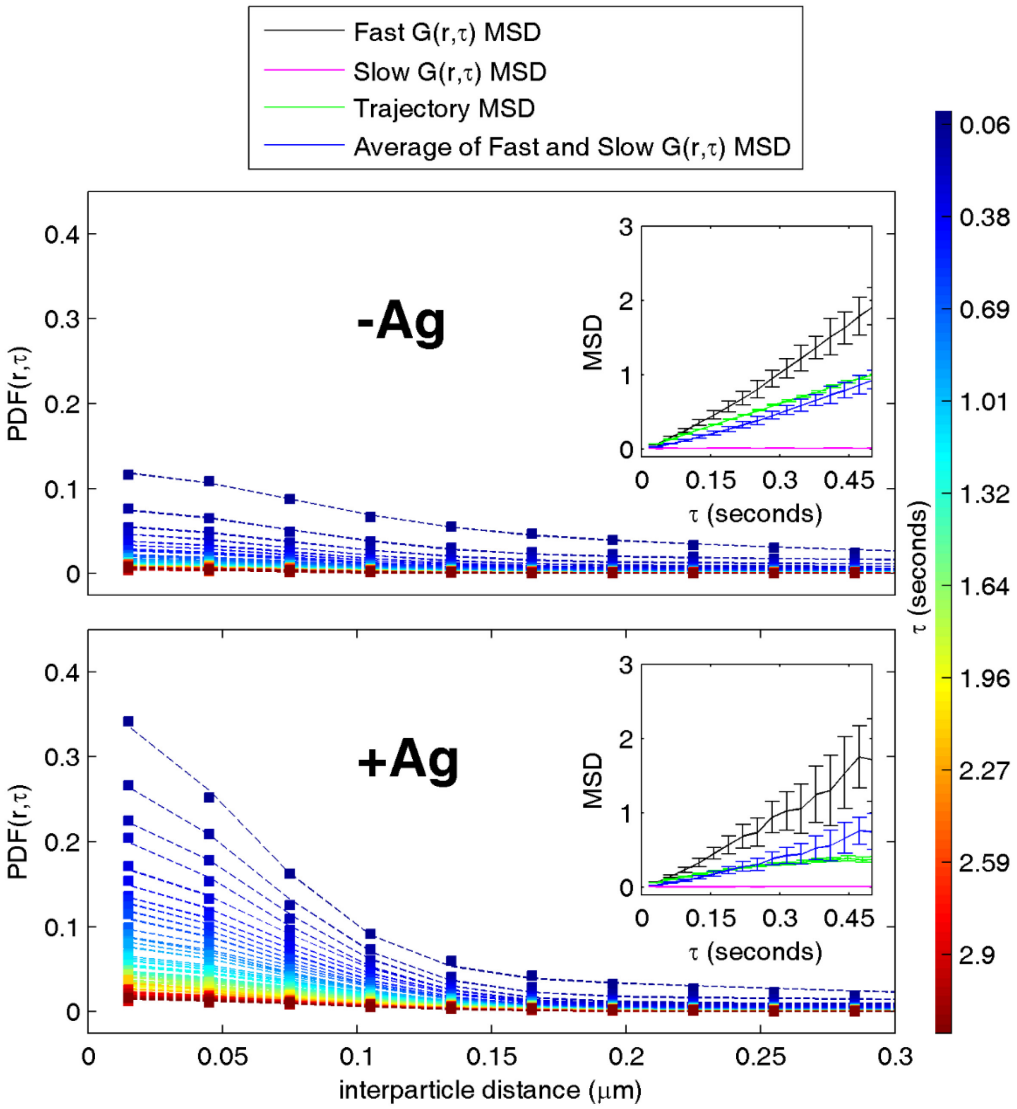

Figure 21: MSDs determined from Gaussian fitting of PDF(r,τ) are in good agreement with MSDs determined from trajectory analysis

Experimentally determined probability distribution functions (PDFs) are determined from the auto-correlation of Lyn positions through time G(r,τ) as described in **Methods Section 3.4.3**. PDF(r,τ) is fit well by two Gaussian functions (Equation 11), where the Gaussian width reports on the MSD of that population of diffusers, and a parameter α reports the fraction of segments in the slow population. Raw PDF(r,τ) is shown as squares colored by τ, and Gaussian fits are shown as dotted lines also colored by τ. This MSD was used to quantify the diffusion of each population using MSD vs time curves, as shown in the inset. Black curves show the MSD from the fast population, magenta curves show the MSD from the slow population, and green curves show the MSD tabulated from trajectories. Blue curves show the average of the fast and slow population weighted by α. Colorbar on the right indicates the time lag between frames, τ, for the correlation functions G(r, τ). –Ag and +Ag, respectively, corresponding to prior or after the addition of streptavidin to cluster and stimulate B cell receptors. Error bars in black, magenta, and blue curves in inset are indicate one standard deviation of the MSD parameters from Gaussian fits to the PDF(r, τ). Error bars in the green curve are given by the standard error in the slope of the line fit to the 2nd through 4th points of the MSD tabulated from all trajectories in the time window.

3.3: Discussion

We present an analytical method to quantify the co-distribution and dynamics of labeled molecules in super-resolution localization measurements without reconstructing images or trajectories, enabling robust measurement of co-distributions in single cells exhibiting high mobility. This adds to an existing set of analysis methods based on spatial auto- and cross-correlations[161,187,188] with specific applicability to point localized stochastically blinking probes commonly used in super-resolution fluorescence localization datasets. Here, we apply this methodology to quantify interactions between membrane bound components, but in principle this methodology could be applied to a range of systems including those imaged in one or three dimensions.

When applied to measurements of the B cell receptor and Lyn kinase in live cells, we find that these proteins are only weakly associated prior to antigen stimulation, providing evidence against a model where a large fraction of Lyn is constitutively associated with BCR in the resting cell[198]. Instead, Lyn is observed to transiently co-localize with BCR soon after the addition of multivalent antigen, with single Lyn proteins dwelling with an off-rate of 0.7 seconds. On average, the population of Lyn associating with BCR is greatest at short times after stimulation then decreases over several minutes. This is consistent with Lyn's role as a mediator of early signaling events and is in excellent agreement with previous findings obtained by FRET[109]. One advantage of this approach over past FRET measurements in this system is the ability to estimate interaction energies between proteins, and we observe that the potential well attracting BCR and Lyn has depth of roughly the thermal energy over a range of 100 nm. Interestingly, Lyn is still recruited to BCR clusters in the presence of the inhibitor PP2, although to a weaker extent, suggesting that there are interactions between BCR and Lyn beyond SH2 binding to phosphorylated ITAMs within BCR. Overall, this work emphasizes the complexity of Lyn-BCR interactions as well as the power of super-resolution localization microscopy to probe the organization and dynamics of protein interactions in intact cells.

3.4: Methods

3.4.1: Calculating correlation functions

Cross-correlation functions are tabulated by first computing the distances between pairs of distinguishable localized molecules, then constructing a histogram with these distances by separating into discrete bins covering different ranges of radii, then finally normalizing this histogram to account for the different areas associated with each bin and effects that arise due to the finite size of the region of interest being analyzed. These steps are illustrated graphically in **Figure 7b** for the example of an image reconstructed from BCR and Lyn localizations in a chemically fixed cell, and are described in detail below.

Within a region of interest (ROI) of an image, the total number of distinct pairwise distances between distinguishable localizations is N = $n_1 \times n_2$ where n_1 is the number of localizations of one colored probe and n_2 is the number of localizations of the second colored probe. These N distances are computed, and then discretized into bins centered at radii r with width Δr, which sets the resolution of the cross-correlation. Here, we call this histogram M(r). M(r) tends to increase in magnitude with increasing radius since the two dimensional area associated with each radii bin is a ring with area of $\Delta A(r)=2\pi r\Delta r$. A larger associated area means that there is a greater likelihood of finding pairs separated at larger distances even if particles are randomly distributed. The total area associated with each radii bin also depends on the detailed shape of the ROI being analyzed, again with larger area bins being more affected. To account for this, we assemble a normalization factor μ(r), which is the expected M(r) histogram that would be measured if all particles are uniformly distributed over the ROI: $\mu(r) = \Delta A(r)\rho_o W(r)$. The average density of pairwise distances over the whole area is given as $\rho_o = N/A_{ROI}$, where A_{ROI} is the total area of the ROI. W(r) is the radially averaged autocorrelation of the ROI which corrects for the region of interest having shape that contributes to the cross-correlation, and is computed using fast Fourier transforms (FFTs) as described previously[138]. The cross-correlation function C(r) is the relative probability of finding a pair separated by a distance r compared to a random distribution, can then be simply expressed as:

$$C(r) = \frac{M(r)}{\mu(r)} \qquad \textit{Equation 4}$$

Pair cross-correlation functions describing the co-distribution of proteins can also be constructed using FFTs of the reconstructed image[138,139]. **Figure 7e** demonstrates that C(r) evaluated by both methods is equivalent.

The steady-state simultaneous cross-correlation, C(r, τ=0), is tabulated as described above, but M(r) histograms are assembled using only particle localizations that are detected simultaneously over a steady state time-interval. In this case, this histogram is normalized as above, using the total number of pairwise distances between red and green localized particles given by:

$$N = \sum_{i=1}^{F} n_{1,i} \times n_{2,i} \qquad \textit{Equation 5}$$

Where F is the number of image frames included in the steady-state time-window, and $n_{1,i}$ and $n_{2,i}$ are the number of localizations of the first and second fluorophore type in the i^{th} image frame. C(r, τ) is tabulated in the same way as for C(r, τ=0), but by measuring pairwise distances between fluorescent localizations separated by a time-interval τ. G(r, τ) measures correlations between localizations of the same fluorophore type observed with time-lag τ. It is tabulated by the method described above for C(r, τ), but pairwise distances are measured between localizations of the same colored probe. Note that G(r, τ=0) is a measure of the average density of probes and not a measure of self-clustering and is typically disregarded. Matlab code that tabulates C(r, τ) and G(r, τ) and associated statistical variances from point localization data is included in reference 200.

3.4.2: Determining statistical variance of correlation functions

Variance in C(r, τ) (σ_C^2) arises from statistical variance in the number of pairs associated with each spatial bin (M(r)) as well as the number of total pairs identified (N) over some integration time. Since M and N are independent variables, the σ_C^2 can be determined through simple error propagation:

$$\sigma_C{}^2 = \left|\frac{\partial C}{\partial M}\right|^2 \sigma_M{}^2 + \left|\frac{\partial C}{\partial N}\right|^2 \sigma_N{}^2 \qquad \textit{Equation 6}$$

σ_M^2 and σ_N^2 are given by M and N respectively, as is expected from Poisson counting statistics and verified in experimental data on chemically fixed cells in **Figure 8a**. For datasets with reduced sampling, it may be appropriate to approximate σ_M^2 as M+1 to provide a finite estimate of error when spatial bins contain no pairs. Using the definition of C(r) given in Equation 4, this becomes:

$$\sigma_C(r)^2 = \frac{M(r)}{\mu(r)^2} \qquad \textit{Equation 7}$$

The variance in C(r) is well described by Equation 7, as exemplified through data from fixed cells or resampling the molecular dynamics simulation. Point localization data acquired in chemically fixed cells was re-sampled after first scrambling the time-ordering of frames to remove additional contributions to σC that arise from probe photo-bleaching and/or fluorophores localizations being otherwise correlated in time. Values of M(r) and N were recorded and C(r,τ=0) was tabulated over steady-state time windows with constant number of scrambled frames. The standard deviation of M(r) is well described by the square root of M(r), as shown in **Figure 8a**. Additionally, the standard deviation of C(r) is well described by the variance given in Equation 7, which holds independent on the values of C(r), as evidenced by examining a cell chemically fixed without antigen as well as a cell chemically fixed after incubation with antigen for 1 minute (**Figure 8b**). We performed a similar validation using a simulated super-resolution microscopy experiment of the Lennard-Jones MD simulation by assigning a probability that a particle is on, P_{on}, as illustrated in **Figure 8c**. σC is estimated by resampling the simulation 15 times for each P_{on}, changing the identity of red and green particles for each resampling. C(r, τ=0) is tabulated from each resampled simulation and the standard deviation is used to estimate variance. We find good agreement between the measured variance and the predicted variance determined in Equation 7, as illustrated in **Figure 8d**.

The predicted relative error in a measurement, σC(r)/C(r), is given by:

$$\frac{\sigma C(r)}{C(r)} = \sqrt{\frac{1}{M(r)} + \frac{1}{N}} \qquad \textit{Equation 8}$$

3.4.3: Quantifying single molecule mobility with correlation functions

Normalizing G(r, τ) such that the total two dimensional area under the curve is set to one produces a probability distribution function (PDF) describing single molecule displacements r over a time lag τ.

$$PDF(r,\tau) = {G(r,\tau) - 1}\Big/{\sum(G(r,\tau) - 1)2\pi r\Delta r} \qquad \textit{Equation 9}$$

The PDF for 2 dimensional Brownian diffusion is a normalized Gaussian function with center at zero with a width equal to the mean squared displacement which defines the diffusion coefficient, D, according to MSD=4Dτ, where MSD is the mean squared displacement MSD= $<|r(\tau)-r(0)|^2>$.

$$PDF(r,\tau) = \frac{1}{4\pi D\tau} \times e^{\frac{-r^2}{4D\tau}} \qquad \textit{Equation 10}$$

The PDF for two populations of diffusers can be written as a summation of two independent normalized Gaussians with associated diffusion coefficients D_1 and D_2, and a parameter α describing the fraction of segments associated with the diffusion coefficient D_1.

$$PDF(r,\tau) = \alpha \frac{1}{4\pi D_1\tau} \times e^{\frac{-r^2}{4D_1\tau}} + (\alpha - 1)\frac{1}{4\pi D_2\tau} \times e^{\frac{-r^2}{4D_2\tau}} \qquad \textit{Equation 11}$$

Matlab software for calculating C(r, τ) and G(r, τ) and associated statistical variances from point localization data is available in reference 200.

3.4.4: Molecular dynamics simulation

A molecular dynamics simulation was performed utilizing the Lennard-Jones (L-J) potential with particle motions constrained to two dimensions. A system of 64 atoms was created with a reduced density of 0.05 atoms per unit area, giving a side length close to 36σ. Periodic boundary conditions were enforced, and the temperature of the simulation was adjusted by setting the initial velocities to a Gaussian distribution of magnitudes. Positions were propagated using the Verlet algorithm, and a timestep of 0.005 (reduced time) was used. The starting configuration maximized space between atoms, and the simulation was allowed to equilibrate for 40,000 steps before molecular positions were tracked. A total of 200,000 time steps were taken in each simulation run, and the positions of atoms were saved every 5 time steps, giving 40,000 snapshots of atomic positions to use in the TRXC analysis. The atoms were randomly divided into two equal groups displayed as green and red fractions. Simulation and analysis were carried out in MATLAB (The MathWorks).

3.4.5: $f(Ab)_1$ and cholera toxin subunit B modification

$f(Ab)_1$ fragment goat antibody to mouse IgM, μ chain specific (Jackson Immuno Research, West Grove, PA, item number 115-007-020) was simultaneously chemically modified with Atto 655 NHS ester (Sigma, St. Louis, MO) and Biotin-X, SSE, 6-((Biotinoyl)Amino)Hexanoic Acid, Sulfosuccinimidyl Ester, Sodium Salt (Sulfo-NHS-LC-Biotin) (Invitrogen, Grand Island, NY). Modifications were carried out in aqueous solution buffered by 0.01 M NaH_2PO_4 with 0.01 M NaH_2CO_3, with 23 μM $f(Ab)_1$ in the presence of 47 μM Atto 655 NHS ester and 140 μM Biotin–X SSE, at pH 8.2 for thirty minutes at room temperature. Reaction products were separated by gel filtration on Illustra NAP-5 columns (GE Healthcare, Piscataway, New Jersey) to remove unbound dye from labeled protein. Labeled $f(Ab)_1$ was conjugated to additional Atto 655 in the same manner as above using 10 μM $f(Ab)_1$ in the presence of 140 μM Atto 655, and unbound dye was again separated using gel filtration. Labeled $f(Ab)_1$ fragment was then spun down at 20,000 x g for 90 minutes at 4°C to remove any protein aggregates. We determined the average number of Atto 655 dye molecules per $f(Ab)_1$ fragment to be 1.6 from absorbance measurements using a NanoDrop 2000 (Thermo Scientific, Rockford, IL). The average number of biotin per $f(Ab)_1$ was determined to be 0.8 using the FluoReporter Biotin Quantification Kit (Invitrogen).

Cholera toxin subunit B (CTxB) (Sigma Alderich, St. Louis, MO) modifications were carried out in aqueous solution buffered by 0.01 M $Na_2B_4O_7$ with 0.150 M NaCl, with 19 μM CTxB in the presence of 80 μM reactive dye, either Atto 655 NHS ester or Alexa 532 NHS ester, at pH 8.2 for 30 minutes at room temperature. Reaction products were separated by gel filtration on Illustra NAP-5 columns (GE Healthcare, Piscataway, New Jersey) to remove unbound dye from labeled protein. Labeled CTxB was then spun down at 20,000 x g for 90 minutes at 4°C to remove any protein aggregates. We determined the average number of dye molecules per CTxB to be around 3 for both Atto 655 and Alexa 532 conjugated CTxB.

3.4.6: GPMV preparation

GPMVs were prepared through incubation of RBL-2H3 cells with low concentrations of dithiothreitol (DTT, 2mM) and formaldehyde (25mM) in the presence of calcium (2 mM) for 1 hour at 37°C consistent with previous work[201]. Prior to GPMV formation, cells were labeled with two distinct pools of CTxB for 10 minutes at room temperature, 0.4 μg/ml conjugated to Atto 655 and 0.1 μg/ml conjugated to Alexa 532.

3.4.7: Cells, transfection, and fixation

CH27 cells were a generous gift from Neetu Gupta (Cleveland Clinic, Lerner Research Institute) and were maintained in low glucose DMEM (Life Technologies, Carlsbad, CA) containing 15% FBS (Mediatech, Manassas, VA), 10 mM HEPES, 110 mg/L sodium pyruvate, 50 μM BME, and 1% Pen/Strep in 5% CO_2 at 37°C.). CH27 cells were transiently expressing either Lyn protein containing a C terminal fusion to the mEos3.2 photoactivatable fluorescent protein or a 20 amino acid sequence, here called GG, coding for a polybasic stretch and C terminal geranylgeranylation and N terminal fusion to mEos3.2. 500,000 CH27 cells were transfected with .5 μg mEos3.2 tagged plasmid DNA in Clontech N1 or C1 vector (Clontech, Mountain View, CA) using Lonza Nucleofector electroporation (Lonza, Basel, Switzerland). Plasmid DNA encoding for full length Lyn protein and mEos3.2 have been described previously[202], and the GG plasmid described previously[108] was cloned to include mEos3.2. Cells were plated at 100,000 / ml and grown overnight on glass bottom wells (MatTek Corporation, Ashland, MA). Endogenous BCR in the plasma membrane was labeled with a modified $f(Ab)_1$ fragment conjugated to both Atto 655 and

biotin by staining with 10 μg/ml labeled $f(Ab)_1$ for ten minutes at room temperature in growth media followed by extensive washing with phosphate buffered saline (Life Technologies) prior to imaging. Cells were stimulated by clustering $f(Ab)_1$ biotin Atto 655 conjugate labeled IgM with with 5μg/mL soluble streptavidin. This labeling and activation scheme preserves signaling functionality under our imaging conditions, as indicated by increased tyrosine phosphorylation and calcium mobilization after the addition of antigen (**Figure 22)**. For fixed cells, CH27 cells were transfected with Lyn-mEos3.2 and BCR was stained with modified $f(Ab)_1$ fragment as described above prior to holding in control buffer (135 mM NaCl, 5 mM KCl, 1 mM MgCl2, 1.8 mM CaCl2, 5.6 mM glucose, 20 mM HEPES) at room temperature during addition of streptavidin (Life Technologies) at 5 μg/ml to stimulate cells. Cells were then washed extensively in phosphate buffered saline before chemical fixation with 4% formaldehyde and 0.01% gluteraldehyde (Ted Pella Inc, Redding, CA) for 10 minutes at room temperature.

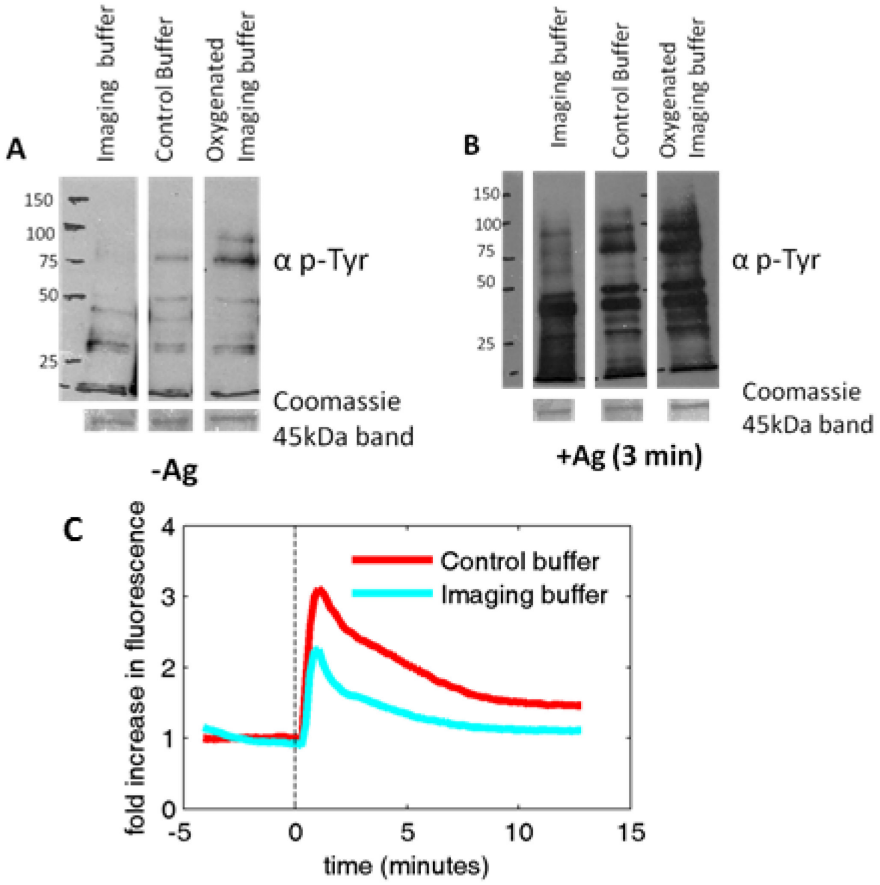

Figure 22: Antigen induced phosphotyrosine and calcium mobilization is retained in CH27 cells under imaging conditions

a) Total phosphotyrosine western blot of CH27 lysates from unstimulated cells. IgM was labeled with IgM specific f(AB)$_1$ conjugated to biotin, and lysates were prepared from cells in either full imaging buffer, a control buffer, or the imaging buffer without oxygen scavenging enzymatic system as described in **Methods Section 3.4.9**. Molecular weight marker is shown at left. Coomassie stain of blot is shown at bottom, indicating total protein content for each lane is constant. Some higher molecular weight proteins have less phosphotyrosine staining in the full imaging buffer condition compared to the control buffer, however normal phosphotyrosine staining is recovered by using imaging buffer without the oxygen scavenging system. **b)** Phosphotyrosine western blot of CH27 lysates from cells 3 minutes after addition of 5 µg/ml streptavidin to stimulate BCR. Molecular weight marker is shown at left. Coomassie stain of blot is shown at bottom, indicating total protein content for each lane is constant. As in unstimulated cells, some higher molecular weight proteins have less phosphotyrosine staining in the imaging buffer condition compared to control buffer, however normal phosphotyrosine staining is recovered by using imaging buffer without the oxygen scavenging system. **c)** Cytoplasmic Ca^{2+} mobilization time-course from CH27 cells suspended in control and full imaging buffers, as indicated using Fluo-4 fluorescence intensity. Cells exhibit Ca^{2+} mobilization in both buffer conditions, although is attenuated in the full imaging buffer

3.4.8: TIRF microscopy

Imaging was performed on an Olympus IX81-XDC inverted microscope with a cellTIRF module, a 100X UAPO TIRF objective (NA=1.49), active Z-drift correction (ZDC) (Olympus America, Center Valley, PA). Images were acquired on an iXon-897 EMCCD camera (Andor, South Windsor, CT). Excitation of Atto 655 was accomplished using either a 647 nm diode laser for live-cell measurements (OBIS 647 LX-100FP, Coherent, Santa Clara, CA) or a 641 nm diode laser for GPMV measurements (CUBE 640-75FP, Coherent). Excitation of Alexa-532 was accomplished using a 532nm diode laser (150mW Samba, Cobolt, Sweden), and excitation of mEos3.2 constructs was accomplished using a 561 nm diode laser (Sapphire 561 LP, Coherent). Photoactivation of mEos3.2 was accomplished with a 405 nm diode laser (CUBE 405-50FP, Coherent). Laser intensities were adjusted such that single fluorophores could be distinguished in individual images. Excitation and emission was filtered using the quadband dichroic mirror ET-405/488/561/647 (Chroma, Bellows Falls, VT) for both mEos3.2/Atto 655 and mEos3.2/Dyomics 654 fluorophore pairs or filtered using ET-405/488/532/640 for Alexa 532/Atto 655 fluorophore pair. Emission was split into two channels using a DV2 emission splitting system (Photometrics, Tuscon, AZ) using a T640lpxr dichroic mirror to separate emission, ET605/52m to filter near-red emission, and ET700/75m to filter far-red emission (Chroma).

Live cells were imaged in a live cell compatible imaging buffer: 30 mM Tris, 100 mM NaCl, 5 mM KCl, 1 mM $MgCl_2$, 1.8 mM $CaCl_2$, 50 mM glucose, 12 mM glutathione, 40 µg/ml catalase (Sigma), 500 µg/ml glucose oxidase (Sigma), pH 7.5. Where noted, cells were treated with 40 µM PP2 (Invitrogen) in live cell compatible imaging buffer for five minutes prior to and during antigen stimulation Fixed cells were imaged in buffer with higher buffering capacity, glucose concentration, and pH: 50 mM Tris, 550 mM glucose, 10 mM NaCl, 12 mM glutathione, 40 µg/ml catalase, 500 µg/ml glucose oxidase, pH 8.5. GPMVs were diluted 1:1 into live cell compatible imaging buffer. A small quantity of water (5%) was also added to better match the osmolarity of the GPMV and imaging buffers. GPMVs were imaged using off-TIR excitation between two #1.5 coverslips with a vacuum grease spacer and attached to a home-built Peltier-

based temperature stage coupled to a PID controller (Oven Industries, Mechanicsburg, PA), consistent with previous work[201] .

3.4.9: Western blots and Ca^{2+} mobilization

CH27 cells were incubated with 10 μg/ml of goat anti-mouse IgM μ-chain specific $f(Ab)_1$-biotin fragment (Jackson) for 10 minutes to label the IgM with biotin and then subsequently washed twice by centrifugation. One million CH27 cells were each suspended in either control buffer (defined above), live cell imaging buffer (defined above), or imaging buffer without oxygen scavenging enzymes glucose oxidase and catalase. Some cells were stimulated by the addition of 5 μg/ml streptavidin. Cells were lysed at room temperature using RIPA buffer (EMD Millipore, Billerica, MA) in the presence of Halt Phosphatase Inhibitor Cocktail (Thermo Scientific) and Complete Mini Protease Inhibitor Cocktail (Roche, Basel, Switzerland). Cell lysates were centrifuged at 16,000 x gravity for 15 minutes at 4°C. Supernatants were run on a denaturing SDS-PAGE gel, 7.5% Mini-PROTEAN gel (Bio-Rad, Hercules, CA) and then transferred to an Immobilon-P PVDF transfer membrane with 0.45 pore size (Millipore). Blots were stained with a 1:2000 dilution of mouse IgG2b 4G10 Platinum anti-phosphotyrosine antibody (Millipore, catalog number 05-321) and subsequently stained with a 1:5000 dilution of peroxidase conjugated goat anti-mouse IgG2b specific secondary antibody (Jackson Immuno research, catalog number 115-035-207). Blots were sensitized using SuperSignal West Pico chemiluminescent substrate and developed on Amersham Hyperfilm ECL (GE Healthcare Biosciences, Piscataway, NJ). Ca^{2+} mobilization assays were performed by incubating 3 million CH27 cells per ml with 2 μg/ml Fluo-4, AM (Life Technologies) in the presence of 0.25 mM sulfinpyrazone for 5 minutes at room temperature and then diluting to 0.2 million cells per ml in the same buffer for 30 minutes at 37°C. Cells were washed twice by centrifugation and resuspended in either control buffer or imaging buffer. CH27 IgM was labeled with biotin as above and then cells were loaded into wells 96 well black plates at a concentration of 2 million per ml and fluorescence was assayed by exciting the cells with 485 nm light and collecting 520 nm light in the Omega PolarStar (BMG Labtech, Ortenberg, Germany).

3.4.10: Single molecule analysis

Single molecule fluorescent events were localized by fitting local maxima in background subtracted images to Gaussian functions, and images were reconstructed[138]. Briefly, background subtracted raw images were bandpass filtered and local maxima above a threshold were used as starting locations for two-dimensional Gaussian fitting to unfiltered background subtracted images. The width and errors of the Gaussian fits as well as the sum of intensity in the fluorescent spot were used to cull outliers in each distribution of parameters. Stage drift was corrected for every 500 frames by finding the maximum in the 2D cross correlation produced by all localizations between successive groups of frames.

Localizations in the near-red channel were registered with the far-red channel using fiducial markers with adapted methodology[156]. Briefly, 100nm diameter Tetraspeck beads with fluorescence emission in both near and far-red channels (Invitrogen) were adhered to glass slides, excited by both 561nm (or 532nm) and 647nm lasers, and 70 fluorescent images of 20-40 beads were collected before and after the acquisition of each data set. These diffraction-limited fluorescent beads were used as control points to create a polynomial transform from the near-red channel to the far-red channel, and this polynomial transform was applied to mEos3.2 localizations in the near red channel.

Stage-drift corrected and emission channel registered point localizations were used to reconstruct a multicolor super-resolution image by incrementing pixels corresponding to 25nm for each localization falling into that pixel for each emission channel. $C(r,<\tau>)$ was determined from images, I_1 and I_2, reconstructed from point localizations collected from each emission channel over time as follows consistent with previous work[138].

$$C(r,<\tau>) = Re\left\{\frac{FFT^{-1}(FFT(I_1)\ x\ conj[FFT(I_2)])}{(\rho_1\rho_2 W(r))}\right\} \qquad \textit{Equation 12}$$

Here, *conj[]* indicates a complex conjugate, ρ_1 and ρ_2 are the average surface densities of images I_1 and I_2 respectively, and Re{} indicates the real part. $C(r,\tau)$ was determined using stage drift corrected and emission channel registered point localizations. Both $C(r, \tau)$ and $C(r, <\tau>)$ were computed from point localizations falling within a user-defined region of interest (ROI), and this ROI was used to determine normalization factor W(r).

Single molecule trajectories were determined using a tracking algorithm that searches for localizations within 500 nm in subsequent frames and terminates ambiguous trajectories[203]. The average mean squared displacement (MSD) as a function of time interval (τ) was tabulated for all trajectories and diffusion coefficients were extracted through a linear fit to the second through fourth time point of the MSD(τ), and error bounds reflect standard error determined directly from this fit to determine the average diffusion coefficient D. Single trajectory diffusion coefficients were obtained by tabulating MSDs from single long trajectories (greater than 10 segments), and fitting the second through fourth point of MSD vs. τ in the same manner to obtain individual diffusion coefficients D.

3.4.11: Strategies to reduce the effects of bleed-through

As demonstrated in **Figure 15, 16**, and **17** fluorescent bleed-through of one fluorophore into the other image channel leads to additional spatial correlations at short distances that are also correlated in time. While the most reliable method to reduce the adverse effects of bleed-through are to choose probe pairs that minimize this artifact, several analytical approaches can be used to correct for bleed-through under specific circumstances. For example, if dynamics are slow compared to both the acquisition time for single molecule detection and the characteristic on-time of fluophoroes, the it is possible to extrapolate $C(r, \tau)$ to $\tau=0$ while excluding the small τ points that are affected by bleed-through. An application of this can be seen in **Figure 15**, where $C(r, \tau =0)$ is systematically higher than $C(r, \tau \rightarrow 0)$ for the first spatial bin ($r<50$nm for Lyn and $r<100$nm for GG). For instances where co-localization dynamics are fast compared to acquisition time or fluorophore on-times, then it may be possible to estimate the magnitude of a bleed-through correction to $C(r, \tau=0)$ by first calibrating with a fixed cell sample, where the

effects of bleed-through can be directly measured (**Figure 17**). Under conditions where it can be assumed that bleed-through properties are not altered by fixation, then in principle this correction could be applied to live cell data. It should be noted that chemical fixation can alter the quantum yield of some fluorophores[204], so there is limited applicability of this method. Finally, it may be possible to correct for bleed through directly, by first measuring the magnitude of the bleed-through signal, then subtracting the predicted bleed-through signal directly from acquired data prior to image processing. In our hands, we found this method to be computationally expensive, since it requires that fluorophores be first localized, then a spatial transform computed to properly localize the bleed-through signal on the second image channel. We also found this method to be only moderately effective for reducing the magnitude of $C(r, \tau=0)$ in cases of known bleed-through, likely due to the uncertainty in intensity and localization inherent to this treatment.

Chapter 4: B cell receptor clusters anchor an ordered membrane domain that sorts proteins involved in signal initiation

The work presented in this chapter is a current collaboration between the following authors:

Matthew B Stone, Sarah L Veatch, Sarah A. Shelby, Marcos F. Núñez, Kathleen Wisser

Author contributions:

Study Design: MBS, SLV; *Data Collection:* MBS, SAS, MFN, KW; *Data analysis:* MBS, SAS, SLV; *Manuscript preparation:* MBS and SLV

The B cell antigen receptor (BCR) communicates binding of antigen in the extracellular environment through the B cell plasma membrane and is a central component of the adaptive immune system. It has been suggested that BCR clusters are surrounded by a distinct plasma membrane composition following antigen binding which may influence receptor phosphorylation, clustering, and internalization. Using multicolor super-resolution microscopy, we show that peptides bearing only membrane anchoring components display non-uniform spatial distributions around B cell receptors in a manner consistent with formation of an ordered membrane composition around BCR clusters. We find that the local production of charged lipids, including PIP2, alters the BCR-proximal spatial distribution of membrane proteins bearing polybasic sequences such as those in the Ras and Rho family of GTPases. We also find that membrane domains act to enrich BCR clusters in Lyn and deplete clusters of CD45, and we develop a minimal model in which this domain mediated sorting of signaling mediators leads to

receptor activation upon clustering that requires the presence of membrane domains. We also explore the role of cholesterol perturbation and find that cholesterol depletion enhances BCR stimulation by increasing the contrast of the domain. These results directly show that B cell receptor clusters stabilize a relatively ordered composition analogous to order-disorder fluid phase coexistence observed in model membranes and suggest a membrane order-based mechanism for signal initiation and regulation of multichain immune recognition receptors.

4.1: Introduction

It is postulated that the composition of the B cell plasma membrane is not uniform following clustering of the B cell receptor (BCR) by antigen, where that nascent BCR clusters form a domain with relatively ordered lipid acyl chains that is enriched in sphingomyelin and palmitoylated proteins and depleted of certain transmembrane proteins[67,83,198,205,206]. These ordered domains surrounding the receptor cluster, also referred to as 'lipid rafts', may serve important roles in the initiation of BCR signaling[83], the regulation of BCR sensitivity[207], the internalization of BCR clusters[206,208], and the processing and presentation of antigen[209] through the enrichment or depletion of regulatory proteins and lipids proximal to BCR clusters[205,210]. Analogous hypotheses exist for other multi-chain immune recognition receptors such as the T cell[69,211] and Fc[210,212] receptors. While this membrane-mediated regulation of receptor activity is appealing, it has proven difficult to validate experimentally due to a lack of direct experimental methods to probe small structures with low contrast in intact cell membranes[100,213–215]. Micron-scale domains rich in saturated lipids are routinely observed in phase separated model membranes[74,147], but the presence of a direct correlate in intact cell membranes remains controversial[213]. Chemical treatments either extracting or adding cholesterol are often used to invoke dependencies on lipid rafts, however, it is currently unclear what effect cholesterol modulation has on membrane domains, leading to great disagreement in the field about the role of membrane domains in cellular processes.

The main goal of the current study is to directly test the hypothesis that lipid domains exist in the plasma membrane of B cells by visualizing the nanoscale distribution of simple membrane anchored peptides around the B cell receptor using quantitative multicolor super-resolution

microscopy. These peptides are used as markers of ordered- and disordered-like domains, and we validate their partitioning into ordered- and disordered-domains in cells. We find that B cell receptor clusters anchor a domain that is enriched in liquid-ordered probes and depleted in liquid-disordered probes phase in the plasma membrane of B cells in both chemically fixed and live cells. These plasma membrane domains drive the segregation of CD45 away from receptor clusters and act to enrich Lyn, providing a plausible scheme for receptor phosphorylation initiation and control. A simple model based on the membrane as a super-critical fluid recapitulates the observed domain formation around receptor clusters and also indicates that domain stabilization around receptors could trigger robust activation. We further show that cholesterol modulation does not destroy membrane domains and can rather increase or decrease the contrast between domain and the rest of the plasma membrane, leading to predictable differences in receptor activation that are consistent with how cholesterol perturbations alter calcium responses to antigen. Our results show that, generally, protein clusters can anchor both disordered and ordered domains in the plasma membrane in agreement with their partitioning in model systems, and these domains sufficiently influence protein spatial distributions to significantly impact cellular behavior.

4.2: Results

4.2.1: Membrane-interacting peptides have non-uniform distributions around protein clusters

Here, the spatial distribution of membrane anchored probes report on the existence and nature of compositionally distinct domains present in the plasma membrane. We employ (direct) stochastic optical reconstruction microscopy, (d)STORM[118,119], and (fluorescence) photoactivation localization microscopy, (f)PALM[120,121], to simultaneously localize clustered membrane components and expressed membrane anchors in chemically fixed and live CH27 B cells. These point localization-based super-resolution imaging techniques provide a 10-fold increase in lateral resolution compared to conventional fluorescence microscopy[216,217] and have the sensitivity to detect subtle changes in the co-distribution of proteins labeled in the cell membrane when co-distributions are quantified using pair cross-correlation functions[139,162,200]. Membrane anchored peptides conjugated to the photoactivatable fluorescent probe mEos3.2 (**Figure 23**) are markers of ordered or disordered plasma membrane domains. PM is a

palmitoylated and myristolated peptide from the 11 N-terminal residues of Lyn that is used as a probe of ordered domains. In general, palmitoylated proteins are frequently enriched in Triton-X insoluble membrane fractions isolated from cellular membranes[66,67,86] and palmitoylation is necessary for the ordered phase localization of integral membrane proteins in phase separated vesicles derived from plasma membrane[135]. GG is a geranylgeranylated peptide containing a 6 lysine polybasic sequence modeled after the C-terminal anchoring of K-Ras4B and is used as a probe of disordered domains[108]. Geranylgeranyl groups are branched and unsaturated, and geranylgeranylated proteins are not found in detergent insoluble membrane fractions[66,86].

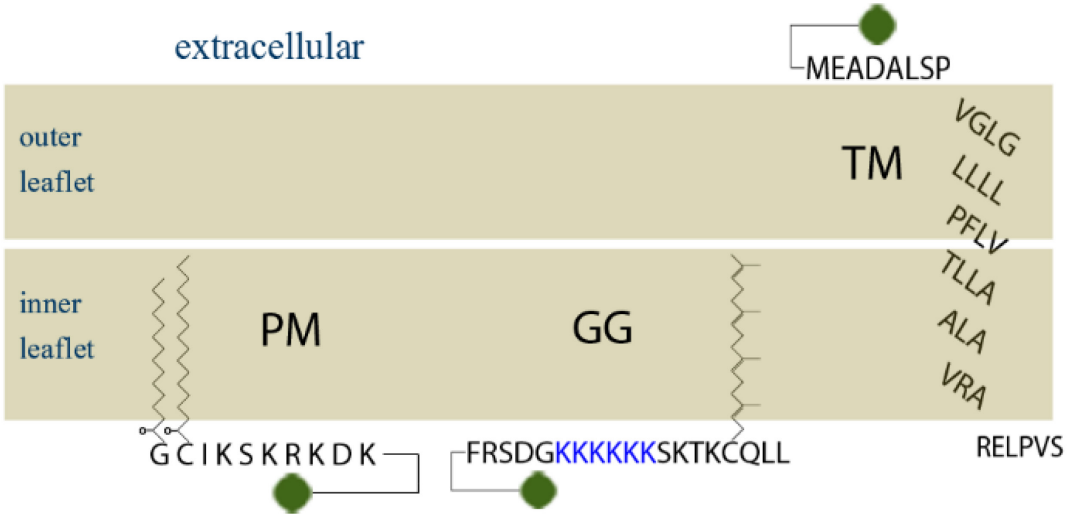

Figure 23: Membrane probes used in this study

The three probes used in this study are shown as simple models of how they interact with the membrane bilayer. PM, originally described in reference 108, contains the first 10 residues of Lyn kinase, which is sometimes referred to as its SH4 domain, which is naturally palmitoylated and mirisoylated on its N-terminus due to acylation signal sequences. A short amino acid linker connects PM to the mEos3.2 protein, shown in green. GG, originally described in reference 108, contains a geranylgeranyl group on its C-terminus along with a proximal polybasic region that assists in localizing GG to the plasma membrane, which is connected to mEos3.2 via a short amino acid linker. TM, described in [135], is the transmembrane domain of Lat, where the native palmitoyl cysteines have been mutated away.

We first demonstrate the utility of these peptide probes as markers of membrane domains by quantifying their localization with respect domains generated by clustering ordered or disordered membrane components in the plasma membranes of CH27 cells (**Figure 24**). We generated ordered domains on the outer leaflet of the plasma membrane by binding biotinylated cholera toxin subunit B (CTxB) to endogenous GM1 and then clustering membrane bound CTxB with

streptavidin. CTxB is a well characterized marker of ordered domains in both model and cell membranes[144,146]. We find that CTxB clusters contain a higher local concentration of PM than is present in the rest of the membrane, while the local concentration of GG in these clusters is reduced when compared to the average concentration of GG in the plasma membrane (**Figure 24a**). This can be seen in the cross-correlation curves shown, which quantify the average relative density of PM and GG as a function of distance from the center of CTxB clusters. These cross-correlation curves are normalized such that 1 represents the average density, a value of 0.8 indicates a concentration 20% less than than the average density, and a value of 1.2 indicates a concentration 20% higher than the average density. This result indicates that clustering CTxB on the outer leaflet results in an inhomogeneous distribution of PM and GG probes on the inner leaflet, consistent with the formation of an ordered membrane domain that is approximately as large as the CTxB cluster and spans both membrane leaflets. We generated a disordered domain in the plasma membrane by transiently expressing and clustering a peptide that favors a disordered composition. The peptide, referred to here as TM, is the 36 residue transmembrane helix from the LAT protein in which the palmitoylation sites have been removed. Past work demonstrates that TM strongly partitions into the disordered phase of giant plasma membrane vesicles (GPMVs)[135]. Clusters of TM were generated by binding an extracellular YFP tag to a biotinylated primary antibody followed by clustering with streptavidin. We find that TM clusters contain a higher local concentration of GG than is present in the rest of the membrane, while the local concentration of PM in these clusters is reduced when compared to the membrane as a whole (**Figure 24b**). This is the inverse of what was observed for CTxB domains, consistent with the formation of a disordered membrane domain.

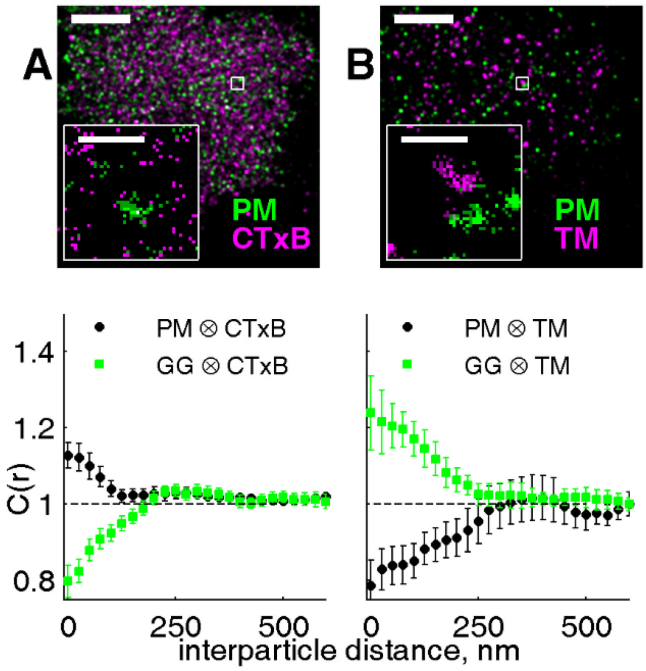

Figure 24: Clusters of ordered or disordered phase markers create compositionally distinct domains

(A) In the upper panel, a representative reconstructed super-resolution image of PM-mEos3.2 localizations (green) and clustered CTxB-Atto 655 in a fixed CH27 cell is shown. In A and B, the large image scalebar is 5 μm and the inset shows a zoom in of the boxed region where localizations are shown as iterations on a pixel grid in which the scalebar is 500 nm. In the lower panel, the average cross-correlation between CTxB and either PM (N=12) or GG (N=12) in fixed cells. Errorbars in A and B indicate the standard error of the mean. **(B)** In the upper panel, a representative reconstructed super-resolution image of PM-mEos3.2 localizations (green) and clustered TM-Atto 655 in a fixed CH27 cell is shown. In the lower panel, the average cross-correlation between TM and either PM (N=12) or GG (N=8) in fixed cells.

Together, these results demonstrate that the lateral distributions of PM and GG are influenced by the presence of protein clusters in the plasma membrane. PM is enriched in ordered CTxB clusters whereas it is depleted in disordered TM clusters, providing evidence that PM partitions more strongly into ordered membrane domains. In contrast, GG is depleted from CTxB clusters and enriched in TM clusters, consistent with it partitioning more strongly into disordered domains. This spatial heterogeneity is subtle as we only observe a 20% enrichment or depletion of the peptide probes within the clustered protein domains. We conclude that the observed heterogeneity is likely mediated by membrane composition since both PM and GG peptides lack protein binding motifs.

Membrane domains are also observed within B cell receptor clusters in chemically fixed and live CH27 cells and primary B cells (**Figure 25**). The PM peptide is enriched and the GG and TM peptides are depleted from clustered BCR in CH27 cells chemically fixed 5 minutes after antigen addition (**Figure 25a**). This finding is quantitatively similar to that observed for clustered CTxB in Fig 1a, suggesting that BCR and CTxB stabilize similar local membrane compositions in CH27 B cells. We also observe that BCR clusters are enriched in PM and depleted of TM in living CH27 cells (**Figure 25a**) when co-localization is quantified using a steady-state cross-correlation function[200]. This quantitative agreement indicates that the observations of non-uniform distributions of peptides in fixed cells are not a consequence of chemical fixation. In these live cell measurements, we also tracked the mobility of PM and GG probes and do not observe altered mobility for probes in close proximity to BCR clusters (**Figure 26**). This is counter to the diffusion behavior observed for full length Lyn kinase which slows near BCR clusters (reference 200 **and Figure 26**), likely due to direct interactions between Lyn and BCR or other proteins. BCR-proximal domains are also observed in primary mouse B cells chemically fixed 5 minutes after antigen addition (**Figure 25b**). In this case we observe quantitative differences between the partitioning of peptides within BCR clusters in primary vs. CH27 B cells, with increased recruitment or exclusion of all probes in primary cells. This likely due to some combination of their being inherent differences in the membranes of these two cell types and the requirement that primary cells be stimulated with LPS in order to maintain cell viability during the expression of transfected plasmids (see **Methods Section 4.4.3**). Taken together, these results indicate that clustered BCR stabilizes a local environment that is enriched an order favoring peptide and depleted of two disordered favoring peptides.

The cross-correlation curves shown in Fig 2A can be simply converted into the potential of mean force[162,200] (PMF) according to PMF = $-k_BT(c(r))$. This quantity provides a measure of the potential energy felt by the peptides as a function of the distance from the center of BCR clusters. **Figure 25c** shows the potential well for PM partitioning near the BCR and the potential barriers for TM and GG partitioning near the BCR from observed correlations in fixed CH27 cells. Interestingly, the length scale of the TM and PM domains are slightly larger than the BCR cluster itself, indicating that the membrane domain persists beyond the BCR cluster. The magnitude of these wells and barriers are several tenths of k_BT and span the footprint of the

receptor clusters, consistent with these interactions being weak but long range. Due to the finite lateral resolution of this measurement, these PMF curves provide a lower-bound estimate of the energy associated with these non-uniform distributions **Figure 27**. Additionally, we are not able to resolve depletion of GG or TM around unclustered B cell receptors, however, weak enrichment between PM and Lyn could be faintly resolved between unclustered BCR and Lyn or PM (**Figure 28**). The inability to resolve domains around unclustered BCR is likely due to finite resolution lowering the correlation magnitudes detailed in **Figure 27**.

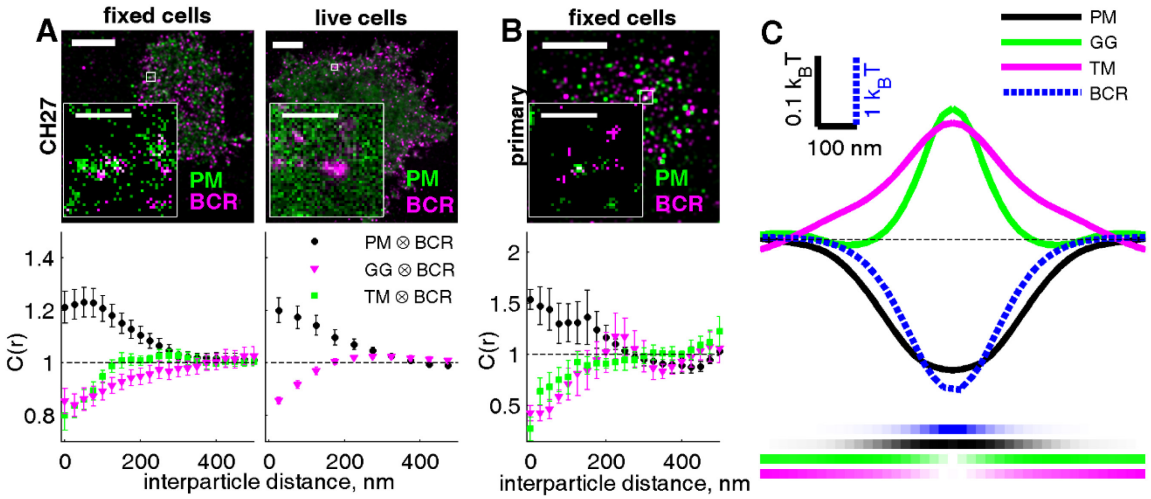

Figure 25: B cell receptor clusters anchor ordered membrane domains in the B cell plasma membrane

(A) In the upper panel, representative reconstructed super-resolution images of PM-mEos3.2 (green) and BCR-Atto 655 (magenta) localizations in fixed (left column) and live (right column) CH27 cells are shown. In A and B, the large image scalebar is 5 μm and the inset shows a zoom in of the boxed region where localizations are shown as iterations on a pixel grid in which the scalebar is 500 nm. The live cell image is reconstructed from 5 minutes of data following antigen addition. The lower left panel shows the average cross-correlation between BCR and either PM (N=8), TM (N=10), or GG (N=18) in cells fixed 5 minutes after antigen addition, and the lower right panel shows correlations between BCR and PM (N=4) or TM (N=4) in live cells following antigen addition. Errorbars in the lower panel of A and B indicate the standard error of the mean between correlations from separate cells. **(B)** In the upper panel, a representative reconstructed super-resolution image of PM-mEos3.2 localizations (green) and BCR-Atto 655 (magenta) in a live primary B cell fixed one minute following antigen addition is shown. In the lower panel, the average cross-correlation between BCR and either PM (N=4), TM (N=5), or GG (N=4) in primary cells fixed one minute following antigen addition. **(C)** Potential of mean force between the BCR and the membrane anchored peptides is shown after smoothing and making symmetrical about r=0. The black dotted line is where the PMF=0. The saturation of the gradient lines below the figure denotes the relative concentrations of each component in space with the same x-axis scaling as above.

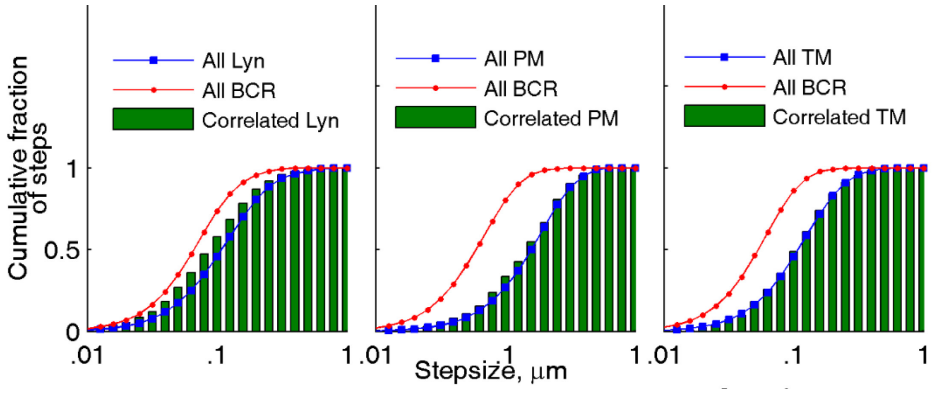

Figure 26: Step-size of lipid probes does not change when close to BCR clusters

BCR and either Lyn, PM, or TM were tracked simultaneously with TIRF excitation during a live cell, multicolor super-resolution experiment. BCR was labeled with a f(Ab)1 fragment conjugated to biotin and Atto 655, while Lyn, PM, and TM probes contained mEos3.2 tags and were transiently expressed using nucleofection. Live cells with BCR labeled with f(Ab)1 fragment were stimulated with 2 μg/mL streptavidin in order to cluster BCR and induce stimulation. The curves above show the stepsize distributions for BCR and probes PM, TM, and Lyn. Green bars show the stepsize distribution only for probes correlated with BCR, which were detected within 100 nm of a BCR localization in the same frame. Stepsizes for correlated probes were determined form the positions in the immediately preceeding and following frames. Lines show the stepsize distribution for all probes detected, and are used to compare the stepsize distribution of the correlated probes. Interestingly, correlated lipid probes show no change in diffusion from the rest of the membrane, indicating that diffusion of probes in membrane domains is not appreciably different than elsewhere in the membrane.

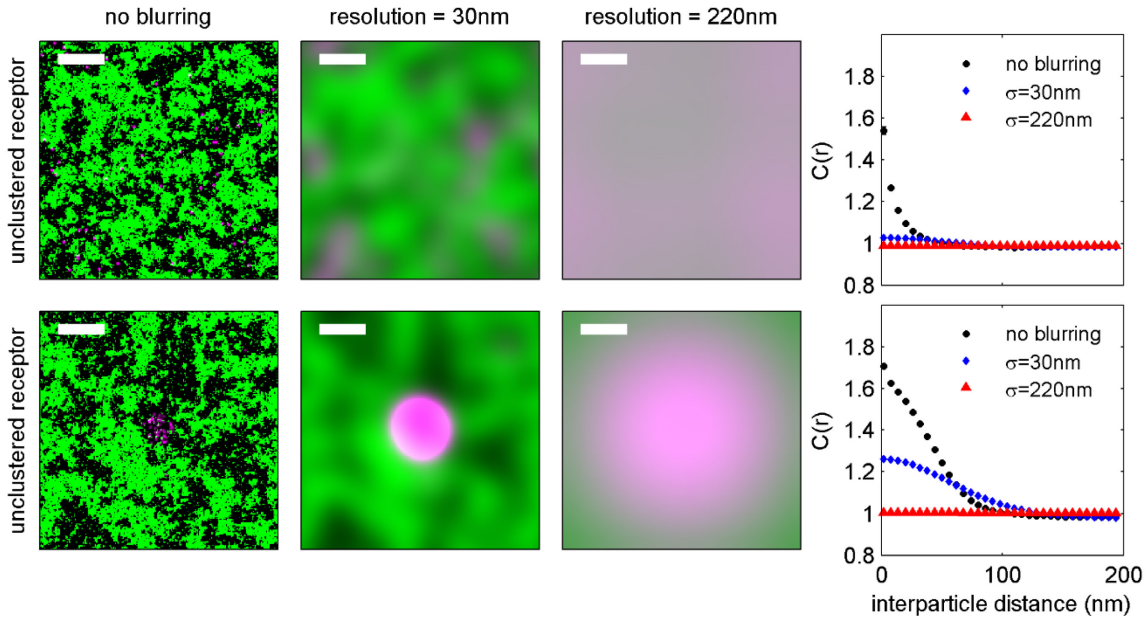

Figure 27: Resolution of super-resolution microscopy experiment limits the size of domains that can be investigated

We quantify here how finite experimental resolution impacts the cross-correlation signal between receptor and membrane probe for an example case of a domain formed in an Ising model simulation. Here, receptors are placed in an Ising model in either random (upper) or clustered distribution (lower), shown at left. Receptors are defined to always prefer the dark phase, and the model is placed above the phase transition temperature such that there are still visible fluctuations in composition but not phase separation. 2 dimensional cross-correlations were then convolved with a Gaussian with a width of the resolution from super-resolution experiment ~30 nm (middle) or resolution of conventional microscopes ~220 nm. We find that the small fluctuations in composition that are in the simulation from unclustered receptors are not resolvable by traditional or super-resolution microscopy (right, blue line) since convolution with the experimental resolution reduces the magnitude of observed cross-correlations close to the noise floor. In contrast, clustered receptors anchor a domain that is observable by super-resolution microscopy, although still not resolvable by traditional microscopy.

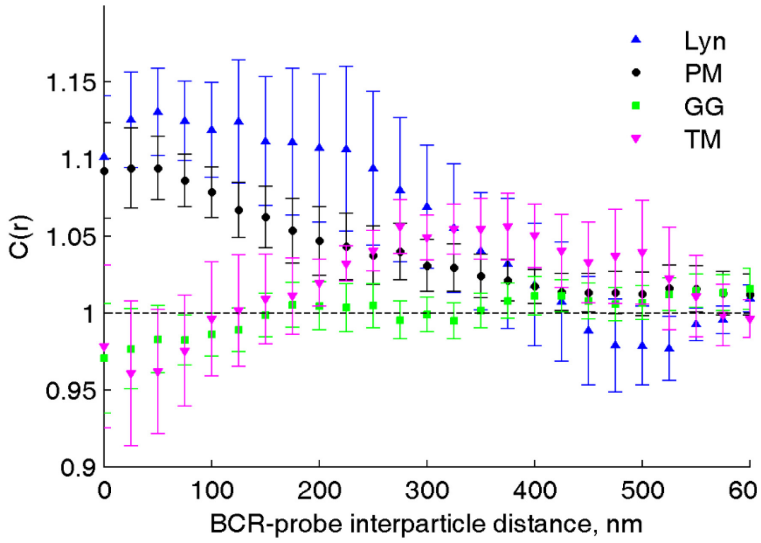

Figure 28: Correlations between membrane anchors and unclustered BCR are difficult to resolve

Correlations between membrane probes investigated in this study and unclustered BCR are shown. For PM and Lyn, weak enrichment around unclustered BCR is resolvable, however, this may be due to a few clustered BCR in the resting state rather than the correlation between single receptor and membrane anchor. Disordered favoring probes GG and TM are uniform within error, although the overall shape of the curves may suggest anticorrelation.

4.2.2: Both domains and charged lipids affect GG distribution

We observe quantitative differences between of GG and TM partitioning behavior, even though both peptides exhibit the same qualitative behavior of being depleted from BCR clusters. GG depletion from BCR clusters is of shorter range than TM after 5 min of antigen stimulation (**Figure 25**), and GG correlations are significantly reduced in magnitude compared to TM correlations after 1 min of antigen stimulation (**Figure 29a**). We hypothesize that these differences arise due to the poly basic stretch present on GG which likely interacts with anionic lipid produced within active BCR clusters, particularly the anionic lipids PIP_2 and PIP_3 which are known to play important roles in BCR signaling[218,219]. These anionic lipids may recruit the GG peptide to BCR clusters, countering the partitioning preference of the acyl modification. In support of this hypothesis, we observe enrichment of the PIP_2 binding PH motif of PLCδ2 within BCR clusters at 1 minute but not 5 minutes following antigen stimulation (**Figure 29b**).

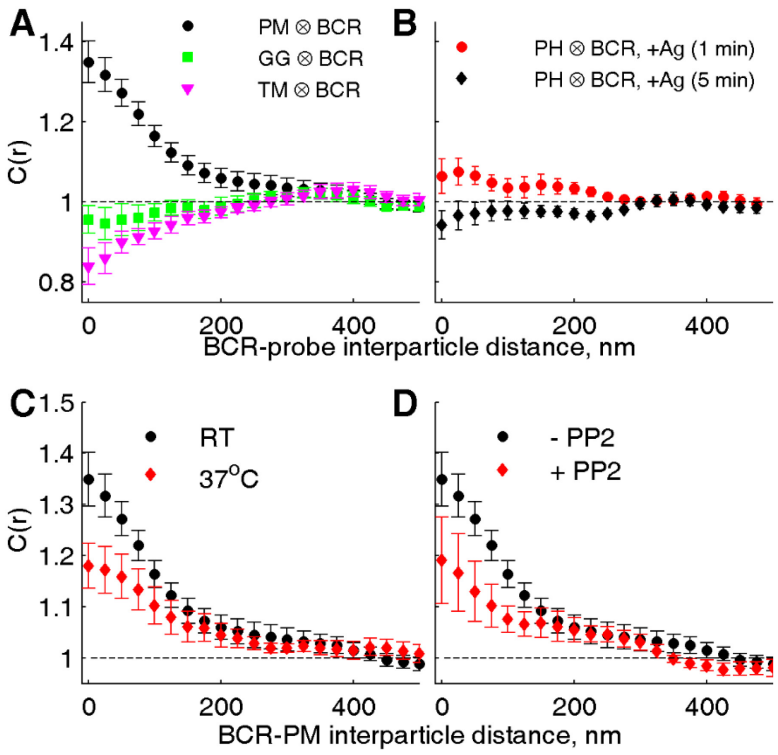

Figure 29: GG is sensitive to both domain formation and the presence of charged lipids; domains are sensitive to ambient temperature and BCR phosphorylation

(A) Cross-correlation functions between BCR clusters and lipid anchor probes in cells fixed one minute following antigen addition. Errorbars represent standard error of the mean (PM: N=13, GG: N=8, TM: N=11). **(B)** Average cross-correlation between BCR and PH motif in CH27 cells fixed 1 minute (N=7) and 5 minutes (N=10) after antigen addition. Errorbars indicate standard error of the mean. **(C)** Average cross-correlation between PM and BCR at room temperature (black) or at 37°C (red) one minute following antigen addition (N_{RT}=13, N_{37}=11). Errorbars indicate standard error of the mean. **(D)** Average cross-correlation between PM and BCR in cells treated with 40 μM of the Src kinase inhibitor PP2 (red) or control (black) and fixed one minute following antigen addition (N_{-PP2}=13, N_{+PP2}=7).

The magnitude of PM partitioning within BCR clusters depends on both temperature and receptor phosphorylation. Results of **Figure 25** were accomplished at room temperature, where CH27 cells exhibit antigen dependent signaling responses[200] but is below physiological temperature. Thus, we examined the partitioning of PM within BCR clusters in cells chemically fixed at 37°C and find that PM recruitment is reduced in magnitude but still detectable (**Figure 29c**). This suggests that BCR clusters stabilize an ordered membrane domain at physiological temperatures. We also investigated if PM partitioning depends on BCR activation using PP2 to inhibit Src family kinase activity[220]. Src kinase inhibition acts to decouple the clustering of BCR

from Syk phosphorylation[221], thus preventing adaptor protein binding and downstream signaling. PM partitioning is reduced under conditions where receptor phosphorylation is suppressed (**Figure 29d**). This suggests that the B cell receptor does not solely anchor the ordered domain within these clusters, but also productive interactions with down-stream components amplify this effect. We note that BCR clusters are also smaller under PP2 treatment (**Figure 30**), and this reduction in cluster size is also expected to reduce the magnitude of cross-correlation functions due to the limited lateral resolution of these measurements (**Figure 27**).

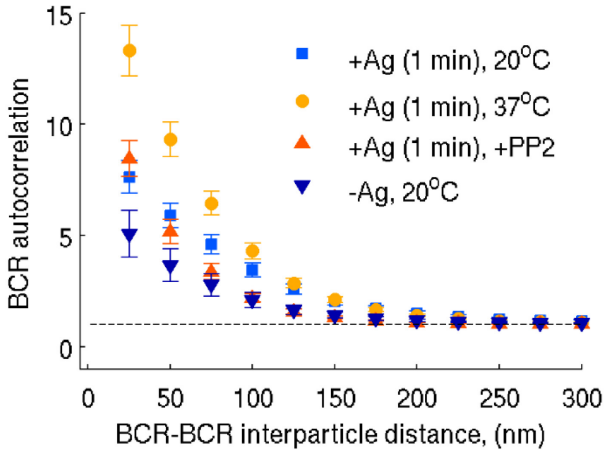

Figure 30: BCR clustering differences are observed for PP2 and temperature treatments

We compute autocorrelations for BCR images and average over all cells in our data sets. Here, we have removed the first point of the autocorrelation since this point is mostly determined by the degree of overcounting in the super-resolution images, and is thus not useful for determining clustering. The autocorrelations were well fit by exponential decays, and the decay constant from the fit is plotted below the curves. The decay constant indicates that B cells stimulated at both higher temperature and in the presence of PP2 have a slightly smaller BCR cluster size.

We also estimate the numbers of B cell receptors in the cluster, since a very high BCR receptor density in a cluster might lead to a loss of membrane fluidity around individual receptors. We utilize the autocorrelation of the receptor cluster along with knowledge of the average receptor density to estimate how many BCR are enriched in the cluster. We radially integrate the exponential fit to the autocorrelation curve between 0 and 200 nanometers, and multiply this by the average density of BCR to give the number of BCR in a cluster. We find that there are

between 90 and 450 BCR in a cluster with radius 200 nm assuming that the average density of the BCR is between 200 μm^{-2} and 1000 μm^{-2}. The average density of BCR can be estimated from previous work[194,195] to be 500 μm^{-2}, which gives a value of 220 BCR in a cluster of radius 200 nm. Importantly, the number of BCR in this cluster is only at max about 5% of the total membrane fraction in the cluster, since assuming that the average lipid or transmembrane protein takes up about 1 nm^2 gives around 10,000 membrane proteins or lipids in a circular area with a 200 nm radius. This indicates that there is an appreciable amount of free membrane that is not being determined by the annular space around BCR proteins.

4.2.3: Domains enrich Lyn and deplete CD45

We have also investigated the localization of Lyn kinase and CD45 along with their minimal membrane anchor sequences in chemically fixed cells (**Figure 31**), both proteins known to play important roles in receptor activation and regulation. Lyn phosphorylates ITAM residues on BCR and we find that Lyn kinase is strongly recruited to BCR clusters at both 1 and 5 minutes after antigen addition (**Figure 31a**). This is consistent with the direct binding of Lyn to phosphorylated ITAM sequences associated with the BCR. PM, the minimal anchor sequence of Lyn, is also recruited to BCR clusters, although the magnitude of this enrichment is weaker than the full length protein. When this is examined as a potential of mean force, full length Lyn has a potential well that is roughly 3 times deeper than that of PM (**Figure 32**). This suggests that the PM anchor of Lyn provides roughly one third of the free energy of Lyn-BCR association after BCR cluster formation and signal initiation.

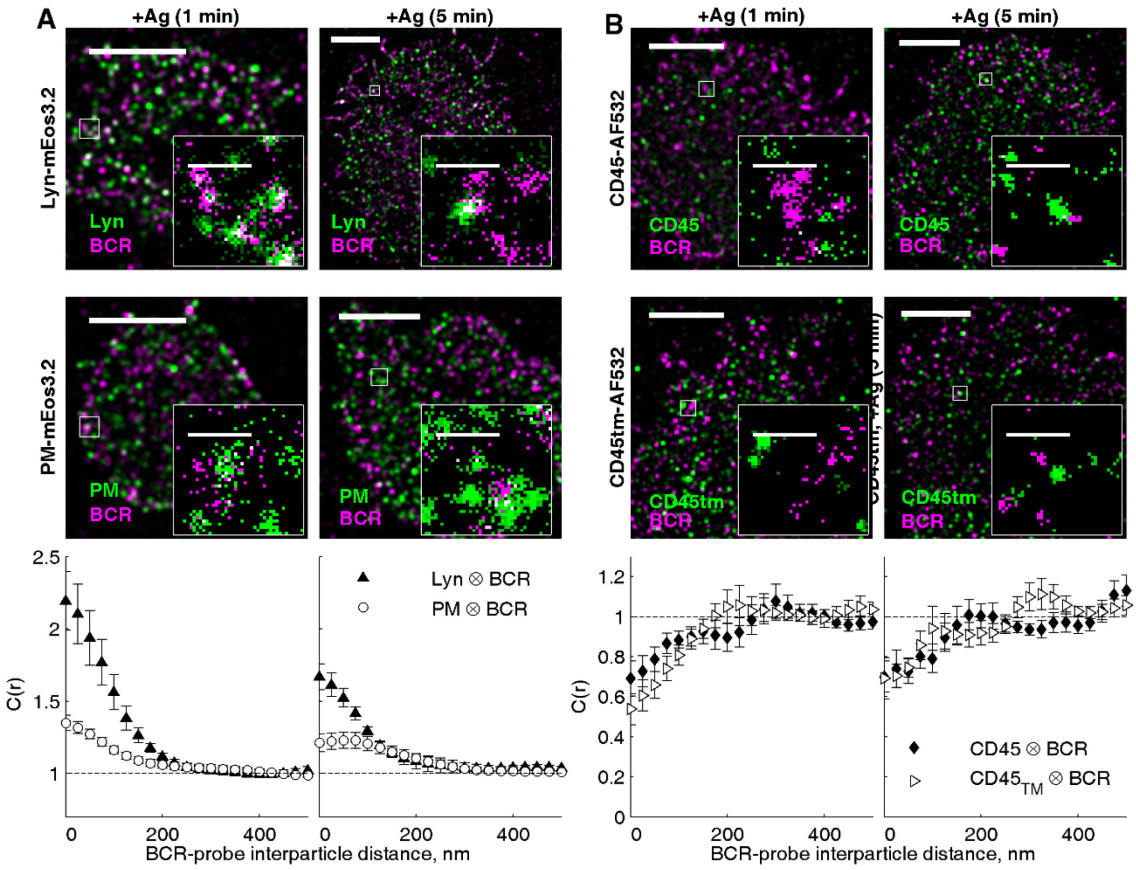

Figure 31: Membrane domains contribute to the enrichment of Lyn and the depletion of CD45 immediately following antigen stimulation

(A) (top and middle) Reconstructed two-color super-resolution images of Atto 655 labeled BCR shown in magenta and mEos3.2 labeled Lyn (top) or PM (middle) shown in green. BCR was clustered for 1 minute in cells on left and 5 minutes in cells on right. The insets in A and B show a zoom in of the boxed region, wherein localizations are shown as pixel iterations. Scale bars are 5 μm and 500 nm in both A and B. (bottom) Average cross-correlations between BCR and Lyn (cyan) or BCR and PM (magenta) for cells fixed 1 minute following antigen addition (left, N_{Lyn}=5, N_{PM}=13), and 5 minutes following antigen addition (right, N_{Lyn} = 4, N_{PM}=8). Errorbars indicate standard error of the mean in both A and B. **(B)** (top and middle) Reconstructed two-color super-resolution images of Atto 655 labeled BCR shown in magenta and Alexa 532 labeled CD45 (top) or CD45 transmembrane region (CD45tm, middle) shown in green. BCR was clustered for 1 minute in cells on left and 5 minutes in cells on right. (bottom) Average cross-correlations between BCR and CD45 (magenta) or BCR and CD45tm (green) for cells fixed 1 minute following antigen addition (left, N_{CD45}=13, N_{CD45tm}=15), and 5 minutes following antigen addition (right, N_{CD45} = 10, N_{CD45tm}=10.

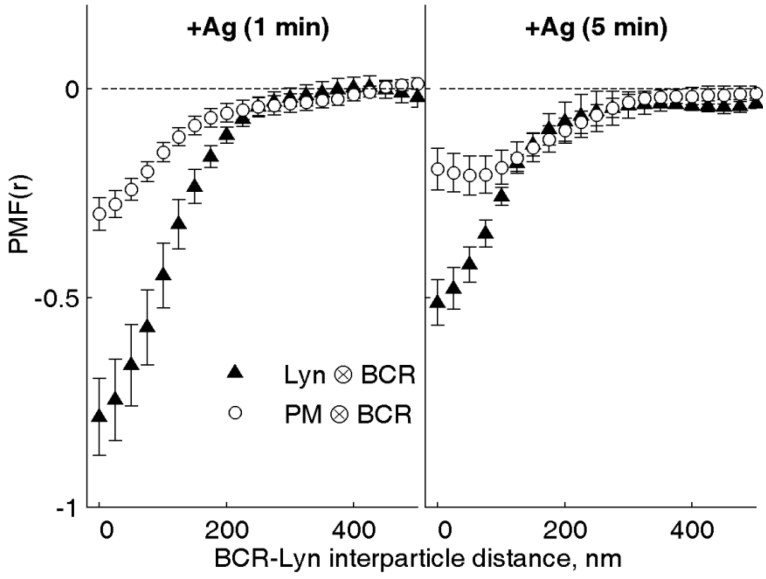

Figure 32: Lyn interaction with BCR is partially driven by membrane anchoring

Cross-correlations between BCR and Lyn or PM are converted to potential of mean force (PMF) by taking the –log(C(r)). This gives a lower bound estimate for the total energy of interaction between the BCR and Lyn (shown as triangles) or between the BCR and PM (shown as circles). We estimate that PM contributes around 1/3 of the total energy for the interaction between BCR and Lyn since the PMF between BCR and PM is 1/3 the magnitude of the PMF between BCR and Lyn for both 1 minute after stimulation (left) and 5 minutes after stimulation (right).

CD45 is a transmembrane phosphatase which deactivates the receptor and activating kinases, and whose localization is implicated in regulating receptor activity in a variety of contexts[47–49,222,223]. We find that both CD45 and its minimal plasma membrane anchor (CD45tm) are depleted from receptor clusters 1 and 5 minutes after antigen stimulation (**Figure 31b**). In this case, the magnitude of the depletion is the same within experimental errors for the full length protein and minimal peptide anchor. This indicates that the partitioning behavior of the membrane anchor sequence alone is responsible for segregating CD45 away from BCR clusters in these measurements. Taken together, these findings suggest that membrane anchor sequences contribute to the localization of signaling proteins proximal to BCR after cross-linking with multivalent antigen.

4.2.4: Domain formation can initiate BCR signaling

We hypothesize that domain formation around BCR clusters could initiate receptor phosphorylation. **Figure 33** simulates domain formation with an Ising model which naturally recapitulates our experimental observations of domain magnitude and extent. This minimal model includes receptors that prefer an ordered local lipid environment, components that activate receptors (e.g kinases) that also prefer an ordered environment, and components that deactivate receptors (e.g. phosphatases) that prefer a disordered environment, all embedded in a membrane containing fluctuating regions of ordered and disordered compositions (**Figure 33a**). Within this model, a receptor has a low probability of becoming activated when it is adjacent to an activating component and a high probability of becoming inactive when it is adjacent to a deactivating component. Through this set of minimal assumptions, it is possible to increase the fraction of activated receptors simply by clustering receptors (**Figure 33b**). Qualitatively, this occurs because receptor clustering stabilizes an ordered domain that is depleted of the phosphatase and enriched in the kinase (**Figure 33a**). Cross-correlations show that non-uniform distributions between the receptor cluster and the kinase or phosphatase are dependent upon fluctuations. Interestingly, these correlations have a similar magnitude as ones observed in B cells (**Figure 33c**).

While activation is increased upon clustering in this simple model by several fold, it does not lead to the dramatic change in receptor activation state typically associated with trigging an immune response. This is because there is a reasonable probability for a single deactivating component to enter the receptor cluster in this model, since the energy cost of placing a single disorder-favoring pixel in an ordered local environment is small compared to the thermal energy. Motivated by the observation that doubly tyrosine phosphorylated ITAM sequences on BCRs recruit the kinase Syk from the cytoplasm, we add an additional layer of complexity to the model, granting a receptor the ability to activate an adjacent receptor once the initial receptor becomes multiply activated. This additional layer of complexity acts to amplify receptor activation for cases where the local density of receptors is high and there are many collisions between components, as shown for a cluster of receptors in **Figure 33d**. Receptors still become inactivated when phosphatases diffuse through receptor clusters, leading to large fluctuations in

receptor phosphorylation state with time (**Figure 33e**). Within this model, significant receptor activation is not achieved in the absence of composition fluctuations, however the presence of composition fluctuations and receptor clustering induce strong phosphorylation that appears to fluctuate in time, as shown in **Figure 33e**.

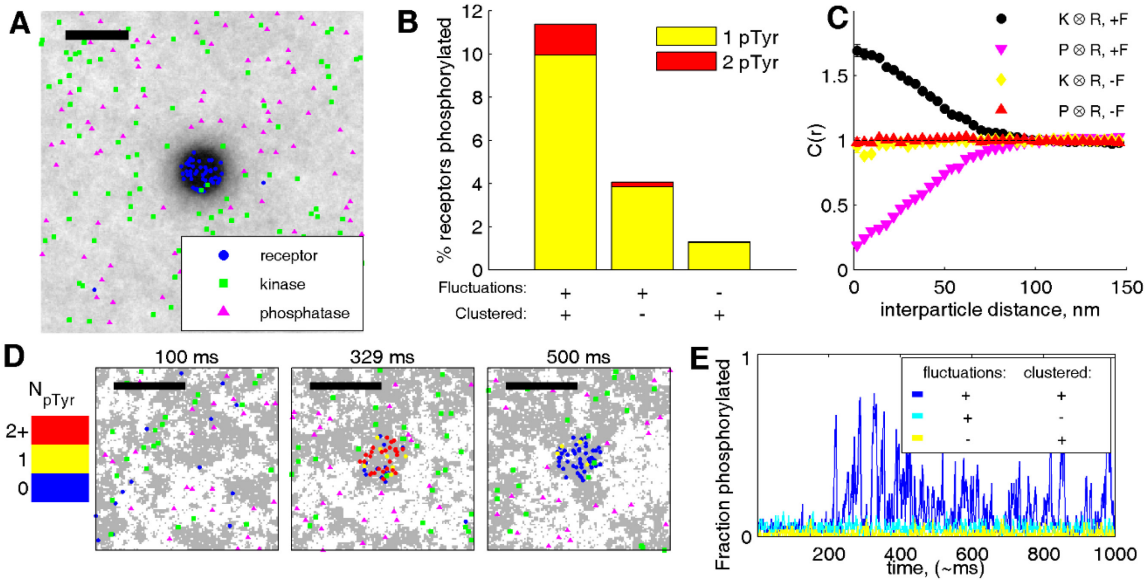

Figure 33: Initial activation of receptors clusters can be recapitulated by a simple fluctuation-based simulation

(A) Time-average Ising model where ordered spins are black and disordered spins are white. Receptor, kinase, and phosphatase positions from a single simulation frame are shown. Scalebar is 100 nm. **(B)** The percent of total receptors with either 1 (yellow) or more (red) activations are shown for clustered and unclustered receptors both with and without fluctuations. For simulations without fluctuations, only ordered spins were present, and thus the lattice was uniform. **(C)** Cross-correlations between receptors and kinase or phosphatase with and without fluctuations. **(D)** Time trace and frames from simulations where receptors can become kinases after being phosphorylated. The first frame shows the simulation prior to clustering, where receptors are randomly distributed around the lattice. The middle and right frames show when receptor clusters become either fully activated or deactivated, respectively. Scalebar is 100 nm. Far right time trace shows the percent of activated receptors for each condition, clustered, unclustered, or clustered without fluctuations. Time trace and frames correspond to the same simulation.

4.2.5: Cholesterol concentration modulates BCR responses

Historically, cholesterol depletion is thought to destroy lipid domains or lipid rafts, and signal loss upon cholesterol depletion was interpreted as a dependence of that biological process on lipid domains. However, cholesterol addition and depletion should rather change the relative amount of ordered and disordered phase as observed in model systems[75,224], which does not

prevent domain formation. We verify this in vesicles derived from B cell plasma membranes treated with either cholesterol or MBCD (**Figure 35a**). Depleting cholesterol and thus lowering the fraction of ordered membrane acts to increase the contrast between domains and the rest of the membrane since there is relatively little ordered membrane anywhere besides the domain. This is highlighted in the Ising model after replacement of 20% of ordered phase with disordered phase, where both the ordered lipid and kinase have a noticeably stronger relative enrichment and phosphatase has greater depletion in the domain. Conversely, addition of ordered lipids decreases the contrast between domains and the rest of the membrane (**Figure 35b**). The resulting effect on receptor activation in the simulation is striking; depleting the amount of ordered lipid acts to increase receptor phosphorylation, since kinases are further enriched and phosphatases are further depleted from the domain. Interestingly, ordered fraction depletion increases receptor activation up to a point until there is not enough ordered membrane to form a domain. Conversely, when the amount of ordered phase is increased, domains have less contrast and receptors are less phosphorylated (**Figure 35c**). We treat CH27 cells with either MBCD or cholesterol to change the fractional amount of ordered and disordered phase as demonstrated in **Figure 35a**. We and others[92,225] find that calcium response after receptor crosslinking is decreased upon cholesterol addition, and calcium responses are increased upon cholesterol addition until a significant fraction of cholesterol is removed as shown in **Figure 35c**. Shown here are the integrated area under peak calcium response, and raw curves are provided in **Figure 34.**

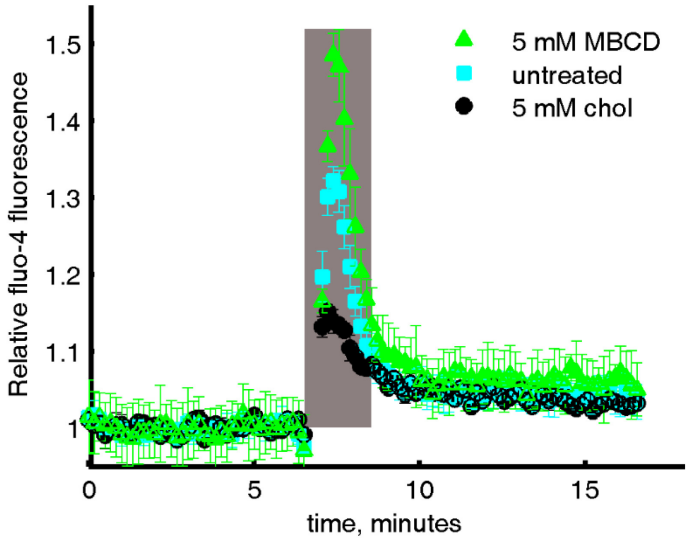

Figure 34: Fluor-4 fluorescence traces showing calcium response to antigen with MBCD and cholesterol treatments

Cells were pretreated with cholesterol loaded MBCD or MBCD for 15 minutes at 37 degrees before assaying cytoplasmic calcium release in a calcium free buffer at 37°C. Shown are the raw traces after baseline normalization for 5 mM MBCD, untreated, and 5 mM MBCD treated cells. Curves were integrated for the area within the grey box to give the total peak calcium response given in **Figure 33** in the main text.

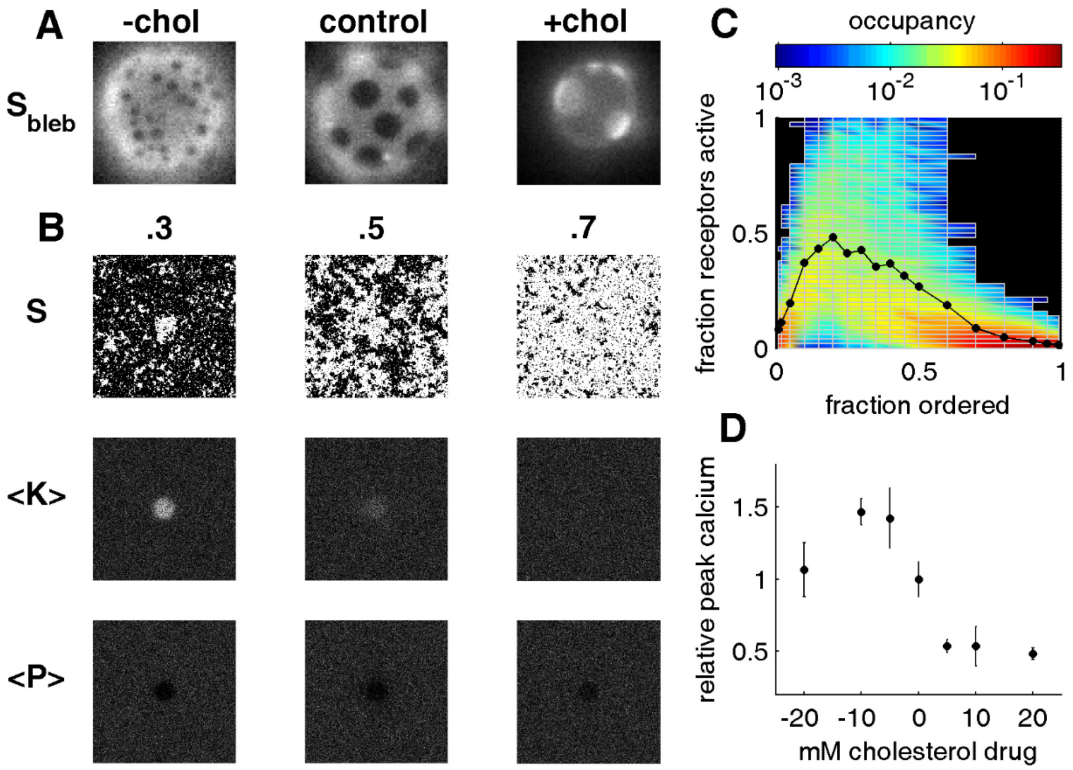

Figure 35: The fraction of ordered membrane determines the domain contrast and the signaling response to BCR clustering

(A) Effects of ordered fraction modulation seen in vesicles and Ising simulations. Giant plasma membrane vesicles (blebs) derived from CH27 B cells were treated with 5 mM MBCD (left), untreated (center), or treated with 5 mM cholesterol (right) for 15 minutes at room temperature. Here, DiIC12 is labeling the vesicles, which partitions strongly into the disordered phase, thus the ordered domains are dark. **(B)** Ising models of receptor clustering were performed with various fractions of ordered and disordered pixels, either with 30% (left), 50% (middle), or 70% (right) ordered pixels. The top row shows a single frame from the simulation where white pixels are ordered and black pixels are disordered. The second row shows the average position of kinase (<K>), and the bottom row shows the average position of the phosphatase (<P>). **(C)** The amount of receptor phosphorylation is shown for various levels of total ordered or disordered pixels in the simulation, where 0.5 gives an equal fraction of ordered and disordered phase. The coloring shows the distribution of receptor activation states through all 1000 frames collected through the simulation. The black line shows the average activation state for all 1000 frames. **(D)** Peak calcium response for CH27 cells treated with a varying amount of cholesterol or MBCD. Here, MBCD treatment is given as negative numbers and cholesterol treatment is given as positive numbers.

4.3: Discussion

In this study, we demonstrate that B cell plasma membranes can support domains that share some characteristics of liquid-ordered and liquid-disordered phases in purified and isolated biological membranes[74,224]. We further show that clustered B cell receptors reside within an ordered domain that sorts the membrane interacting motifs of key mediators of early BCR signaling. These measurements are made possible by multicolor super-resolution fluorescence localization microscopy, which has the lateral resolution to resolve domains and the sensitivity to detect the weak enrichment and depletion. Finally, we apply our experimental findings to construct a simple but plausible model of early BCR signaling where receptor clustering stabilizes compositionally distinct domain, leading to activation of receptors by altering the spatial distribution of regulatory components.

We observe a weak enrichment or depletion of membrane components within membrane domains. This is in contrast to the more conventional expectation that lipid domains strongly concentrate membrane components and confine diffusion. The cross-correlation curves of **Figure 25** indicate that there is roughly 20% enrichment or reduction of phase sensitive probes within BCR clusters compared to the membrane as a whole. In practical terms, this means that the average BCR cluster will contain only 1.2 PM probes due to lipid mediated interaction if a random distribution would yield 1 PM probe per cluster. It is not surprising that this subtle heterogeneity has not been consistently observed in past studies. Although this effect is weak, its magnitude can be large enough to produce significant effects, as demonstrated in our simulation studies of receptor clustering shown in **Figure 33 and Figure 35**.

Although this effect is weak, its magnitude is consistent with predictions of the critical fluctuation hypothesis in which heterogeneity arises because the plasma membrane is tuned to be slightly above a miscibility critical point[74,77,78,150]. In this model, clustering one type of membrane component, in this case the receptor, acts to stabilize a region of heterogeneous composition because the near-critical membrane has a high compositional susceptibility. While this domain persists in time, the depletion of probes is not absolute because the energy cost to incorporating some unfavorable components is close to the thermal energy. The enrichment of probes occurs

at even lower efficiency since the membrane contains many sites of favorable local interactions that are away from the receptor cluster. The observed magnitude of probe enrichment and depletion is consistent with past observations in model membranes, which find a similar level of fluorescent probe enrichment or depletion when phase partitioning components are clustered via adhesion purified model membranes and isolated plasma membranes investigated above their miscibility critical temperature[78].

Our current work supports and adds to the previously proposed view that B cell receptor clusters reside in an ordered membrane environment which positions the receptor in close proximity to Lyn[226]. Original work largely drew on indirect measures of plasma membrane organization, such as biochemical membrane fractionation in the presence of detergents and the modulation of receptor signaling by varying cholesterol content or temperature. More direct support for this view comes from two studies which observed FRET between the order preferring PM probe and the BCR soon after antigen crosslinking[109,227], and another study which observes co-localization between the order preferring CTxB probe and the macroscopic BCR clusters that form at long times (>30min) after antigen cross-linking[104]. Based on our current findings, we would update this scheme to state that receptor clustering acts to stabilize and extend existing ordered domains, biasing this biochemical network to favor receptor activation. This could be accomplished by favoring interactions with activating components such as Lyn and suppressing interactions with down-regulating components such as CD45 as illustrated in the results presented in **Figure 33 and Figure 35**. It is also possible that the stabilization of an extended membrane domain could impact how the receptor itself interacts with the membrane, influencing the conformation of intrinsically disordered ITAM regions of CD79a and CD79b[56,58].

Past work has demonstrated that the CD45 phosphatase can be sequestered from receptors when antigen is presented in a solid support due to steric exclusion. In this case, there is evidence that CD45 is excluded from regions of antigen bound receptor due to the high energy cost required to bend the membrane to accommodate its bulky glycosylated ectodomain. In the case of surface presented antigen we expect that this bending effect would likely dominate over the lipid mediated effects examined in our current study using soluble antigen, as membrane bending energies tend to be $>>k_BT$, much larger than the potentials measured in this study and shown in

Figure 25. Even so, it is possible that lipid-mediated interactions work in concert with these bending interactions make this stimulation mechanism more robust, by providing a mechanism to recruit or exclude other signaling components to sites of receptor activation. It is likely that both forced exclusion of CD45 and the intracellular recruitment of signaling mediators after receptor activation acts to extend and amplify this domain, since the enforced patterning of proteins coupled to ordered or disordered composition would also stabilize domains in the same fashion as the receptor cluster. This concept is supported by our observation of weaker recruitment of PM to cross-linked BCR in the presence of the signaling inhibitor PP2. It is also possible that further changes in this membrane environment impact how signals transmit downstream of receptor activation. This could in principle occur through the recruitment of co-receptors, the presence of actin flows, or due to other cellular or environmental cues. Further studies are needed to investigate these possibilities. This also could provide a means for cells to distinguish soluble and surface presented antigen, possibly leading to distinct signaling patterns that can impact the cellular antigen response.

While the experiments conducted here relate directly to membrane domains formed during BCR clustering, our findings suggest a novel mechanism underlying the emergence of membrane domains in cell plasma membranes, where proximity to a miscibility critical point allows perturbations such as protein clustering to be translated into significant compositional heterogeneity. Since the partitioning of membrane proteins affects their likelihood of coming into contact with other membrane bound proteins, domain stabilization can thus influence how often proteins interact and modify one another. Thus membrane heterogeneity could be tuned through the regulation of membrane composition in order to further regulate membrane bound biochemical networks. Some examples might be growth factor signaling, where we have recently shown a correlation between miscibility transition temperature and conditions that affect growth rates in RBL-2H3 mast cells[148] where the downstream regulators Ras and Rac have clear phase partitioning preferences[228]. Another example could be some GPCR signaling networks, where membrane heterogeneity could impact the accessibility of receptor to G protein or allosterically regulate GPCR internal states. Further work is needed to explore if similar organizing principles apply to these diverse signaling systems, and how the cell may regulate its membrane heterogeneity.

4.4: Methods

4.4.1: f(Ab)$_1$ modification and DNA constructs

f(Ab)$_1$ fragment goat antibody to mouse IgM, μ chain specific (Jackson Immuno Research, West Grove, PA) was simultaneously chemically modified with Atto 655 NHS ester (Sigma, St. Louis, MO) and biotin-X, SSE, 6-((Biotinoyl)Amino)Hexanoic Acid, Sulfosuccinimidyl Ester, Sodium Salt (Sulfo-NHS-LC-Biotin) (Invitrogen, Grand Island, NY). Modifications were carried out in aqueous solution buffered by 0.01 M NaH_2PO_4 with 0.01 M NaH_2CO_3, pH 8.2 for thirty minutes at room temperature. Reaction products were separated by gel filtration on Illustra NAP-5 columns (GE Healthcare, Piscataway, New Jersey) to remove unbound dye from labeled protein. Streptavidin and CTxB was biotylated and conjugated to ATTO 655 in-house via similar methods, and CTxB and f(Ab)$_1$ conjugation is also described in reference 200.

4.4.2: DNA constructs

Lyn, PM, and GG lipidation sequences[108] were a generous gift from Dr. Barbra Baird (Cornell University, Ithaca, NY) and were cloned using standard techniques to replace YFP with mEos3.2. Plasmid DNA encoding mEos3.2 protein and TM anchor sequence are gifts from the Dr. Akira Ono (University of Michigan, Ann Arbor, MI). All plasmids used here, SNAP and mEos3.2 tagged, are in Clontech N1 vector (Clontech, Mountain View, CA). We also cloned the CD45 transmembrane domain with a small number of flanking amino acids *de novo* from the amino acid sequence for mouse CD45 isoform 1, UniParc identifier P06800-1. We additionally included the HA membrane targeting signal sequence and a FLAG tag[229] upstream of the construct on the N terminus, to allow for efficient plasma membrane delivery and detection, respectively. We used 3 primers to amplify the CD45tm insert using PCR with Phusion DNA polymerase (New England Biolabs, Ipswich, MA), double digested both the insert and the Clontech N1 vector (Clontech, Mountain View, CA) using BamHI and EcoRI (New England Biolabs), dephosphorylated the digested N1 vector using Antarctic Phosphatase (New England Biolabs), and ligated the digested insert to the digested and dephosphorylated N1 vector for 18 hours at 16^{o} C with T4 DNA Ligase (New England Biolabs). This ligated product was transformed this XL1 Blue supercompetent cells (Agilent, Santa Clara, CA) in the presence of 50

μg/mL kanamycin (Fisher Bioreagents, Hampton, NH). DNA was sequenced (University of Michigan DNA Sequencing Core, Ann Arbor, MI) to confirm the presence of the insert and ensure correct sequence of the plasmid.

Amino Acid sequence of CD45tm insert with upstream HA-FLAG tag:
N terminus-
MKTIIALSYIFCLVFADYKDDDDANESTNFNAKALIIFLVFLIIVTSIALLVVLYKIYDLRK
KR-C terminus

Primers used for cloning CD45tm:
Primer1: 5'- ATGCGGAATTCATGAAGACGATCATCGCCCT-3'
Primer2: 5'- ACTGGATCCGCGCGTTTTTTGCGCAGATCATAAAT-3'
Primer3: 5'-
ATGAAGACGATCATCGCCCTGAGCTACATCTTCTGCCTGGTGTTCGCCGACTACAAG
GACGATGAT
GACGCCAACGAAAGCACCAACTTTAACGCGAAAGCGCTGATTATTTTCTGGTGTTT
CTGATTATTGTGACCAGCATTGCGCTGCTGGTGGTGCTGTATAAAATTTATGATCTGC
GCAAAAAACGC-3'

4.4.3: Cells and transfection

CH27 cells were maintained in low glucose DMEM (Invitrogen) containing 15% FBS (Mediatech, Manassas, VA), 10 mM HEPES, 110 mg/L sodium pyruvate, 50 μM BME, and 1% Pen/Strep in 5% CO_2 at 37°C). CH27 cells were transiently transfected with post-translational lipidation signal sequences fused to the mEos3.2 photoactivatable fluorescent protein. For mEos3.2, YFP, and FLAG tag construct expression, 700,000 CH27 cells were transfected with 1 μg plasmid DNA using Lonza Nucleofector electroporation (Lonza, Basel, Switzerland). Cells were plated at 100,000 / ml and grown overnight on glass bottom wells (MatTek Corporation, Ashland, MA). In some cases, especially GG, cells were grown overnight in flasks, spun down, and washed extensively in media, and then plated on the same day as fixation or experiment to minimize the amount of background mEos3.2 that occurs when constructs escape from cells. For

clustered CTxB, plasma membrane GM1 was bound with biotinylated CTxB conjugated to Atto 655 (bCTXB-655) at a concentration of 74.3 nM bCTXB-655 for 10 minutes at 37ºC. B cells were washed with 37ºC Tyrode's buffer before clustering CTxB with 0.1 mg/mL Streptavidin for 5 minutes at room temperature. For clustered TM experiments, TM bearing an extracellular YFP tag was transfected into CH27 cells and subsequently clustered with 13 µg/mL anti-GFP rabbit IgG conjugated to biotin (ThermoFisher) for 30 minutes at room temperature in cell media. Cells were subsequently washed with Tyrodes buffer and stained with 100 µg/mL streptavidin for 10 minutes prior to fixation. For BCR experiments, $f(Ab)_1$ fragments conjugated to both Atto 655 and biotin were used to label endogenous BCR in the plasma membrane. Cells were stained with 5 µg/ml labeled $f(Ab)_1$ for ten minutes with extensive washing with PBS buffer prior to clustering with 2 µg/mL streptavidin during either live cell imaging or prior to chemical fixation.

Cells were fixed with a combination of 4% paraformaldehyde and 0.1% glutaraldehyde in PBS buffer for 10 minutes at room temperature. Primary cells were purified from a C57BL/6 mouse (Jackson Laboratories) using standard negative selection procedure. Briefly, one mouse was sacrificed using CO_2 asphyxiation. Spleen and lymph nodes were harvested in the presence of DNase I and filtered through a 70 µm strainer. Cells were pelleted and resuspended in DMEM with 2% FBS, 10 mM HEPES, 50 IU/mL penicillin, 50 µg/mL streptomycin, and 0.2 mg/mL DNAse I. 5 µg/mL CD11c (clone N418, Biolegend) and 5 µg/mL CD43 (clone S7, BD Biosciences) biotinylated antibodies were added to cells for 30 minutes on ice prior to red blood cell lysis with RBC lysis buffer (0.14 M NH_4Cl and 0.017 M Tris, pH 7.2) and washing by pelleting. Remaining cells were incubated with streptavidin MACS beads (Miltenyi Biotec) for 20 minutes on ice and non-B cells were removed using an Automacs (Miltenyi Biotec) on the DEPLETES protocol. Primary B cells were then put into a buffer recommended by Lonza: RPMI 1640 supplemented with 10% FCS, 2 mM glutamine, 50 µM 2-mercaptoethanol, and 50 µg/mL LPS for 24 hours. Electroporation was accomplished with the P4 Primary Nucleofector solution with electroporation program DI-100 (Lonza) using 600,000 cells with 0.6 µg plasmid DNA in each well. Cells were grown overnight in flasks, spun down and washed extensively in cell media, and then plated onto fibronectin plates for 2 hours prior to labeling with $f(Ab)_1$ Atto 655, stimulation with streptavidin, and fixation as described above.

4.4.4: TIRF microscopy

Imaging was performed on an Olympus IX81-XDC inverted microscope with a cellTIRF module, a 100X UAPO TIRF objective (NA=1.49), active Z-drift correction (ZDC) (Olympus America, Center Valley, PA). Images were acquired on an iXon-897 EMCCD camera (Andor, South Windsor, CT). Excitation of Atto 655 was accomplished using a 650 nm diode laser (OBIS, 100mW, Coherent, Santa Clara, CA) when also imaging mEos3.2, or a 640 nm diode laser (CUBE 640-75FP, Coherent) when also imaging Alexa 532. Excitation of mEos3.2 constructs was accomplished using a 561 nm diode laser (Sapphire 561 LP, Coherent). Photoactivation of mEos3.2 was accomplished with a 402 nm diode laser (CUBE 405-50FP, Coherent). Excitation of Alexa 532 was accomplished with a 532 nm diode-pumped solid-state laser (Samba 532-150 CW). Laser intensities were adjusted such that single fluorophores could be distinguished in individual images. Excitation and emission was filtered using the quadband cube LF405/488/561/635-4X-A-000 (Semrock, Lake Forest, IL) or a 532/640 dualband cube (TRF59907, Chroma, Bellows Falls, VT). Emission was split into two channels using a DV2 emission splitting system (Photometrics, Tuscon, AZ) using a T640lpxr dichroic mirror to separate emission, ET605/52m to filter near-red emission, and ET700/75m to filter far-red emission (Chroma). Live and fixed samples with ATTO 655 and mEos3.2 were imaged in a buffer suitable for STORM and PALM microscopy: 30 mM Tris, 9 mg/ml glucose, 100 mM NaCl, 5mM KCl, 1 mM KCl, 1 mM $MgCl_2$, 1.8$CaCl_2$, 10 mM glutathione, 8 µg/ml catylase, 100 µg/ml glucose oxidase, pH 8.5. Fixed samples with ATTO 655 and mEos3.2 were imaged in a buffer more suitable for oxazine and rhodamine dyes[123]: 50 mM Tris, 100 mg/mL glucose, 10 mM NaCl, 100 mM 2-mercaptoethanol, 50 µg/ml glucose oxidase, 200 µg/ml catalase, pH 8.

4.4.5: Single molecule localization

Single molecule fluorescent events were localized by fitting local maxima in background subtracted images to Gaussian functions using standard methods and the ensemble of peaks was then culled to remove outliers in brightness, size, and localization error. Localizations in the near-red channel were registered with the far-red channel using a registration technique published previously[156]. Briefly, 100 nm diameter Tetraspeck beads with fluorescence emission

in both near and far-red channels (Invitrogen) were adhered to glass slides, excited by both 561 nm and 640 nm lasers, and 70 fluorescent images of 20-40 beads were collected before and after the acquisition of each data set. These diffraction-limited fluorescent beads were used as control points to create a polynomial transform from the near-red channel to the far-red channel, and this polynomial transform was applied to mEos3.2 localizations in the near red channel. Stage drift correction was performed every 500 frames by finding the maximum in the 2D cross correlation produced by all localizations between successive groups of frames. Super-resolution localizations are used to make super-resolved images after correcting for stage drift and emission channel registration by incrementing the intensity of pixels at positions corresponding to localized single molecules. Cross-correlation analysis was performed on these images using previously described methodology[138,200]. Cross-correlations from live cells were performed as in reference 200, where the time evolution of the cross correlation was used to better describe the instantaneous cross-correlation. For step-size analysis, single molecule trajectories were constructed from super-resolution localizations using a tracking algorithm that searches for localizations within 500 nm in subsequent frames and terminates ambiguous trajectories[203]. The step size distribution for BCR-correlated probe is calculated by finding all instances of probe localization within 100 nm of a simultaneous BCR localization.

4.4.6: Ising model simulation

A conserved order parameter 2D Ising model was simulated on a 256 by 256 square lattice as described previously[152] with minor modifications. Briefly, components that prefer Lo or Ld regions are represented as pixels that have value of +1 and -1 respectively. The vast majority of +1 and -1 pixels represent unspecified membrane components (proteins and lipids). In addition, 50 pixels with values of +1 are classified as receptors, 100 pixels with values +1 are classified as kinases, and 100 pixels with values -1 are classified as phosphatases. At each update, two random pixels are chosen, the energy cost or gain to exchanging the two pixels is calculated, and the move is either accepted or rejected using a Monte Carlo algorithm that maintains detailed balance. If the resulting configuration is lower or equal in energy, the exchange is always accepted. If the energy is raised, the exchange is accepted stochastically with probability $\exp(-\beta\Delta H)$ where β is the inverse temperature and ΔH is the change in energy between initial

and final states. In this scheme, the critical point occurs at Tc = 2/ln(1+sqrt(2)). Simulations with fluctuations were run at T=1.05Tc and those without were run at T=2Tc. One pixel is chosen to represent a 2nm by 2nm patch of membrane, so that the correlation length varies with temperature as observed in experimental observations in isolated plasma membrane vesicles[74]. One sweep corresponds to the option to exchange each of the pixels on average twice (256^2 pixel swaps are proposed). All simulations are initially run using non-local exchanges to decrease equilibration times and then exchanges are restricted to nearest neighbors in order to better mimic diffusive dynamics. Simulation sweeps are converted to time assuming a diffusion coefficient of roughly $4\mu m^2/s$, with 1 sweep corresponding to roughly 1μs. Receptors are clustered by applying a strong circular field at the center of the simulation frame that only acts on receptors.

If a move is accepted that places a receptor neighboring a kinase, then the receptor activation state is incremented with a low probability (0.2%). If a move is accepted that places a receptor neighboring a phosphatase, then the receptor is completely deactivated at a high probability (100%). These probabilities are chosen to produce a low level of activation in a well-mixed simulation that contains an equal number of kinases and phosphatases. Higher probability of deactivation is also physiologically relevant because deactivating components such as CD45 are expressed in the plasma membranes of lymphocytes at several-fold higher densities than Src kinases (e.g. T cells express between 100,000 and 500,000 CD45 molecules and between 40,000 and 120,000 Lck molecules per cell[230,231]. In some simulations, receptors have kinase behavior when they are multiply activated (≥2 activations). In this case, a move that places a multiply activated receptor next to a second receptor results in the second receptor becoming activated at a low probability (0.2%). All analyses were carried out in MATLAB (The MathWorks, Natick, MA).

4.4.7: Calcium measurements

5 million CH27 cells were loaded with 2 μg/mL fluo-4 (ThermoFisher) for 5 minutes at room temperature in 1 mL Tyrodes buffer with 0.25 mM sulfinpyrazone (T/S buffer). Cells were subsequently diluted to 15 mLs T/S buffer and allowed to load for 30 minutes at 37°C. 700,000 cells in 1.8 mL T/S were then treated with either methyl-β-cyclodextrin (MBCD) or MBCD

loaded with cholesterol (Sigma) at 37^{o}C for 15 minutes. The concentration of both MBCD+cholesterol and MBCD were determined by the molecular weight of MBCD alone. Cells were then spun down and resuspended in 1 mL of phosphate buffered saline + 0.25 sulfinpyrazone (P/S buffer). Cells were then spun down again and resuspended in 400 uL P/S for each condition. Fluo-4 was visualized on a fluorescence plate reader (Omega) using excitation centered at 485 nm and emission centered at 520 nm. Cells were stimulated by addition of f(Ab)$_2$ rabbit anti-mouse IgM (Jackson) to a final concentration of 3 μg/mL.

Chapter 5: Conclusion

Our application of super-resolution microscopy helps to resolve a difficult problem in B cell membrane biology by showing directly that compositional heterogeneity exists around clustered B cell receptors and influences the partitioning of proteins which regulate BCR signaling. In this chapter, I will review the implications of these results and future directions that this work may motivates. First, our results are consistent with B cell receptors stabilizing critical fluctuations into long lived and large domains, and this strategy may be advantageous for the B cell to respond to diverse antigens. Second, our results provide evidence that membrane domains may act as regions of altered phosphorylation which could impact the activation state of co-receptors as well as Src kinases. Third, the multicolor super-resolution techniques detailed here can be used in a variety of contexts to investigate protein behavior in cells. Finally, I conclude with highlighting a new paradigm for understanding the immunomodulation effects of some anesthetics, and I review unanswered questions that have bearing on this work.

5.1: Membrane domains around BCR clusters have a functional role

Our work clarifies two long-standing questions regarding whether domains form around B cell receptor clusters and whether these domains are involved in receptor signal propagation. Our work also supports a model where the cell membrane exists near a critical point for ordered and disordered phase coexistence and this proximity to a critical point allows transient and small fluctuations to be stabilized into larger compositionally distinct domains. Utilizing membrane composition fluctuations may be particularly advantageous for BCR signaling since this receptor must be able to respond to a nearly endless array of antigen epitope architectures and patterns. Linking spatial control of receptor phosphorylation and cytoskeleton may also be important for the cellular coordination of receptor signaling and internalization. The domain around clustered

BCR may be more pronounced when immune synapses form, since some proteins with phase preference, including CD45, can be forcibly excluded or enriched in areas of close cell adhesion. Overall, membrane domains may represent one method for the B cell to spatially tune their biochemical responses to external stimuli.

5.1.1: B cell plasma membranes may reside near a critical point

This work is consistent with a model where receptor clusters preferentially interact with ordered compositions in a membrane near a critical point for liquid-order and liquid-disorder phase coexistence. This model predicts that both ordered and disordered domains can form by clustering proteins that favor interaction with ordered or disordered compositions. In systems with an equal fraction of phases and under similar clustering conditions, induced ordered and disordered domains have correlation functions with inverse magnitude. Our data show that ordered domains can be made by clustering either the BCR or CTxB, and disordered domains can be made by clustering TM. Additionally, the magnitude of cross-correlation between the clustered proteins and the phase markers is very similar between ordered or disordered protein clustering, consistent with the predictions of a critical system. This model predicts that probe enrichment in the BCR cluster is limited since the system is above its phase transition temperature. Our data is consistent with this prediction, since the correlations we observe are fairly weak, and are not greater than the thermal energy present in the system. Further, we provide evidence that the domains we observe are not gel, since the diffusion of our membrane probes, particularly PM, is not altered in the presence of the BCR cluster.

We utilize the Ising model to simulate receptor phosphorylation in a critically fluctuating membrane when activating kinases are ordered components and deactivating phosphatases are disordered components. Interestingly, we see good agreement between the magnitude of signaling responses to receptor clustering when the membrane phase fraction is perturbed. Use of the Ising model allowed a quantitative prediction to be made about the B cell membrane without knowing all the components of the system. The critical model for membrane phase fluctuations allows the phase behavior of highly complex membranes to be modeled without any knowledge of the specific composition of the membrane, and may thus be a very useful model for understanding other membrane-based processes.

5.1.2: Domain stabilization is a constant response to binding varied antigens

It is possible that domain stabilization could initiate signaling in response to antigen clustering, and this mechanism may be advantageous to the B cell since it would allow for the BCR to respond to any clustering antigen. B cell receptors recognize a wide array of antigens which are presented in a nearly endless array of epitope configurations. The formation of membrane domains around clustered BCR would allow the B cell to respond to antigen induced clustering of the BCR in the face of endless variability in the target antigen. Domain stabilization is independent of the chemical species of the epitope the receptor binds to (be it protein, lipid, or glycosylation), but may depend strongly on the strength of receptor-epitope binding and thus can also indicate the strength of antigen binding to the cell. For instance, weakly binding receptors are able to unbind the antigen and diffuse away from the cluster, and the domain observed would have a greater probability of disordered phase fluctuations occurring within it because there are less receptors that are creating the domain. Although these weak antigens could still result in stimulation, the receptor phosphorylation would be diminished since phosphatase is less excluded and kinase is less enriched. Differing domain composition in response to binding stronger or weaker ligands could be a mechanism for BCR to sense the avidity of ligand binding, an important part of the selection of B cells[232]. Additionally, although conformational change of the BCR has been reported during the binding of membrane bound antigen, this conformational change acts to cluster and oligomerize BCR immunoglobulin domains in response to pulling forces between opposing membranes[55], which in conjunction with resisting membrane curvature may be a mechanism for BCR to cluster in response to monovalent ligands presented on surfaces. A simplified diagram of the partitioning of regulatory proteins around nascent BCR clusters is provided in **Figure 36**. It is thus possible that B cell receptors utilize membrane domains as a mechanism to initiate signaling in response to clustering by non-specific ligands.

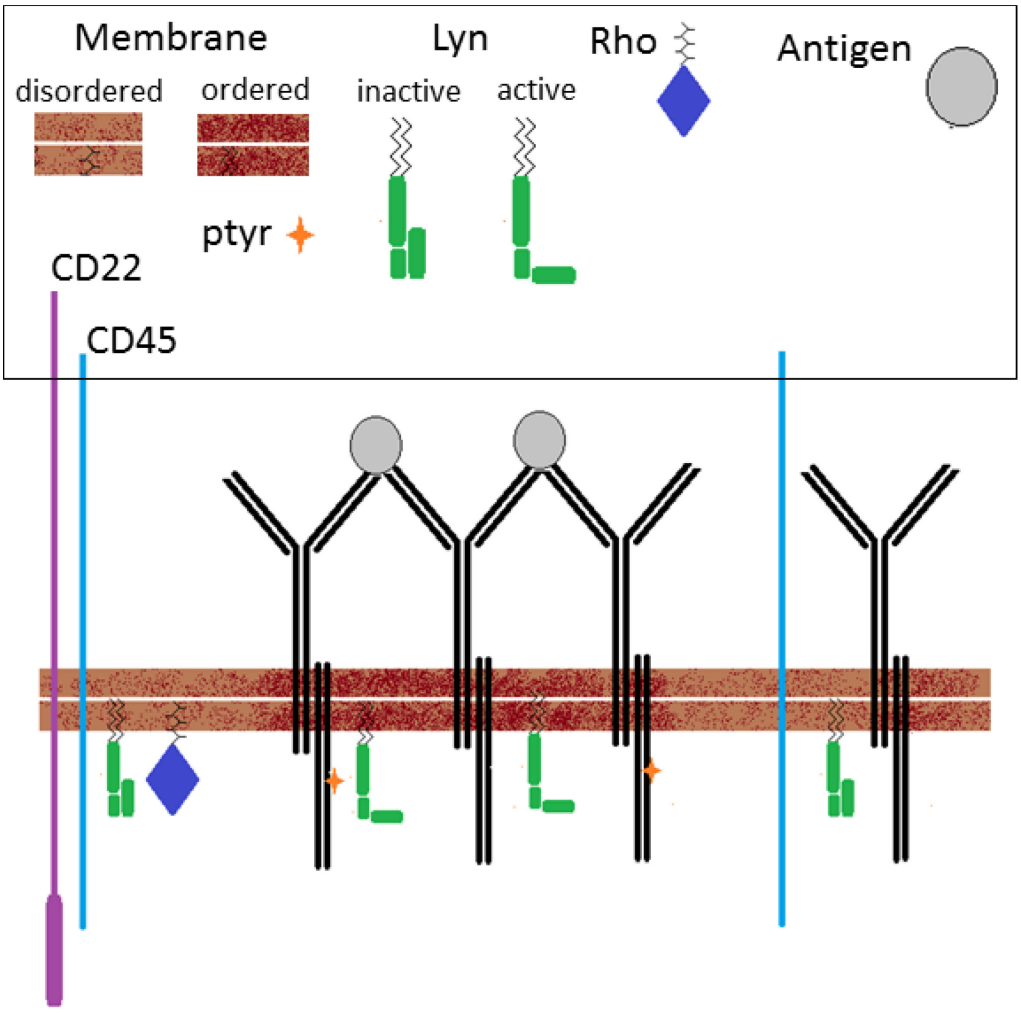

Figure 36: The moments following BCR antigen binding

B cell receptor signalling may be initiated by stabilizing an ordered domain around receptor clusters. Antigen forces the receptors to cluster, which consequently forms an ordered domain in the plasma membrane. This ordered domain is enriched in the kinase Lyn and depleted of the phosphatases CD45 and CD22 and the geranylgeranylated Rho family GTPases. Lyn activity may also be higher in the ordered domain than elsewhere, and ITAMs may be more ordered due to the presence of the membrane domain. Here, ordered domain is drawn as speckled to emphasize that ordered domains are stabilized fluctuations around the B cell receptor cluster, and these ordered fluctuations exist elsewhere in the plasma membrane as well.

5.1.3: Cytoskeleton linkages to the plasma membrane may utilize domains for spatial control

Membrane domains may provide gradients in the concentration and activity of Rho family GTPases allowing for controlled actin polymerization as well as internalization and capture of antigens. The remodeling of the cortical cytoskeleton is important for BCR cluster formation

and signaling[233]. RhoA is activated following BCR stimulation and inhibition of RhoA reduces calcium responses to antigen stimulation[234]. CDC42 is critically important for the development of B cells; its deletion blocks cells from passing the pre-B cell phase[235], and it is known to assist in the remodeling of actin structures through interactions with the Wiskott–Aldrich syndrome protein. CDC42, RhoA, and Rac1 all bear geranylgeranylations on their C-termini[236] which assist in their localization to the plasma membrane[237]. The results of this work suggest that these GTPases should have a lower concentration near BCR clusters due to their geranygeranyl modifications due to its unfavorable partitioning into ordered membrane domains. It is possible that this concentration gradient of GTPases could aid in the cytoskeleton remodeling that happens during BCR signaling, such as the spreading and contracting of the B cell membrane in response to antigen binding and antigen gathering[238]. Further, CDC42 and other Rho GTPases are also phosphorylated by Src kinases, and both the activity and concentration of Src family kinases may be distinct within domains. Interestingly, clustered GPI-proteins are also correlated with an increased actin density[139], which further indicates the regulation of the cytoskeleton by membrane domains since GPI clusters likely form ordered domains as well. These non-uniform distributions of Rho family GTPases also occur in neuronal synapses, where Rac1 spatial patterning can regulate the elongation of actin networks in dendritic spines[239]. The coupling of Rho family GTPases and other cytoskeletal regulatory proteins to membrane domains may thus allow for spatial regulation of actin and cytoskeletal network remodeling and organization.

5.1.4: B cell receptor immune synapse could have more pronounced compartmentalization due to forced exclusion of some proteins

The ordered domains around BCR clusters may be further stabilized when BCR recognizes membrane bound antigens due to the forced exclusion of disorder-favoring large glycosylated proteins from the immune synapse. B cell receptors often recognize targets on the surface of antigen presenting cells such as follicular dendritic cells, and binding to their target antigen in this context forms an immune synapse. When B cells recognize their target antigen presented on the surface of another cell, the B cell will adhere to the antigen presenting cell, search for additional antigen on the cells[238], and then aggregate the antigen into a central synapse from which the B cell internalizes antigen[21]. Tight adhesion of the synapse may act to exclude some

proteins from the synapse, as seen in T cells where CD45 is excluded from the TCR-APC synapses due to the bulky ectodomain of CD45[54]. This process happens in B cell synapses, where very strong exclusion of CD45 and CD22 was observed between B cell and antigen presenting cell[21]. This forced repulsion of CD45 from the B cell receptor synapse would help stabilize a disordered domain outside of the synapse since the transmembrane domain of CD45 is coupled to disordered plasma membrane. Both CD45 and CD22 have large glycosylated ectodomains which likely leave areas of close membrane juxtaposition to minimize the high energy cost of membrane bending. CD22 is also not detergent resistant[93], suggesting that it may also be coupled to disordered membrane, in addition to recruiting the tyrosine phosphatase SHP1. Together, this suggests that clusters of BCR in the synapse may have an even more stabilized ordered membrane domain since adhesion is forcibly locating these proteins to the outside of the synapse.

5.2: Membrane domains as regions of altered phosphorylation profiles

Ordered membrane compositions may generally act as distinct phosphorylation environments for a variety of substrates. Both the phosphorylation state of the co-receptor FcγRIIb and Src kinases may be distinct in membrane domains. Interestingly, simply clustering membrane order-preferring proteins can activate some cell types, suggesting that this is a generalized mechanism to initiate some signaling pathways. In summary, domains may represent a distinct compartment for phosphorylation and other regulatory modifications.

5.2.1: The co-receptor FcγRIIb may utilize the domains to signal

The co-receptor FcγRIIb may experience altered phosphorylation simply by being present in an ordered membrane domain, which could activate its inhibitory effect on B cell activation. FcγRIIb recognizes IgG immunologobulins which are produced after the body has already undergone the adaptive immune response. Mature B cells can bind to an antigen that is also bound by an IgG, which brings FcγRIIb into close proximity of the BCR clusters. FcγRIIb downregulates BCR signals through the phosphorylation of ITIM residues on FcγRIIb. In agreement with this, co-ligation of the BCR and FcγRIIb prevents the large-scale spreading response as well as the receptor slowdown normally observed after BCR ligation, indicating that

the receptor is not inducing the normal cytoskeletal reorganization[39]. Further, the conformational changes associated with the CD79a C-terminal subunit are also blocked[39], which may reflect that the ITAM subunits of the BCR remain embedded in the membrane. Interestingly, the PM probe is co-localized with FcγRIIb following BCR co-ligation, indicating that the membrane domain around clustered BCR is not perturbed under co-ligation with FcγRIIb[39]. It has been shown that a variant of FcγRIIb associated with Lupus has a decreased presence in detergent insoluble membrane fractions due to a mutation in a transmembrane residue from an isoleucine to a threonine[97,240]. This mutated FcγRIIb also exhibits a reduced phosphorylation and attenuated recruitment of SHIP when colligated to BCR, suggesting that its presence in membrane domains may be important for FcγRIIb's phosphorylation and downstream signaling and thus its downregulating effect on immunoglobulin production[97,240]. It may be that the enhanced phosphorylation in domains initiates signals emanating from FcγRIIb, and disruption of membrane domains around FcγRIIb may lead to reduced phosphorylation of FcγRIIb and excessive activation of B cells. Phosphorylation of the mutated and disorder preferring FcγRIIb co-ligation with the BCR could also be simulated with an Ising model. Here, FcγRIIb would be chosen to be a disordered component which could also be phosphorylated. In this way, we can use our results showing that the critical model is valid and apply it to a clinically relevant system.

5.2.2: Src kinase activation state may be distinct in domains

Src kinases may also experience an altered phosphorylation profile in membrane domains. Src kinases are regulated by phosphorylation on two key residues; a tyrosine at residue 508 (human Lyn) that inhibits kinase activity and a phosphorylation on a tyrosine at residue 397 (human Lyn) that increases kinase activity. The inhibitory 508 residue is phosphorylated by Csk, and when Csk is deleted only the 397 residue is phosphorylated and Lyn is overactive[50]. Csk associates with the plasma membrane through the Csk binding protein (Cbp, also known as PAG), which has a transmembrane domain and is doubly palmitoylated. Cbp and the Csk-Cbp protein complex are also found in detergent resistant membrane fractions[241], which could lead to a distinct regulatory phosphorylation of Lyn in membrane domains. In addition, CD45 can dephosphorylate both the 508 and the 397 residues of Lyn, and after BCR clustering both Lyn tyrosine residues become phosphorylated[49,242], suggesting that CD45 exclusion from BCR is

necessary for Lyn and other Src kinases to achieve the activation state necessary to phosphorylate BCR. The activation of Src kinases may be even more complex than this since the Cbp-Csk complex is likely enriched in the BCR induced domain, where it would act to phosphorylate the inhibitory 508 residue and potentially dampen the signaling response to BCR clustering. Overall, Lyn and other Src kinases are important kinases that are present in the not only the B cell receptor signaling pathway but also play a role in the phosphorylation of many other proteins, including other immune receptors as well as membrane proteins that regulate neuronal polarity[243]. It will be important to determine how the activity of Lyn and other Src kinases may be altered by ordered membrane domains. It may be possible to use antibodies specific to Lyn phosphorylation to examine what is the phosphorylation state of the Lyn that is close to the receptor cluster. This would involve comparing the cross-correlations between BCR and phosphorylated Lyn-397 to the cross-correlation between BCR and phosphorylated Lyn-508. It may be expected that Lyn outside of the BCR cluster would have a lower phosphorylation due to the ability of CD45 to dephosphorylate both regulatory tyrosine residues[49], and Lyn phosphorylation could also be strongly affected by the presence of other Lyn within the domain that may phosphorylate trans-phosphorylate each other.

5.2.3: Domains may provide a generalized platform for membrane protein activation

Clustering an ordered preferring component and creating an ordered domain is sufficient to induce phosphorylation of proteins and motivate calcium release in some cell types, indicating that ordered domain formation could be a generalized signaling mechanism. Our results show that domains are enriched in the kinase Lyn and depleted of the phosphatase CD45, and simulations of phosphorylation suggest that this altered concentration of regulatory proteins can stimulate the BCR. Additionally, domains could phosphorylate any protein that is regulated by Lyn and CD45 since domains are depleted in CD45 and enriched in Lyn. It has been shown that clustering GPI-anchored proteins on neutrophils acts to stimulate the cells[244], which does not have an obvious cause since these proteins do not have intracellular or transmembrane domains to interact with effector proteins. This was also observed in T-cells and an epithelial cell line, where the recruitment of Lyn to the cluster as well as cell stimulation was also noted[245,246]. It was also seen that clustering cholera toxin subunit b acts to induce phosphorylation of effectors

downstream of TCR activation[247]. These results suggest that certain cell types may respond to membrane domain formation by phosphorylating specific proteins. Interestingly, a substrate for focal adhesion kinase is more phosphorylated with the PM anchoring compared to the GG anchoring, indicating that FAK is more active in resting ordered membrane without domain stabilization[248]. These observations indicate that ordered membrane compositions have a different phosphorylation profile, and proteins may become activated when outside forces stabilize domains by clustering ordered-preferring proteins in the membrane.

5.3: Quantitative multicolor super-resolution microscopy enables detailed studies of molecular interactions *in vivo*

Our work helps to advance methodologies for quantitative multicolor super-resolution microscopy, where quantitative means that protein co-distributions can be accurately determined in terms of absolute enrichment or depletion. This experimental approach provides a wealth of information that allows comparisons to be made between data and predictive models such as the Ising model, and potential of mean forces can be estimated from the observed enrichment or depletion. This mode of super-resolution microscopy is ideal for structures larger than the resolution limit, making it well suited to fill the gap between traditional and FRET microscopy. In live cells, cross-correlations between labeled proteins and the dynamics of individual molecules can be simultaneously determined, which can allow transient states to be examined in greater detail.

5.3.1: Quantitative super-resolution microscopy enables the long range interactions between membrane proteins to be determined

Super-resolution microscopy is an important tool for observing large-scale architecture and organization of biomolecules in cells that bridges the gap between FRET and traditional microscopy. Large-scale organization and spatial patterning occurs in a variety of biological contexts, including receptor clustering and capping[233], cytoskeletal networks[125], and sites of adhesion[238], for example. It is of interest to find patterns within individual elements and between large-scale architectures of the system. FRET and traditional microscopy are useful tools to

observe interactions between biomolecules in cells, however super-resolution microscopy bridges an important spatial gap between these two methods. FRET is a good measure for short range interactions between labeled proteins, however it cannot provide information on length scales much greater than the Förster distance, which is between 1 and 10 nanometers depending on the fluorophore[106], and traditional fluorescence microscopy is unable to resolve structures less than about 200 nm at best, due to the diffraction limit of light. Super-resolution microscopy is an ideal tool for investigating large scale structures that occur in cells, especially those that have a length scale greater than 25 nm, the approximate resolution of STORM experiments. We show that it is also possible to measure very weak co-distributions between labeled objects. This methodology could be extended to a variety of biological systems, and will be especially important for measuring spatial organization that is impossible to resolve by traditional microscopy and is too large for FRET.

5.3.2: Simultaneous cross-correlation and dynamics can be informative of transient states

Transient states, such as the brief correlated positions of two objects or a segment of a trajectory that exhibits confined motion, can be examined in detail by simultaneously determining cross-correlations and individual molecule dynamics. We examined the diffusive step-size for PM and TM protein near BCR clusters, which informed us on the physical state of the membrane near the BCR clusters[200]. This analysis scheme could also be done in reverse, where trajectories of an object exhibiting two different modes of diffusion could be classified into different states, and those states could be individually spatially correlated with another target enabling further insight into the transient state. For example, it is thought that GPI proteins become transiently immobilized in "corrals" created by cytoskeletal elements[140]. It may be possible to simultaneously observe the correlation between a labeled cytoskeletal element and the labeled GPI anchored protein, and observing the correlation function between them for times when the GPI anchored protein is in or hopping between the corrals. Additionally, it is thought that the BCR becomes immobilized by binding to cytoskeletal elements[233], which could easily be tested using this technique. In general, it is useful to determine both the cross-correlation function and the dynamics of individual proteins at the same time in live cells, and this methodology can reveal new information about the dynamics of proteins and interaction between molecules.

5.3.3: Quantitative Super-resolution microscopy enables detailed molecular questions to be asked

An important facet of this work was the quantitative nature of the cross-correlation functions determined from super-resolution data, where quantitative implies that the absolute value of the relative enrichment or depletion is given by the correlation function. Quantitative also implies that the baseline for the cross-correlation measurement is 1, and there are no residual biases in the measurement. Cross-correlations determined for ordered and disordered membrane anchors have close to identical absolute magnitudes for all protein clusters tested. This is a good indication that our measurement is relatively free of bias, since neither enrichment nor depletion is favored in the experiment. This could be tested directly using a "null" protein that does not favor partitioning into ordered or disordered domains such as palmitoylated LAT which shows little ordered or disordered phase preference in GPMVs[135]. The expected cross-correlation between a clustered phase-preferring protein and the null protein is a flat line having a value of one since it should be neither enriched nor depleted from the cluster. The quantitative nature of these experiments is an important asset of this work; it allows the potential of mean force (PMF) to be reliably estimated and facilitates comparisons of experimental cross-correlations to those from simulations from the Ising model.

5.4: Going forward

5.4.1: Anesthetics could perform immunomodulation by manipulating membrane domains

It may be possible to modulate the immune system by changing how easily the cell membrane can stabilize a domain. Gray et al showed that it is possible to lower the transition temperatures of blebs using anesthetics[77], which was evidenced by a lower proportion of cells exhibiting coexisting ordered and disordered phases in cells that had been treated with anesthetics. Applied to the results in this Dissertation, this suggests that cells treated with anesthetics would be less able to support ordered domain formation around receptor clusters which may attenuate BCR signaling in response to antigen binding. Indeed, it has been shown that general anesthetics act to immediately lower the number of circulating lymphocytes[249]. Additionally, propofol reduces the outgrowth of T cells[250], and also compromises the murine immune system's response to

Listeria[251] and other organisms[252]. Propofol has also been shown to attenuate damage and cytokine release following septic shock[253,254], which has a protective effect for the patient. Overall, this research suggests that anesthetics and other drugs which alter transition temperatures may have a dampening effect on the immune system. This hypothesis could be directly tested by observing the partitioning of membrane probes used here around cells treated with clinically relevant concentrations of anesthetics. These and similar drugs could also be potentially be useful for the treatments requiring urgent inflammation reduction and immunological control, such as acute autoimmune disease, shock, and transplant rejection.

5.4.2: The view ahead

The work here has provided direct evidence that the plasma membrane of B cells exhibits membrane non-uniformity around the clustered B cell receptor, illustrating that it is indeed possible for domains to exist in the plasma membrane of cells. This work is an important advancement in the understanding of B cells, where better techniques and models were needed to understand the behavior of domains. This work also raises some important questions which may be the focus of future work. It is still unknown how transmembrane protein motifs may be sorted between ordered and disordered membrane environments, and there may be common determinants for partitioning into ordered or disordered phases[255]. What is it about the B cell receptor that acts to stabilize an ordered domain? Some of the proteins that bind directly to the BCR including LAT2 and Lyn bear palmitoylations; it may be these or the receptor structure itself that acts to couple the receptor to the plasma membrane. It is also of interest to determine whether other immune receptors such as the T cell receptor[69] or FcεRI[256] are also coupled to ordered domains. These receptors also recognize a diverse array of antigens, and a domain-based mechanism for activation may be a common theme in this type of receptor. Also, it has been shown that trafficking of transmembrane proteins depends on the proteins affinity for ordered and disordered domains in GPMVs[65], and it is known that membrane trafficking helps to maintain cell membrane polarity in epithelial cells and other polarized cell types. How do membrane domains interact with the cytoskeleton in order to sustain this asymmetry? It is possible that the proteins that help sort vesicles may also have strong phase preference and simultaneously couple to cytoskeleton flow. Finally, it is also known that B cells and other white

blood cells are commonly covered in microvilli structures which add nearly 50% more membrane to the cells compared to if the cells had smooth memrbanes[257]. It may be interesting to investigate how domains may or may not interact with these structures. In conclusion, membrane domains may be involved in a wide array of biological processes, and it will be of interest to determine how the cell might utilize membrane domains to perform various tasks.

Appendix 1: Experimental Protocols

1.1: Transfection via electroporation

1.1.1: CH27s and RBLs

- For RBLs, trypsonize cells, remove cells from flask, add excess cell media to quench trypsin reaction, and spin down cells to completely remove trypsin prior to electroporation.
- Aliquot between 0.5 million and 1 million healthy suspended cells. For more difficult to transfect constructs, such as Lyn, it is good practice to transfect only 0.5 million cells since they are more sensitive to overgrowth and death following transfection.
- Completely remove culture media from pellet after spinning for 5 minutes at 500 x g.
- Cell pellet is then resuspended in:
    - 16.3 µL SF cell line solution
    - 3.6 µL Supplement
    - Plasmid DNA (Generally around 1 µg DNA or less per 1 million cells)
- Cells suspended in transfection media are pipetted into one of well of the multi-well electroporation strip and tapped lightly to ensure bubbles are not on the bottom of curvette
- Well is pulsed by either CA 137 (CH27 cells) or DS 138 (RBL cells) and strip is placed back into hood for 10 minutes
- 40 µL of pre-warmed cell media is then pipetted into the well, and the entire volume in the well is then pipetted into 6 mLs prewarmed cell media. If higher cell density on glass is needed, less media can be used
- Cells in media are pipetted onto glass bottom wells, generally no more than 200,000 per well.
    - For membrane constructs that can easily unbind the membrane, like GG-mEos3.2, it can be helpful to grow cells overnight in a flask instead of on plates to reduce the presence of debris containing mEos3.2 on coverslip surface.
    - The following morning, cells can be lifted from the flask (using trypsin for RBLs), spun down and media replaced twice, and then added to plates.
    - CH27s will adhere to glass plates after an hour if cells are added in small volume (400 µL) and high numbers (200,000 cells per plate)
    - RBLs will adhere to glass plates after ~2 hours

1.1.2: Primary B cells

Primary B cells are more sensitive and require more attention to details to ensure cell viability and transfection. Specifically, cell media should be pre-equilibrated to CO_2 and to temperature. Also, cells should be spun down more gently than CH27s and RBLs, specifically, I used 300 x g for 8 mins, as this is what was used in the Grigornova lab during harvesting.

- Spleen and lymph nodes were harvested from a male C57BL/6 mouse.
- B cells were negatively selected via CD11c and CD43.
- Approximately 30 million cells were harvested.
- Immediately following primary cell harvesting, cells are put into a growth media containing:
    - RPMI 1640 + 10%FBS
    - 2 mM glutamine
    - 10 μM betamercaptoethanol
    - 1 %ITS (Insulin, Transferrin, Selenium, Sodium pyruvate, Ethanolamine, Sigma I3146)
    - 50 μg/mL LPS (γ-irradiated, lyophilized powder, <3% protein, Sigma L6529)
- B cells should be grown for ~20 hours in this media to allow for B cell blast formation, indicated by some cell clumping.
- 600,000 cells per condition were transfected, with 0.6 μg PM, GG, or TM plasmid DNA, using pulse DI-100 under P4 Primary Cell.
    - For more transfection and possibly less cell viability, can increase cell number to 700,000 and use pulse DI-102 or DT-100
- After electroporation, strip was placed in culture hood for 10 minutes at toom temp and then 40 uL of cell media was added to the well, and allowed to sit in incubator for 30 minutes to recover.
    - Cell media was pre-equilibrated to CO_2 by placing in incubator for 30 minutes and was also warmed to 37C
- Electroporated cells were grown in a culture flask overnight.
- Cells were spun down at 300 x g for 8 minutes, resuspended in fresh media, and spun down again before plating on fibronectin plates.
    - Fibronectin plates were made by incubating a 10 μg/mL concentration of fibronectin in Tyrodes (needs calcium) at 37C in incubator for 1 hour or more.

1.2: Sample prep for super-resolution microscopy

1.2.1: Clustering cholera toxin subunit b to make an ordered domain

- Bind live cell plasma membrane with a 1:100 dilution of cholera toxin subunit b (CTxB) conjugated to biotin (Life Technologies, stock is 1 mg/mL) in cell media or Tyrodes buffer.
- Wash 5 times with Tyrodes buffer.
- Cluster CTxB with a 1:10 dilution of Atto 655 labeled streptavidin for 10 minutes at room temperature in Tyrodes buffer.

1.2.2: Clustering Lat mutant to make a disordered domain

- Transfect CH27s with Lat mutant YFP construct, the construct from J. Grover and A. Ono that has the YFP on the extracellular side (Lat mutant YFP (C2A)).
- Bind Lat mutant YFP with a 1:150 dilution of rabbit anti-GFP polyclonal IgG2b biotinylated antibody (Invitrogen) for 30 minutes at room temperature in cell media.
- Wash cells 3 times or more in Tyrodes.
- Further cluster Lat mutant with a 1:10 dilution of Atto 655 labeled streptavidin in Tyrodes buffer at room temperature for 10 minutes.
- At this point, cells can be fixed with 4% paraformaldehyde + 0.1% glutaraldehyde.

1.2.3: Detection of CD45

- CD45 is an endogenous protein that is expressed in CH27s and all other B cells.
- Post chemical fixation, further block plates with "superblock" (cell media + 3% BSA + 3% fish gelatin) for 3 hrs at room temperature.
- Label CD45 with a 1:500 dilution of AF532 anti-CD45 primary antibody in superblock overnight at 4^{o}C
    - Stock is 0.2 mg/mL
    - Antibody is clone RA3 6B2, against CD45R/B220, and is specific for mouse and human CD45
- Wash cells 5 times in PBS to remove all unbound antibody. Use plate quickly, or bound antibody may unbind over time.

1.2.4: Detection of CD45tm

- CD45tm is the transmembrane of CD45 that was cloned October 30, 2015 by MBS.
    - A sequence for mEos3.2 is attached on the intracellular side and a sequence for the FLAG tag is attached on the outer membrane
    - Due to an unforeseen furin protease cleavage site between mEos3.2 and the transmembrane domain, mEos3.2 cannot be used to localize CD45tm
        - Furin cleavage site: (R-X-(K/R)-R)

        - Linker region from CD45 inner membrane, transmembrane proximal CD45 sequence: (R-K-K-R)
        - mEos3.2 is assumedly diffusing around the cytoplasm of transfected cells, although is difficult to detect even with ultraviolet laser irradiation
        - Protease cleavage suggests that CD45 protein structure near the membrane may be somewhat disordered, although this may be more structured in the native protein
- Transfect cells with CD45tm construct.
- After fixation and washing, label extracellular FLAG tag with a 1:100 dilution of mouse anti-Flag in cell media + 3% BSA + 3% fish gelatin at 37^{o}C for 1 hr.
- Wash with blocking solution and PBS.
- Stain cells with a 1:100 dilution of rabbit anti-mouse IgG2b conjugated to Alexa 532 for 1 hr at 37^{o}C.
    - Generally, anti-mouse IgG antibodies with H+L (heavy + light chain) specificity should not be used along with CH27's due to cross reactivity between antibody and IgM light chain. The use of IgG2b specific, not light chain specific, antibodies avoids this problem.
- Wash 5 times with PBS.

1.3: Super-resolution microscopy

1.3.1: General method

Both the STORM buffer and the high amount of excitation light applied to the sample allows fluorophores to reversibly blink. For PALM, blinking is also assisted by buffer and laser intensity, but probe density is largely determined by the amount of UV light applied to the sample and the amount of transfected PALM probe. For PALM, the laser angles for readout and photoactivation should both be kept as shallow as possible so fluorophores within the sample are not unnecessarily photoactivated. Probe density should be high enough to get a well sampled image but not so high as to not allow for individual particle detections. The acquisition time should be adjusted to give fluorophore spots with bright intensity, in practice between 0.01 and 0.05 seconds. Fluorophores are best excited by a TIRF or oblique excitation angle so to include relevant signal in the excitation volume while excluding as much as possible background noise. Preamp gain is always set to 5x and EMCCD gain is usually set between 50 and 200 for STORM and PALM data acquisition. The excitation intensity should be adjusted to give an appropriate photoswitching time and signal density, for Atto 655 this may not be at 100% laser power. It is important to use the autofocus during acquisition to keep the focus on the surface of interest. Some fluorophores and samples may be difficult to photoswitch due to high density of signal. In

this case it may be advantageous to illuminate sample with high laser intensity for some time until enough probe is in the dark state to see individual molecules. Cross-correlation between two probes necessitates accurate transformation between the two emission channels, which is satisfied by securing the DualView dichroic mirror with tape prior to starting imaging, and taking images of fluorescent beads for transformation generation both before and after imaging a sample. Generally, around 50 images of beads, each field of view having 10-50 beads, are taken to ensure accurate transformation across the entire field of view. It is good practice to acquire images of cells prior to photoswitching induction so that the final STORM image can be compared to the image of all fluorophores. To do this accurately, images acquired prior to photoswitching should be in the same focal plane and having the same laser excitation angle as the STORM or PALM data to be acquired. Finally, it should be noted that when using enzymes to deplete oxygen (as should be the case for Alexa 647 and Alexa 532 but not for Atto 655), these enzymes will acidify the buffer over time, and will eventually prevent robust photowitching if the pH becomes too acidic. This can be countered by the addition of Tris or other buffer that will help keep the pH near 8.5. Generally, pH values less than 7 do not yield high quality STORM data.

1.3.2: Buffer for Atto655 super-resolution microscopy

- The oxazine Atto 655 exhibits different photophysics than Alexa 647, and thus performs better in a modified buffer[123] prepared as follows:
    - 10 mL H_20
    - 0.5 mL of 1M Tris
    - 1 g glucose
    - 20 µL 5M NaCl
    - 108 µL betamercaptoethanol
    - pH to 8.5
    - For each mL of STORM buffer, add 100 µL 2mg/mL catalase and 5 µL 10 mg/mL glucose oxidase
- When exciting Atto 655 at 647 nm, the following buffer is superior:
    - 10 mLs Tris-Tyrodes
    - 90 mg glucose
    - 40 mg glutathione
    - pH to 8.5
    - For each mL of STORM buffer, add 100 µL 2mg/mL catalase and 5 µL 10 mg/mL glucose oxidase

- These buffers are suitable for Atto 655, mEos3.2, as well as Alexa 532[123]
- Excitation of Atto 655 is better at 647 nm than 640 nm, although can be performed at either

1.3.3: Buffer for Alexa 647 super-resolution microscopy

- The cyanine dye Alexa 647 works best under very low oxygen and very high reduction agent conditions. Either of the above buffers work well with Alexa 647, however one adjustment should be made:
    - For each mL of STORM buffer, add 20 µL 2mg/mL catalase and 50 µL 10 mg/mL glucose oxidase

1.4: Cloning

1.4.1: CD45 transmembrane domain

(HASPB and KRas were also cloned as well using similar techniques)

- A very long primer (199 nucleotides) was used as a template for the 22 amino acids coding for the transmembrane domain of CD45 (which was determined from the annotated transmembrane domains from sequence deposit UniProtKB - P06800 (PTPRC_MOUSE)).
- 9 amino acids on the intracellular and extracellular side of CD45's transmembrane domain were included in order to maintain transmembrane domain stability and native structure.
    - These primers were checked for secondary structure and unwanted base pairing between themselves and other parts of the long primer using the IDT tool on the web.
- Forward and reverse hanging end primers were used to attach restriction sites to the ends of the insert, with BamHI and EcoRI, and I chose the length of the overhang such that the melting temperatures for the primers were very similar (~55C for the overhang, and ~65 for the whole primers).
- Annealing temperature = 51.6C = Tm(primer)x0.3 + Tm(product)x0.7 – 14.9 was used.
- For PCR, used volumes of reagents recommended by NEB and Phusion polymerase in 20 µL
    - PCR run:
        1. 95C melt for 30 seconds
        2. 98C for 10 seconds
        3. 51.6C for 20 seconds
        4. 72C for 10 seconds (repeat 2-4 25 times)
        5. 72C for 10 minutes
        6. Hold at 4C
    - Purified PCR product with a Qaigen kit
- PCR product and mEos3.2-N1 plasmid were digested with BamHI and EcoRI for 2 hours at 37C
- Digestion product was ran out on a 1.5% agarose gel
    - 75 mL TAE, 7.5 µL Sybersafe, 1.1 g Agarose
    - Ran at 100 V for 40 minutes

    - Gel extracted bands using Qaigen kit
- mEos3.2 vector was treated with Antarctic phosphatase
    - 30 µL mEos3.2 digested vector in H_20
    - 2 µL Antarctic phosphatase
    - 2.8 µL 10X buffer
- Insert was ligated to mEos3.2 vector
    - 2 µL T4 ligase buffer
    - 1 µL T4 ligase
    - 1 µL mEos3.2 digest
    - 16 µL PCR digest
    - Ligated at 16C for 18 hours
- Ligation product was transformed into XL-1 Blue competent cells with heatshock method and plated on Kan^+ plates
- Colonies were miniprepped and sequenced

1.5: Labeling protein with fluorescent dyes

1.5.1: General method for conjugation of dye to IgG

- Ensure that antibody (Ab) buffer does not contain Tris or any free amines.
- Ensure that Ab does not bind to light chains, since this will cross react with our B cells.
- Remove 100 µL of goat anti-mouse IgG subclass 2b.
- Add appropriate volume of pH 9 NaH_2CO_3 to put pH of Ab solution at 8.5.
- Add 1 µL AF532 NHS reactive dye (10mg/mL stock).
- Rotate at room temp for 30 minutes.
- Prepare a PD-10 column by washing through 2 column volumes of PBS-EDTA (1 mM EDTA).
- Add reaction volume to equilibrated buffer, allow it to fully enter the column.
- Flow through PBS-EDTA until protein band has eluted. Free dye will be retained in the column .
- Assay the protein labeling (number of dye / protein) using the nanodrop.

1.5.2: Streptavidin

- 200 µL streptavidin (stock 1 mg/mL) + 1 µL Atto 655 NHS ester is sufficient to label.
- Methods as above.

1.5.3: Annexin

- Dialyze 50 µL Annexin (1mg/mL) + 300 µL BBS in a 10,000 MWCO dialysis cassette against 1L BBS for 48 hours at 4C with 1 buffer exchange.
- label 500 µL of Annexin with 2 µL of Atto 655 NHS ester for 30 minutes at room temperature using methods as above.
- Dialyze against 1L PBS EDTA to remove free dye, overnight at 4C.

1.5.4: CTxb

- CTxB usually comes lyophilized in Tris buffer, so it must be dialyzed against BBS extensively:
    - Dialyze 250 µL of 1 mg/mL CTxB against 2 L of BBS for 2 days at 4C with one buffer change.
    - Remove 500 µL of CTxB after 2 days (0.5 mg/mL = 10 µM).
- Add 1.77 µL biotin (50 µM final) and 0.8 µL Atto 655 (16 µM final).
- Concentrate CTxB to 100 µL (~50 µM).
- Add 5.5 µL 200 mM pH 9 NaH2CO3 to bring pH to 8.5.
- Add 200 µM of Atto 655, reacted for 20 minutes at room temp.

1.5.5: f(Ab)$_1$

- Use 100 µL f(Ab)$_1$ anti-mouse IgM.
- Add 4.5 µL of 200 mM pH 9 NaH2CO3 to bring pH to 8.5.
- Add 0.3 µL Atto 655 and 1.5 µL biotin.
- React for 30 minutes at room temperature.
- Quench with a 1:100,000 dilution of βME.
- Filter on PD-10 column.

1.6: Cell treatments

1.6.1: Latrunculin

- Treat live cells with 2 µM Latrunculin A (stock is 2.37 mM in DMSO).
- Make a 2x working stock by diluting 1.7 µL into 1 mL buffer.

1.6.2: Cholesterol and MBCD

- Make a 100 mM stock of either cholesterol or MBCD assuming the molecular weight of both is 1310 g/mol.
- Treat cells with appropriate concentrations (between 1 and 20 mM generally) for 15 minutes at 37^{o}C.
- Remove cholesterol or MBCD by spinning or washing.

1.6.3: PP2

- Use 40 µM PP2 to totally prevent scr kinase action.
- Need to have PP2 in all buffers used (PBS + Tyrodes + fixation buffer).
- Treat cells with 40 µM PP2 for 5 minutes prior to antigen addition.

1.7: Calcium assay

- Make a 25 mM sulfinpyrazone stock in water (101.2 mg in 10 mLs water).
- Prepare 20 mLs of T/B/S: 20 mLs Tyrodes + 20 mg BSA + 200 µL stock sulfinpyrazone(0.25 mM final concentration).
- If needing to do calcium-free buffer, use P/B/S + 0.1 mM EDTA to chelate calcium.
- Spin down 5 million cells, suspend in 1 mL T/B/S + 2 µL Fluo-4 stock (stock at 1 mg/mL in DMSO + 6% pluronic).
- Let sit for 5 minutes at room temperature, then dilute cells into 15 mLs T/B/S and put into 37C incubator for 30 minutes.
- Spin down to remove fluo-4, suspend cells to about 2 million/mL final concentration.
- Load around 160 µL cells in each well for plate reader assay.

Appendix 2: Code and Software

2.1: Matlab code to give cross-correlations in live cell data

The following code calculates the pair-correlation either between two sets of particles from the same frame (instantaneous cross correlation) or can return the cross-correlation between the same data through time (time auto-correlation). Thus, this code can be used to analyze both the co-distribution between two sets of molecules as well as the dynamics of one set of molecules. This code is given in a format that can be directly copied and pasted into a Matlab editor.

```
function [corrs params] = Spatial_Temporal_Xcorr(data1, data2, mask, calib, dr,max_tau)
% corrs = Spatial_Temporal_Xcorr(data1, data2, mask, calib, dr,max_tau)
%
% SPATIAL_TEMPORAL_XCORR calculates pair-cross correlation between two sets of particles
% (data1 and data2) falling within a region of interest specified by mask,
% and returns C(r,tau) in the structure CORRS, with fields C_11 and dC_11
% for the autocorrelation (G(r,tau)) of the DATA1, C_22 and dC_22 for the
% G(r,tau) of DATA2, and C_12 and dC_12 for the cross correlation of DATA1
% and DATA2. C_12 correlates DATA1(t) with DATA2(t+tau), whereas C_21
% correlates DATA2(t) with DATA1(t+tau). SPATIAL_TEMPORAL_XCORR also
% returns the structure params which contains the field radii, the
% interparticle distance for the bins C(r,tau) and G(r,tau) given in
% nanometer units.
%
% DATA1 and DATA2 are structures with numel(DATA1) == numel(DATA2) = number
% of frames to be correlated and have fields x and y corresponding to the x and y
% positions of particles in each frame. DATA1(i).x is a column of all x positions in
% frame i. DATA1(i).y is the column of y positions and is the same size as
% DATA1(i).x.  DATA1 and DATA2 should be in register with each other.
%
% x and y should be in units of pixels, do not
% have to be integers, and should be given as column vectors
% for example [DATA1(i).x  DATA1(i).y] returns a 2 column matrix that gives
% the x and y position of all particles in frame i.
%
% MASK is a logical matrix with 1's specifying the region of interest,
% having the same pixel units as DATA. size(MASK) = [xdim ydim]; thus the
% first dimension of MASK corresponds to DATA.x
```

```
%
% CALIB is the length of one pixel in units of nanometers
%
% DR is the one dimensional bin length for the radii histogram M(r), in units of nanometers
%
% MAX_TAU is the maximum number of frames to correlate over. Set MAX_TAU to
% zero to only calculate C(r,tau=0). When MAX_TAU=0 G(r,tau) is not
% calculated for either channel.
%
% NOTE: Autocorrelations can be normalized
% to probability density (PDF) by using Go(r,tau) = G(t,tau) - 1, and the
% PDF(r,tau) = Go(r,tau)/sum(Go(r,tau)*dr*mean_rads*2*pi)

%%%%%%%%%%%%%%%%%%%%%%%%%%%%%%%%%%%%%%%%%%%%%%%%%%%%%%%%%%%%%%%%%%%%%%%%%%%%%%%

dr =dr/calib; % convert bin size to pixel
max_r = 15*dr; %the maximum length to correlate out to
rad_dist_bins = 0:dr:max_r; % the 1D spatial bins to histogram radii
Nframes = numel(data1);%getting the number of frames by the number of elements in the data1
%structure
mask_area = sum(sum(mask));
siz = size(mask);
k = [1 cumprod(siz(1:end-1))]; %initializing for sub2ind workaround to
%increase performance

all_dts = 1:max_tau+1; % real taus are 0:max_tau, to designate taus as
% indexes in structures here using 1+taus to avoid indexing into 0

for t = all_dts
   %initializing M(r) histograms at each time shift
   all_taus(t).M_11 = zeros(1,numel(rad_dist_bins));
   all_taus(t).M_22 = zeros(1,numel(rad_dist_bins));
   all_taus(t).M_12 = zeros(1,numel(rad_dist_bins));
   all_taus(t).M_21 = zeros(1,numel(rad_dist_bins));

   %zeroing N counter for each time shift
   all_taus(t).N_11 = 0;
   all_taus(t).N_22 = 0;
   all_taus(t).N_12 = 0;
   all_taus(t).N_21 = 0;
end


inner_rads = rad_dist_bins(1:end-1); % inner radius for each ring
outer_rads = rad_dist_bins(2:end); %outer radius for each ring
mean_rads = (inner_rads+outer_rads)/2; %center point of ring
areas = pi*(outer_rads.^2 - inner_rads.^2); %area of each ring (in pixel^2)

%%
```

```
mask_rs = imresize(mask,1/dr); %resizing mask to calulate W(r)
% mask_rs has pixel size = dr, thus each bin of W_r = a correlation radii
I1 = double(mask_rs);
rmax = max_r/dr;
L1 = size(I1, 1)+rmax*4; % size of fft2 (for zero padding)
L2 = size(I1, 2)+rmax*4; % size of fft2 (for zero padding)
w_r = real(fftshift(ifft2(abs(fft2(mask_rs, L1, L2)).^2))); % Normalization
% for correct boundary conditions, w_r is the 2D autocorrelation of the mask

normalize = sum(sum(mask_rs)); %normalization factor for w_r
w_r_norm = w_r/normalize; %normalized 2D autocorrelation of mask
[W_r]  = radially_average(w_r_norm, rmax); %radially averaged 1D autocorrelation

%%

for j = 1:Nframes % going through all frames in user supplied data

   max_tau_j = min([max_tau Nframes-j]); % when within max_tau of last frame,
   % this is the maximum tau that can be used

   dts = 0:max_tau_j; % actual tau values
   dt_inds = dts + 1; % tau values for indexes

   %applying mask to data from frame j
   [m_data1] = apply_mask([data1(j).x data1(j).y],mask,k);
   [m_data2] = apply_mask([data2(j).x data2(j).y],mask,k);

   for t = dt_inds % going through all time lags (taus) with respect to frame j

      tshift = dts(t); % actual time lag to apply with respsect to frame j

      % data from frames thift after frame j
      DATA1_t = [data1(j+tshift).x data1(j+tshift).y];
      DATA2_t = [data2(j+tshift).x data2(j+tshift).y];

      %applying mask to data from frame j+tshift
      [m_data1_t] = apply_mask(DATA1_t,mask,k);
      [m_data2_t] = apply_mask(DATA2_t,mask,k);

      %computing the histogram M(r) and total number of radii N for channel 1
      %autocorrelation
      if ~isempty(m_data1) && ~isempty(m_data1_t) % if there are points in the mask
         num_combinations = size(m_data1_t,1)*size(m_data1,1); %total number of radii
         % between the two frames being correlated

        all_taus(t).N_11 = all_taus(t).N_11 + num_combinations;
        % keeping track of N, the total number of radii at each tau
```

```
        [all_taus(t).M_11] = tabulate_radii(m_data1,m_data1_t,rad_dist_bins,all_taus(t).M_11);
        % binning the radii between the two frames being correlated and
        % keeping track of the histogram of radii M(r) at each time shift
      end

      %computing the histogram M and total number of radii N for channel 2
      %autocorrelation
      if ~isempty(m_data2) && ~isempty(m_data2_t)
        num_combinations = size(m_data2_t,1)*size(m_data2,1);
        all_taus(t).N_22 = all_taus(t).N_22 + num_combinations;
        [all_taus(t).M_22] = tabulate_radii(m_data2,m_data2_t,rad_dist_bins,all_taus(t).M_22);
      end

      %computing the histogram M and total number of radii N for channel
      %1->2 cross-correlation
      if ~isempty(m_data1) && ~isempty(m_data2_t)
        num_combinations = size(m_data1,1)*size(m_data2_t,1);
        all_taus(t).N_12 = all_taus(t).N_12 + num_combinations;
        [all_taus(t).M_12] = tabulate_radii(m_data1,m_data2_t,rad_dist_bins,all_taus(t).M_12);
      end

      %computing the histogram M and total number of radii N for channel
      %2->1 cross-correlation
      if ~isempty(m_data2) && ~isempty(m_data1_t)
        num_combinations = size(m_data2,1)*size(m_data1_t,1);
        all_taus(t).N_21 = all_taus(t).N_21 + num_combinations;
        [all_taus(t).M_21] = tabulate_radii(m_data2,m_data1_t,rad_dist_bins,all_taus(t).M_21);
      end
    end
end
%%

colorz = jet(numel(all_dts));

figure

for t = all_dts

    if t~=1 %not plotting autocorrelation at 0 time shift
    subplot(2,2,1)
    C_11(t,:) = (all_taus(t).M_11(1:end-1)./(areas)./(W_r(1:numel(areas)))'*mask_area/(all_taus(t).N_11));
    dC_11(t,:) = sqrt((mask_area./areas./W_r(1:numel(areas))').^2.*(all_taus(t).M_11(1:end- …
1)./all_taus(t).N_11.^2).*(1+all_taus(t).M_11(1:end-1)./all_taus(t).N_11));
    errorbar(mean_rads*calib,C_11(t,:),dC_11(t,:),'s-‘, …
'MarkerFaceColor',colorz(t,:),'MarkerEdgeColor',colorz(t,:),'Color',colorz(t,:),'MarkerSize',2)
    hold on

    subplot(2,2,2)
    C_22(t,:) = (all_taus(t).M_22(1:end-1)./(areas)./(W_r(1:numel(areas)))'*mask_area/(all_taus(t).N_22));
```

```
    dC_22(t,:) = sqrt((mask_area./areas./W_r(1:numel(areas))').^2.*(all_taus(t).M_22(1:end- …
1)./all_taus(t).N_22.^2).*(1+all_taus(t).M_22(1:end-1)./all_taus(t).N_22));
    errorbar(mean_rads*calib,C_22(t,:),dC_22(t,:),'s-','MarkerFaceColor' ,colorz(t,:), 'MarkerEdgeColor' …
,colorz(t,:), 'Color',colorz(t,:),'MarkerSize',2)
    hold on
    end

    subplot(2,2,3)
    C_12(t,:) = (all_taus(t).M_12(1:end-1)./(areas)./(W_r(1:numel(areas)))'*mask_area/(all_taus(t).N_12));
    dC_12(t,:) = sqrt((mask_area./areas./W_r(1:numel(areas))').^2.*(all_taus(t).M_12(1:end- …
1)./all_taus(t).N_12.^2).*(1+all_taus(t).M_12(1:end-1)./all_taus(t).N_12));
    errorbar(mean_rads*calib,C_12(t,:),dC_12(t,:),'s-‘ …
,'MarkerFaceColor',colorz(t,:),'MarkerEdgeColor',colorz(t,:),'Color',colorz(t,:),'MarkerSize',2)
    hold on

    subplot(2,2,4)
    C_21(t,:) = (all_taus(t).M_21(1:end-1)./(areas)./(W_r(1:numel(areas)))'*mask_area/(all_taus(t).N_21));
    dC_21(t,:) = sqrt((mask_area./areas./W_r(1:numel(areas))').^2.*(all_taus(t).M_21(1:end- …
1)./all_taus(t).N_21.^2).*(1+all_taus(t).M_21(1:end-1)./all_taus(t).N_21));
    errorbar(mean_rads*calib,C_21(t,:),dC_21(t,:),'s-‘  …
,'MarkerFaceColor',colorz(t,:),'MarkerEdgeColor',colorz(t,:),'Color',colorz(t,:),'MarkerSize',2)
    hold on


end

subplot(2,2,1)
ylabel('G(r,\tau)')
xlabel('interparticle distance (nm)')
title('data1 autocorrelation','fontweight','bold')

subplot(2,2,2)
ylabel('G(r,\tau)')
xlabel('interparticle distance (nm)')
title('data2 autocorrelation','fontweight','bold')

subplot(2,2,3)
ylabel('C(r,\tau)')
xlabel('interparticle distance (nm)')
title('data1(t) x data2(t+\tau)','fontweight','bold')

subplot(2,2,4)
ylabel('C(r,\tau)')
xlabel('interparticle distance (nm)')
title('data2(t) x data1(t+\tau)','fontweight','bold')

if numel(all_dts)>1 % if there is autocorrelaiton data
    corrs.C_11 = C_11;
    corrs.dC_11 = dC_11;
```

```
   corrs.C_22 = C_22;
   corrs.dC_22 = dC_22;
end

corrs.C_12 = C_12;
corrs.dC_12 = dC_12;

corrs.C_21 = C_21;
corrs.dC_21 = dC_21;

params.radii = mean_rads*calib;
end %returns OUTPUT


function [m_data1] = apply_mask(data1,mask,k)

if isempty(data1); %returns empty if no data
   m_data1 = [];
return
end

X1 = data1(:,1); % x positions of data
Y1 = data1(:,2); % y positions of data

inders = 1:numel(X1); %numbered indexes of original data

NN = X1<size(mask,1); % getting rid of out of range indexes
WW = X1>0;
NM = Y1<size(mask,2);
WA = Y1>0;

RERE = NN.*WW.*NM.*WA;
loggg1 = logical(RERE); %logical indexes of data range of mask

if sum(loggg1) == 0; %if there is no data, return everything empty
   m_data1 = [];
return
end

subs = [ceil(double(X1(loggg1))) ceil(double(Y1(loggg1)))];
% the x and y positions that are within the range of the mask
% subs has removed particles that are out of range of the mask
% subs is ceiling in order to index directly into the mask

struct_inds = inders(loggg1);
%the numerical indexes of the original data in range of mask

ch1_inds = 1 + (subs(:,1)-1)*k(1) + (subs(:,2)-1)*k(2);
```

```
% getting 1D index from 2D subscripts subs [x y] using a
% workaround for sub2ind. sub2ind calls led to decreased performance

keep1 = mask(ch1_inds); % applying the logical mask to the data
inds_zeros = struct_inds'.*keep1; % indexes of all data within mask
% with zeros at indexes of data outside of mask

final_inds = inds_zeros(inds_zeros>0);
m_data1 = data1(final_inds,:); %the masked data1
end

function [vals] = radially_average(I, rmax)
if nargin<2, rmax = 100; end

% finds the center of the image I in each dimension
center1 = ceil((size(I, 1)+1)/2);
center2 = ceil((size(I, 2)+1)/2);

% sets the interval to calculate the radial average,
% centered on image I center pixel
range1 = center1-rmax:center1+rmax;
range2 = center2-rmax:center2+rmax;

% the values from the interval
zvals = I(range1, range2);

% creating a meshgrid from the interval
[xvals yvals] = meshgrid([-rmax:rmax],[-rmax:rmax]);

% transform to polar coordinates with v as image values
[theta,r,v] = cart2pol(xvals,yvals, zvals);

% arrange from small to large r values
Ar = reshape(r,1, numel(r));
[rr,ind] = sort(Ar);

% the corresponding image values
Avals = reshape(v,1, numel(v));
vv = Avals(ind);

% bin by radii and average values in bins
r = 0:floor(max(rr));
[n, bin] = histc(rr, r-.5);
vals = zeros(rmax+1,1);
for j = 1:rmax+1;%length(r),
   m = bin==j;
   n2 = sum(m);
   if n2==0, vals(j)=0; er(j)=0;
   else
```

```
      vals(j) = sum(m.*vv)/n2;
   end
end

end

function [histobam] = tabulate_radii(DATA1,DATA2,rad_dist_bins,histobam)

m_data1 = DATA1; %the masked data1
m_data2 = DATA2; %the masked data2



for k = 1: numel(m_data1(:,1)) %cycling through only data points within mask

      A = m_data1(k,:); %particle k's x and y position

      B = A(ones(size(m_data2,1),1),:); %repeat particle 1's position
      %to match size of data2
         diff = B - m_data2; %comparing particle k to all particles
         %in data2
         diff_squared = diff.*diff; % [x_diff^2 y_diff^2]
         r_diffs = (sqrt(diff_squared(:,1) + diff_squared(:,2)))';
         %radial difference values

[new_hists indexers2] = histc(r_diffs,rad_dist_bins); %binning by radius
% rad_dist_bins = radial distribution
%indexing the column indexes by k, (m_data1(k))
%amazingly, this index takes car of both channels indexing in an elegant
%way: all_radii_indexes(k,j) will return a vector containing which
%bins the radii between m_data(k) and m_data(j) ((NOTE m_data is actually
% N by 2 since it contains x and y values for position...)

histobam = histobam + new_hists; %adding the histograms for g(r)

end
end
```

References

1. Parham, P. *The Immune System, Fourth Edition*. (Garland Science, 2014).
2. Melchers, F. Checkpoints that control B cell development. *J. Clin. Invest.* **125,** 2203–2210 (2015).
3. Batista, F. D. & Harwood, N. E. The who, how and where of antigen presentation to B cells. *Nat. Rev. Immunol.* **9,** 15–27 (2009).
4. The cytoplasmic domains of immunoglobulin (Ig) alpha and Ig beta can independently induce the precursor B cell transition and allelic exclusion. *J. Exp. Med.* **182,** 1389–1394 (1995).
5. Gauthier, L., Rossi, B., Roux, F., Termine, E. & Schiff, C. Galectin-1 is a stromal cell ligand of the pre-B cell receptor (BCR) implicated in synapse formation between pre-B and stromal cells and in pre-BCR triggering. *Proc. Natl. Acad. Sci.* **99,** 13014 –13019 (2002).
6. Shaffer, A. L. & Schlissel, M. S. A truncated heavy chain protein relieves the requirement for surrogate light chains in early B cell development. *J. Immunol. Baltim. Md 1950* **159,** 1265–1275 (1997).
7. Monroe, J. G. ITAM-mediated tonic signalling through pre-BCR and BCR complexes. *Nat. Rev. Immunol.* **6,** 283–294 (2006).
8. Tiegs, S. L., Russell, D. M. & Nemazee, D. Receptor editing in self-reactive bone marrow B cells. *J. Exp. Med.* **177,** 1009–1020 (1993).
9. Pelanda, R. & Torres, R. M. Central B-cell tolerance: where selection begins. *Cold Spring Harb. Perspect. Biol.* **4,** a007146 (2012).
10. Goodnow, C. C., Adelstein, S. & Basten, A. The need for central and peripheral tolerance in the B cell repertoire. *Science* **248,** 1373–1379 (1990).
11. Wardemann, H. *et al.* Predominant Autoantibody Production by Early Human B Cell Precursors. *Science* **301,** 1374–1377 (2003).
12. Cambier, J. C., Gauld, S. B., Merrell, K. T. & Vilen, B. J. B-cell anergy: from transgenic models to naturally occurring anergic B cells? *Nat. Rev. Immunol.* **7,** 633–643 (2007).
13. Banchereau, J. & Steinman, R. M. Dendritic cells and the control of immunity. *Nature* **392,** 245–252 (1998).
14. Sasaki, Y., Casola, S., Kutok, J. L., Rajewsky, K. & Schmidt-Supprian, M. TNF family member B cell-activating factor (BAFF) receptor-dependent and -independent roles for BAFF in B cell physiology. *J. Immunol. Baltim. Md 1950* **173,** 2245–2252 (2004).
15. He, B. *et al.* Lymphoma B Cells Evade Apoptosis through the TNF Family Members BAFF/BLyS and APRIL. *J. Immunol.* **172,** 3268–3279 (2004).
16. Lam, K.-P., Kühn, R. & Rajewsky, K. In Vivo Ablation of Surface Immunoglobulin on Mature B Cells by Inducible Gene Targeting Results in Rapid Cell Death. *Cell* **90,** 1073–1083 (1997).

17. Kraus, M., Alimzhanov, M. B., Rajewsky, N. & Rajewsky, K. Survival of Resting Mature B Lymphocytes Depends on BCR Signaling via the Igα/β Heterodimer. *Cell* **117,** 787–800 (2004).
18. Delgado, P. *et al.* Essential function for the GTPase TC21 in homeostatic antigen receptor signaling. *Nat. Immunol.* **10,** 880–888 (2009).
19. Huppa, J. B. & Davis, M. M. T-cell-antigen recognition and the immunological synapse. *Nat. Rev. Immunol.* **3,** 973–983 (2003).
20. Harwood, N. E. & Batista, F. D. Early Events in B Cell Activation. *Annu. Rev. Immunol.* **28,** 185–210 (2010).
21. Batista, F. D., Iber, D. & Neuberger, M. S. B cells acquire antigen from target cells after synapse formation. *Nature* **411,** 489–494 (2001).
22. Dal Porto, J. M. *et al.* B cell antigen receptor signaling 101. *Mol. Immunol.* **41,** 599–613 (2004).
23. Gauld, S. B., Dal Porto, J. M. & Cambier, J. C. B cell antigen receptor signaling: roles in cell development and disease. *Science* **296,** 1641–1642 (2002).
24. Tsubata, T. Role of inhibitory BCR co-receptors in immunity. *Infect. Disord. Drug Targets* **12,** 181–190 (2012).
25. Flaswinkel, H. & Reth, M. Dual role of the tyrosine activation motif of the Ig-alpha protein during signal transduction via the B cell antigen receptor. *EMBO J.* **13,** 83–89 (1994).
26. Saijo, K. *et al.* Essential role of Src-family protein tyrosine kinases in NF-kappaB activation during B cell development. *Nat. Immunol.* **4,** 274–279 (2003).
27. Chan, V. W. F., Meng, F., Soriano, P., DeFranco, A. L. & Lowell, C. A. Characterization of the B Lymphocyte Populations in Lyn-Deficient Mice and the Role of Lyn in Signal Initiation and Down-Regulation. *Immunity* **7,** 69–81 (1997).
28. Johnson, S. A. *et al.* Phosphorylated immunoreceptor signaling motifs (ITAMs) exhibit unique abilities to bind and activate Lyn and Syk tyrosine kinases. *J. Immunol.* **155,** 4596–4603 (1995).
29. Kurosaki, T. *et al.* Role of the Syk autophosphorylation site and SH2 domains in B cell antigen receptor signaling. *J. Exp. Med.* **182,** 1815–1823 (1995).
30. Hutchcroft, J. E., Harrison, M. L. & Geahlen, R. L. Association of the 72-kDa protein-tyrosine kinase PTK72 with the B cell antigen receptor. *J. Biol. Chem.* **267,** 8613–8619 (1992).
31. Rowley, R. B., Burkhardt, A. L., Chao, H. G., Matsueda, G. R. & Bolen, J. B. Syk protein-tyrosine kinase is regulated by tyrosine-phosphorylated Ig alpha/Ig beta immunoreceptor tyrosine activation motif binding and autophosphorylation. *J. Biol. Chem.* **270,** 11590–11594 (1995).
32. Kabak, S. *et al.* The direct recruitment of BLNK to immunoglobulin alpha couples the B-cell antigen receptor to distal signaling pathways. *Mol. Cell. Biol.* **22,** 2524–2535 (2002).
33. Lemmon, M. A. Pleckstrin homology (PH) domains and phosphoinositides. *Biochem. Soc. Symp.* 81–93 (2007). doi:10.1042/BSS0740081
34. Tsukada, S., Simon, M. I., Witte, O. N. & Katz, A. Binding of beta gamma subunits of heterotrimeric G proteins to the PH domain of Bruton tyrosine kinase. *Proc. Natl. Acad. Sci. U. S. A.* **91,** 11256–11260 (1994).

35. Coggeshall, K. M. & Cambier, J. C. B cell activation. VIII. Membrane immunoglobulins transduce signals via activation of phosphatidylinositol hydrolysis. *J. Immunol. Baltim. Md 1950* **133,** 3382–3386 (1984).
36. Hogan, P. G., Lewis, R. S. & Rao, A. Molecular basis of calcium signaling in lymphocytes: STIM and ORAI. *Annu. Rev. Immunol.* **28,** 491–533 (2010).
37. Gallo, E. M., Canté-Barrett, K. & Crabtree, G. R. Lymphocyte calcium signaling from membrane to nucleus. *Nat. Immunol.* **7,** 25–32 (2006).
38. Nimmerjahn, F. & Ravetch, J. V. Fcγ receptors as regulators of immune responses. *Nat. Rev. Immunol.* **8,** 34–47 (2008).
39. Liu, W., Won Sohn, H., Tolar, P., Meckel, T. & Pierce, S. K. Antigen-Induced Oligomerization of the B Cell Receptor Is an Early Target of FcγRIIB Inhibition. *J. Immunol.* **184,** 1977 –1989 (2010).
40. Sohn, H. W., Pierce, S. K. & Tzeng, S.-J. Live cell imaging reveals that the inhibitory FcgammaRIIB destabilizes B cell receptor membrane-lipid interactions and blocks immune synapse formation. *J. Immunol. Baltim. Md 1950* **180,** 793–799 (2008).
41. Pritchard, N. R. & Smith, K. G. C. B cell inhibitory receptors and autoimmunity. *Immunology* **108,** 263–273 (2003).
42. Goodnow, C. C., Sprent, J., de St Groth, B. F. & Vinuesa, C. G. Cellular and genetic mechanisms of self tolerance and autoimmunity. *Nature* **435,** 590–597 (2005).
43. Nitschke, L. The role of CD22 and other inhibitory co-receptors in B-cell activation. *Curr. Opin. Immunol.* **17,** 290–297 (2005).
44. Depoil, D. *et al.* CD19 is essential for B cell activation by promoting B cell receptor-antigen microcluster formation in response to membrane-bound ligand. *Nat. Immunol.* **9,** 63–72 (2008).
45. Dawes, R. *et al.* Combinations of CD45 Isoforms Are Crucial for Immune Function and Disease. *J. Immunol.* **176,** 3417–3425 (2006).
46. Bleesing, J. J. H. & Fleisher, T. A. Human B cells express a CD45 isoform that is similar to murine B220 and is downregulated with acquisition of the memory B-cell marker CD27. *Cytometry B Clin. Cytom.* **51B,** 1–8 (2003).
47. Justement, L. B., Campbell, K. S., Chien, N. C. & Cambier, J. C. Regulation of B cell antigen receptor signal transduction and phosphorylation by CD45. *Science* **252,** 1839–1842 (1991).
48. Brown, V. K. *et al.* Multiple components of the B cell antigen receptor complex associate with the protein tyrosine phosphatase, CD45. *J. Biol. Chem.* **269,** 17238–17244 (1994).
49. Katagiri, T. *et al.* CD45 negatively regulates lyn activity by dephosphorylating both positive and negative regulatory tyrosine residues in immature B cells. *J. Immunol. Baltim. Md 1950* **163,** 1321–1326 (1999).
50. Hata, A., Sabe, H., Kurosaki, T., Takata, M. & Hanafusa, H. Functional analysis of Csk in signal transduction through the B-cell antigen receptor. *Mol. Cell. Biol.* **14,** 7306–7313 (1994).
51. Bromley, S. K. *et al.* The Immunological Synapse. *Annu. Rev. Immunol.* **19,** 375–396 (2001).
52. Fackler, O. T., Alcover, A. & Schwartz, O. Modulation of the immunological synapse: a key to HIV-1 pathogenesis? *Nat. Rev. Immunol.* **7,** 310–317 (2007).

53. Batista, F. D. & Neuberger, M. S. Affinity Dependence of the B Cell Response to Antigen: A Threshold, a Ceiling, and the Importance of Off-Rate. *Immunity* **8,** 751–759 (1998).
54. Davis, S. J. & van der Merwe, P. A. The kinetic-segregation model: TCR triggering and beyond. *Nat. Immunol.* **7,** 803–809 (2006).
55. Tolar, P., Hanna, J., Krueger, P. D. & Pierce, S. K. The Constant Region of the Membrane Immunoglobulin Mediates B Cell-Receptor Clustering and Signaling in Response to Membrane Antigens. *Immunity* **30,** 44–55 (2009).
56. Sigalov, A. B. & Hendricks, G. M. Membrane binding mode of intrinsically disordered cytoplasmic domains of T cell receptor signaling subunits depends on lipid composition. *Biochem. Biophys. Res. Commun.* **389,** 388–393 (2009).
57. Sigalov, A. B., Kim, W. M., Saline, M. & Stern, L. J. Intrinsically Disordered Cytoplasmic Domain of T Cell Receptor Zeta Chain Binds to the Nef Protein of Simian Immunodeficiency Virus Without a Disorder-to-Order Transition. *Biochemistry (Mosc.)* **47,** 12942–12944 (2008).
58. Rosenlöw, J., Isaksson, L., Mayzel, M., Lengqvist, J. & Orekhov, V. Y. Tyrosine Phosphorylation within the Intrinsically Disordered Cytosolic Domains of the B-Cell Receptor: An NMR-Based Structural Analysis. *PLoS ONE* **9,** e96199 (2014).
59. Sigalov, A. B. Unusual biophysics of immune signaling-related intrinsically disordered proteins. *Self/Nonself* **1,** 271–281 (2010).
60. Yang, J. & Reth, M. The dissociation activation model of B cell antigen receptor triggering. *FEBS Lett.* **584,** 4872–4877 (2010).
61. Packard, T. A. & Cambier, J. C. B lymphocyte antigen receptor signaling: initiation, amplification, and regulation. *F1000Prime Rep.* **5,** (2013).
62. van Meer, G., Stelzer, E. H., Wijnaendts-van-Resandt, R. W. & Simons, K. Sorting of sphingolipids in epithelial (Madin-Darby canine kidney) cells. *J. Cell Biol.* **105,** 1623–1635 (1987).
63. Coskun, Ü. & Simons, K. Membrane rafting: From apical sorting to phase segregation. *FEBS Lett.* **584,** 1685–1693 (2010).
64. The concept of lipid domains in membranes. *J. Cell Biol.* **94,** 1–6 (1982).
65. Diaz-Rohrer, B. B., Levental, K. R., Simons, K. & Levental, I. Membrane raft association is a determinant of plasma membrane localization. *Proc. Natl. Acad. Sci.* **111,** 8500–8505 (2014).
66. Alonso, M. A. & Millán, J. The role of lipid rafts in signalling and membrane trafficking in T lymphocytes. *J. Cell Sci.* **114,** 3957–3965 (2001).
67. Pierce, S. K. Lipid rafts and B-cell activation. *Nat. Rev. Immunol.* **2,** 96 (2002).
68. Holowka, D. *et al.* Lipid segregation and IgE receptor signaling: a decade of progress. *Biochim. Biophys. Acta* **1746,** 252–259 (2005).
69. Kabouridis, P. S. Lipid rafts in T cell receptor signalling. *Mol. Membr. Biol.* **23,** 49–57 (2006).
70. Hogue, I. B., Llewellyn, G. N. & Ono, A. Dynamic Association between HIV-1 Gag and Membrane Domains. *Mol. Biol. Int.* **2012,** e979765 (2012).
71. Bayer, E. M., Mongrand, S. & Tilsner, J. Specialized membrane domains of plasmodesmata, plant intercellular nanopores. *Front. Plant Sci.* **5,** (2014).
72. López, D. & Kolter, R. Functional microdomains in bacterial membranes. *Genes Dev.* **24,** 1893–1902 (2010).

73. Klose, C. *et al.* Yeast Lipids Can Phase-separate into Micrometer-scale Membrane Domains. *J. Biol. Chem.* **285,** 30224–30232 (2010).
74. Veatch, S. L. *et al.* Critical fluctuations in plasma membrane vesicles. *ACS Chem. Biol.* **3,** 287–293 (2008).
75. Veatch, S. L. & Keller, S. L. Organization in Lipid Membranes Containing Cholesterol. *Phys. Rev. Lett.* **89,** 268101 (2002).
76. Baumgart, T. *et al.* Large-scale fluid/fluid phase separation of proteins and lipids in giant plasma membrane vesicles. *Proc. Natl. Acad. Sci. U. S. A.* **104,** 3165–3170 (2007).
77. Gray, E., Karslake, J., Machta, B. B. & Veatch, S. L. Liquid General Anesthetics Lower Critical Temperatures in Plasma Membrane Vesicles. *Biophys. J.* **105,** 2751–2759 (2013).
78. Zhao, J., Wu, J. & Veatch, S. L. Adhesion Stabilizes Robust Lipid Heterogeneity in Supercritical Membranes at Physiological Temperature. *Biophys. J.* **104,** 825–834 (2013).
79. Singer, S. J. & Nicolson, G. L. The fluid mosaic model of the structure of cell membranes. *Science* **175,** 720–731 (1972).
80. Simons, K. & Van Meer, G. Lipid sorting in epithelial cells. *Biochemistry (Mosc.)* **27,** 6197–6202 (1988).
81. Generation of lipid polarity in intestinal epithelial (Caco-2) cells: sphingolipid synthesis in the Golgi complex and sorting before vesicular traffic to the plasma membrane. *J. Cell Biol.* **111,** 977–986 (1990).
82. Skibbens, J. E., Roth, M. G. & Matlin, K. S. Differential extractability of influenza virus hemagglutinin during intracellular transport in polarized epithelial cells and nonpolar fibroblasts. *J. Cell Biol.* **108,** 821–832 (1989).
83. Cheng, P. C., Dykstra, M. L., Mitchell, R. N. & Pierce, S. K. A role for lipid rafts in B cell antigen receptor signaling and antigen targeting. *J. Exp. Med.* **190,** 1549–1560 (1999).
84. Brown, D. A. & Rose, J. K. Sorting of GPI-anchored proteins to glycolipid-enriched membrane subdomains during transport to the apical cell surface. *Cell* **68,** 533–544 (1992).
85. Filipp, D. *et al.* Regulation of Fyn Through Translocation of Activated Lck into Lipid Rafts. *J. Exp. Med.* **197,** 1221–1227 (2003).
86. Moffett, S., Brown, D. A. & Linder, M. E. Lipid-dependent Targeting of G Proteins into Rafts. *J. Biol. Chem.* **275,** 2191–2198 (2000).
87. Chini, B. & Parenti, M. G-protein coupled receptors in lipid rafts and caveolae: how, when and why do they go there? *J. Mol. Endocrinol.* **32,** 325–338 (2004).
88. Zhu, M., Liu, Y., Koonpaew, S., Granillo, O. & Zhang, W. Positive and Negative Regulation of FcεRI-Mediated Signaling by the Adaptor Protein LAB/NTAL. *J. Exp. Med.* **200,** 991–1000 (2004).
89. Zhang, W., Trible, R. P. & Samelson, L. E. LAT Palmitoylation: Its Essential Role in Membrane Microdomain Targeting and Tyrosine Phosphorylation during T Cell Activation. *Immunity* **9,** 239–246 (1998).
90. Simons, K. & Toomre, D. Lipid rafts and signal transduction. *Nat Rev Mol Cell Biol* **1,** 31–39 (2000).
91. Simons, K. & Ikonen, E. Functional rafts in cell membranes. *Nature* **387,** 569–572 (1997).
92. Petrie, R. J., Schnetkamp, P. P., Patel, K. D., Awasthi-Kalia, M. & Deans, J. P. Transient translocation of the B cell receptor and Src homology 2 domain-containing inositol phosphatase to lipid rafts: evidence toward a role in calcium regulation. *J. Immunol. Baltim. Md 1950* **165,** 1220–1227 (2000).

93. Weintraub, B. C. *et al.* Entry of B cell receptor into signaling domains is inhibited in tolerant B cells. *J. Exp. Med.* **191,** 1443–1448 (2000).
94. Cheng, P. C., Brown, B. K., Song, W. & Pierce, S. K. Translocation of the B Cell Antigen Receptor into Lipid Rafts Reveals a Novel Step in Signaling. *J. Immunol.* **166,** 3693–3701 (2001).
95. Aman, M. J., Tosello-Trampont, A. C. & Ravichandran, K. Fc gamma RIIB1/SHIP-mediated inhibitory signaling in B cells involves lipid rafts. *J. Biol. Chem.* **276,** 46371–46378 (2001).
96. Kono, H. *et al.* FcγRIIB Ile232Thr transmembrane polymorphism associated with human systemic lupus erythematosus decreases affinity to lipid rafts and attenuates inhibitory effects on B cell receptor signaling. *Hum. Mol. Genet.* **14,** 2881 –2892 (2005).
97. Floto, R. A. *et al.* Loss of function of a lupus-associated Fc[gamma]RIIb polymorphism through exclusion from lipid rafts. *Nat Med* **11,** 1056–1058 (2005).
98. Flores-Borja, F., Kabouridis, P. S., Jury, E. C., Isenberg, D. A. & Mageed, R. A. Altered lipid raft-associated proximal signaling and translocation of CD45 tyrosine phosphatase in B lymphocytes from patients with systemic lupus erythematosus. *Arthritis Rheum.* **56,** 291–302 (2007).
99. Guo, B., Kato, R. M., Garcia-Lloret, M., Wahl, M. I. & Rawlings, D. J. Engagement of the Human Pre-B Cell Receptor Generates a Lipid Raft–Dependent Calcium Signaling Complex. *Immunity* **13,** 243–253 (2000).
100. Heerklotz, H. Triton Promotes Domain Formation in Lipid Raft Mixtures. *Biophys. J.* **83,** 2693–2701 (2002).
101. Lichtenberg, D., Goñi, F. M. & Heerklotz, H. Detergent-resistant membranes should not be identified with membrane rafts. *Trends Biochem. Sci.* **30,** 430–436 (2005).
102. Shogomori, H. & Brown, D. A. Use of detergents to study membrane rafts: the good, the bad, and the ugly. *Biol. Chem.* **384,** 1259–1263 (2003).
103. LIU, C., FALLEN, M. K., MILLER, H., UPADHYAYA, A. & SONG, W. The actin cytoskeleton coordinates the signal transduction and antigen processing functions of the B cell antigen receptor. *Front. Biol.* **8,** 475–485 (2013).
104. Gupta, N. & DeFranco, A. L. Visualizing lipid raft dynamics and early signaling events during antigen receptor-mediated B-lymphocyte activation. *Mol. Biol. Cell* **14,** 432–444 (2003).
105. Karnell, F. G., Brezski, R. J., King, L. B., Silverman, M. A. & Monroe, J. G. Membrane cholesterol content accounts for developmental differences in surface B cell receptor compartmentalization and signaling. *J. Biol. Chem.* **280,** 25621–25628 (2005).
106. Piston, D. W. & Kremers, G.-J. Fluorescent protein FRET: the good, the bad and the ugly. *Trends Biochem. Sci.* **32,** 407–414 (2007).
107. Sengupta, P., Holowka, D. & Baird, B. Fluorescence Resonance Energy Transfer between Lipid Probes Detects Nanoscopic Heterogeneity in the Plasma Membrane of Live Cells. *Biophys. J.* **92,** 3564–3574 (2007).
108. Pyenta, P. S., Holowka, D. & Baird, B. Cross-correlation analysis of inner-leaflet-anchored green fluorescent protein co-redistributed with IgE receptors and outer leaflet lipid raft components. *Biophys. J.* **80,** 2120–2132 (2001).

109. Sohn, H. W., Tolar, P. & Pierce, S. K. Membrane heterogeneities in the formation of B cell receptor-Lyn kinase microclusters and the immune synapse. *J. Cell Biol.* **182,** 367–379 (2008).
110. Sohn, H. W., Tolar, P., Jin, T. & Pierce, S. K. Fluorescence resonance energy transfer in living cells reveals dynamic membrane changes in the initiation of B cell signaling. *Proc. Natl. Acad. Sci.* **103,** 8143 –8148 (2006).
111. Lingwood, D. & Simons, K. Lipid Rafts As a Membrane-Organizing Principle. *Science* **327,** 46 –50 (2010).
112. Simons, K. & Gerl, M. J. Revitalizing membrane rafts: new tools and insights. *Nat. Rev. Mol. Cell Biol.* **11,** 688–699 (2010).
113. Qian, H., Sheetz, M. P. & Elson, E. L. Single particle tracking. Analysis of diffusion and flow in two-dimensional systems. *Biophys. J.* **60,** 910–921 (1991).
114. Saxton, M. J. & Jacobson, K. SINGLE-PARTICLE TRACKING:Applications to Membrane Dynamics. *Annu. Rev. Biophys. Biomol. Struct.* **26,** 373–399 (1997).
115. Kusumi, A. *et al.* Paradigm Shift of the Plasma Membrane Concept from the Two-Dimensional Continuum Fluid to the Partitioned Fluid: High-Speed Single-Molecule Tracking of Membrane Molecules. *Annu. Rev. Biophys. Biomol. Struct.* **34,** 351–378 (2005).
116. Mortensen, K. I., Churchman, L. S., Spudich, J. A. & Flyvbjerg, H. Optimized localization analysis for single-molecule tracking and super-resolution microscopy. *Nat. Methods* **7,** 377–381 (2010).
117. Schermelleh, L., Heintzmann, R. & Leonhardt, H. A guide to super-resolution fluorescence microscopy. *J. Cell Biol.* **190,** 165–175 (2010).
118. Rust, M. J., Bates, M. & Zhuang, X. Sub-diffraction-limit imaging by stochastic optical reconstruction microscopy (STORM). *Nat. Methods* **3,** 793–795 (2006).
119. Heilemann, M., Margeat, E., Kasper, R., Sauer, M. & Tinnefeld, P. Carbocyanine dyes as efficient reversible single-molecule optical switch. *J. Am. Chem. Soc.* **127,** 3801–3806 (2005).
120. Hess, S. T., Girirajan, T. P. K. & Mason, M. D. Ultra-High Resolution Imaging by Fluorescence Photoactivation Localization Microscopy. *Biophys. J.* **91,** 4258–4272 (2006).
121. Betzig, E. *et al.* Imaging intracellular fluorescent proteins at nanometer resolution. *Science* **313,** 1642–1645 (2006).
122. Dempsey, G. T. *et al.* Photoswitching Mechanism of Cyanine Dyes. *J. Am. Chem. Soc.* **131,** 18192–18193 (2009).
123. Heilemann, M., van de Linde, S., Mukherjee, A. & Sauer, M. Super-Resolution Imaging with Small Organic Fluorophores. *Angew. Chem. Int. Ed.* **48,** 6903–6908 (2009).
124. Zhang, M. *et al.* Rational design of true monomeric and bright photoactivatable fluorescent proteins. *Nat. Methods* **9,** 727–729 (2012).
125. Xu, K., Zhong, G. & Zhuang, X. Actin, spectrin and associated proteins form a periodic cytoskeletal structure in axons. *Science* **339,** (2013).
126. Grover, J. R. *et al.* Roles played by capsid-dependent induction of membrane curvature and Gag-ESCRT interactions in tetherin recruitment to HIV-1 assembly sites. *J. Virol.* JVI.03526–12 (2013). doi:10.1128/JVI.03526-12

127. Hell, S. W. & Wichmann, J. Breaking the diffraction resolution limit by stimulated emission: stimulated-emission-depletion fluorescence microscopy. *Opt. Lett.* **19,** 780 (1994).
128. Klar, T. A., Jakobs, S., Dyba, M., Egner, A. & Hell, S. W. Fluorescence microscopy with diffraction resolution barrier broken by stimulated emission. *Proc. Natl. Acad. Sci.* **97,** 8206–8210 (2000).
129. Bingen, P., Reuss, M., Engelhardt, J. & Hell, S. W. Parallelized STED fluorescence nanoscopy. *Opt. Express* **19,** 23716 (2011).
130. Mueller, V. *et al.* STED Nanoscopy Reveals Molecular Details of Cholesterol- and Cytoskeleton-Modulated Lipid Interactions in Living Cells. *Biophys. J.* **101,** 1651–1660 (2011).
131. Ringemann, C. *et al.* Exploring single-molecule dynamics with fluorescence nanoscopy. *New J. Phys.* **11,** 103054 (2009).
132. Scheiffele, P., Rietveld, A., Wilk, T. & Simons, K. Influenza Viruses Select Ordered Lipid Domains during Budding from the Plasma Membrane. *J. Biol. Chem.* **274,** 2038–2044 (1999).
133. Hess, S. T. *et al.* Dynamic clustered distribution of hemagglutinin resolved at 40 nm in living cell membranes discriminates between raft theories. *Proc. Natl. Acad. Sci. U. S. A.* **104,** 17370–17375 (2007).
134. Owen, D. M., Williamson, D. J., Magenau, A. & Gaus, K. Sub-resolution lipid domains exist in the plasma membrane and regulate protein diffusion and distribution. *Nat. Commun.* **3,** 1256 (2012).
135. Levental, I., Lingwood, D., Grzybek, M., Coskun, U. & Simons, K. Palmitoylation regulates raft affinity for the majority of integral raft proteins. *Proc. Natl. Acad. Sci. U. S. A.* **107,** 22050–22054 (2010).
136. Owen, D. M. *et al.* PALM imaging and cluster analysis of protein heterogeneity at the cell surface. *J. Biophotonics* **3,** 446–454 (2010).
137. Itano, M. S. *et al.* Super-Resolution Imaging of C-Type Lectin and Influenza Hemagglutinin Nanodomains on Plasma Membranes Using Blink Microscopy. *Biophys. J.* **102,** 1534–1542 (2012).
138. Veatch, S. L. *et al.* Correlation Functions Quantify Super-Resolution Images and Estimate Apparent Clustering Due to Over-Counting. *PLoS ONE* **7,** e31457 (2012).
139. Sengupta, P. *et al.* Probing protein heterogeneity in the plasma membrane using PALM and pair correlation analysis. *Nat. Methods* **8,** 969–975 (2011).
140. Fujiwara, T., Ritchie, K., Murakoshi, H., Jacobson, K. & Kusumi, A. Phospholipids undergo hop diffusion in compartmentalized cell membrane. *J. Cell Biol.* **157,** 1071–1082 (2002).
141. Dietrich, C., Yang, B., Fujiwara, T., Kusumi, A. & Jacobson, K. Relationship of lipid rafts to transient confinement zones detected by single particle tracking. *Biophys. J.* **82,** 274–284 (2002).
142. Kusumi, A., Ike, H., Nakada, C., Murase, K. & Fujiwara, T. Single-molecule tracking of membrane molecules: plasma membrane compartmentalization and dynamic assembly of raft-philic signaling molecules. *Semin. Immunol.* **17,** 3–21 (2005).
143. Eggeling, C. *et al.* Direct observation of the nanoscale dynamics of membrane lipids in a living cell. *Nature* **457,** 1159–1162 (2008).

144. Sezgin, E. *et al.* Partitioning, diffusion, and ligand binding of raft lipid analogs in model and cellular plasma membranes. *Biochim. Biophys. Acta* **1818,** 1777–1784 (2012).
145. Sahl, S. J., Leutenegger, M., Hilbert, M., Hell, S. W. & Eggeling, C. Fast molecular tracking maps nanoscale dynamics of plasma membrane lipids. *Proc. Natl. Acad. Sci. U. S. A.* **107,** 6829–6834 (2010).
146. Kenworthy, A. K., Petranova, N. & Edidin, M. High-Resolution FRET Microscopy of Cholera Toxin B-Subunit and GPI-Anchored Proteins in Cell Plasma Membranes. *Mol. Biol. Cell* **11,** 1645–1655 (2000).
147. Veatch, S. L., Soubias, O., Keller, S. L. & Gawrisch, K. Critical fluctuations in domain-forming lipid mixtures. *Proc. Natl. Acad. Sci.* **104,** 17650 –17655 (2007).
148. Gray, E. M. & Veatch, S. L. Cell Cycle Position Determines Critical Temperatures in Plasma Membrane Vesicles. *Biophys. J.* **108,** 86a–87a (2015).
149. J V Sengers & Sengers, and J. M. H. L. Thermodynamic Behavior of Fluids Near the Critical Point. *Annu. Rev. Phys. Chem.* **37,** 189–222 (1986).
150. Machta, B. B., Veatch, S. L. & Sethna, J. P. Critical Casimir Forces in Cellular Membranes. *Phys. Rev. Lett.* **109,** 138101 (2012).
151. Onsager, L. Crystal Statistics. I. A Two-Dimensional Model with an Order-Disorder Transition. *Phys. Rev.* **65,** 117–149 (1944).
152. Machta, B. B., Papanikolaou, S., Sethna, J. P. & Veatch, S. L. Minimal model of plasma membrane heterogeneity requires coupling cortical actin to criticality. *Biophys. J.* **100,** 1668–1677 (2011).
153. Ha, T. & Tinnefeld, P. Photophysics of fluorescent probes for single-molecule biophysics and super-resolution imaging. *Annu. Rev. Phys. Chem.* **63,** 595–617 (2012).
154. Dempsey, G. T., Vaughan, J. C., Chen, K. H., Bates, M. & Zhuang, X. Evaluation of fluorophores for optimal performance in localization-based super-resolution imaging. *Nat. Methods* **8,** 1027–1036 (2011).
155. Bock, H. *et al.* Two-color far-field fluorescence nanoscopy based on photoswitchable emitters. *Appl. Phys. B* **88,** 161–165 (2007).
156. Churchman, L. S., Ökten, Z., Rock, R. S., Dawson, J. F. & Spudich, J. A. Single molecule high-resolution colocalization of Cy3 and Cy5 attached to macromolecules measures intramolecular distances through time. *Proc. Natl. Acad. Sci. U. S. A.* **102,** 1419 –1423 (2005).
157. Shroff, H. *et al.* Dual-color superresolution imaging of genetically expressed probes within individual adhesion complexes. *Proc. Natl. Acad. Sci. U. S. A.* **104,** 20308–20313 (2007).
158. Subach, F. V. *et al.* Photoactivatable mCherry for high-resolution two-color fluorescence microscopy. *Nat. Methods* **6,** 153–159 (2009).
159. Patterson, G., Davidson, M., Manley, S. & Lippincott-Schwartz, J. Superresolution Imaging using Single-Molecule Localization. *Annu. Rev. Phys. Chem.* **61,** 345–367 (2010).
160. Bates, M., Huang, B., Dempsey, G. T. & Zhuang, X. Multicolor super-resolution imaging with photo-switchable fluorescent probes. *Science* **317,** 1749–1753 (2007).
161. Semrau, S., Holtzer, L., González-Gaitán, M. & Schmidt, T. Quantification of biological interactions with particle image cross-correlation spectroscopy (PICCS). *Biophys. J.* **100,** 1810–1818 (2011).
162. Veatch, S. L. *et al.* Correlation functions quantify super-resolution images and estimate apparent clustering due to over-counting. *PloS One* **7,** e31457 (2012).

163. Toplak, T. *et al.* STICCS reveals matrix-dependent adhesion slipping and gripping in migrating cells. *Biophys. J.* **103,** 1672–1682 (2012).
164. Dupont, A., Stirnnagel, K., Lindemann, D. & Lamb, D. C. Tracking Image Correlation: Combining Single-Particle Tracking and Image Correlation. *Biophys. J.* **104,** 2373–2382 (2013).
165. Stone, M. B. & Veatch, S. L. Far-Red Organic Fluorophores Contain a Fluorescent Impurity. *ChemPhysChem* **15,** 2240–2246 (2014).
166. McKinney, S. A., Murphy, C. S., Hazelwood, K. L., Davidson, M. W. & Looger, L. L. A bright and photostable photoconvertible fluorescent protein. *Nat Meth* **6,** 131–133 (2009).
167. Chibisov, A. K., Zakharova, G. V. & Görner, H. Photoprocesses of thiamonomethinecyanine monomers and dimers. *Phys. Chem. Chem. Phys.* **3,** 44–49 (2001).
168. Gruber, H. J. *et al.* Anomalous fluorescence enhancement of Cy3 and cy3.5 versus anomalous fluorescence loss of Cy5 and Cy7 upon covalent linking to IgG and noncovalent binding to avidin. *Bioconjug. Chem.* **11,** 696–704 (2000).
169. Berlier, J. E. *et al.* Quantitative comparison of long-wavelength Alexa Fluor dyes to Cy dyes: fluorescence of the dyes and their bioconjugates. *J. Histochem. Cytochem. Off. J. Histochem. Soc.* **51,** 1699–1712 (2003).
170. Subach, F. V., Patterson, G. H., Renz, M., Lippincott-Schwartz, J. & Verkhusha, V. V. Bright monomeric photoactivatable red fluorescent protein for two-color super-resolution sptPALM of live cells. *J. Am. Chem. Soc.* **132,** 6481–6491 (2010).
171. Gebhardt, J. C. M. *et al.* Single-molecule imaging of transcription factor binding to DNA in live mammalian cells. *Nat. Methods* **10,** 421–426 (2013).
172. Gahlmann, A. *et al.* Quantitative Multicolor Subdiffraction Imaging of Bacterial Protein Ultrastructures in Three Dimensions. *Nano Lett.* **13,** 987–993 (2013).
173. Gunewardene, M. S. *et al.* Superresolution Imaging of Multiple Fluorescent Proteins with Highly Overlapping Emission Spectra in Living Cells. *Biophys. J.* **101,** 1522–1528 (2011).
174. Izeddin, I. *et al.* Super-resolution dynamic imaging of dendritic spines using a low-affinity photoconvertible actin probe. *PloS One* **6,** e15611 (2011).
175. Wilmes, S. *et al.* Triple-color super-resolution imaging of live cells: resolving submicroscopic receptor organization in the plasma membrane. *Angew. Chem. Int. Ed Engl.* **51,** 4868–4871 (2012).
176. Endesfelder, U. *et al.* Chemically Induced Photoswitching of Fluorescent Probes—A General Concept for Super-Resolution Microscopy. *Molecules* **16,** 3106–3118 (2011).
177. Shim, S.-H. *et al.* Super-resolution fluorescence imaging of organelles in live cells with photoswitchable membrane probes. *Proc. Natl. Acad. Sci.* (2012). doi:10.1073/pnas.1201882109
178. Mennella, V. *et al.* Subdiffraction-resolution fluorescence microscopy reveals a domain of the centrosome critical for pericentriolar material organization. *Nat. Cell Biol.* **14,** 1159–1168 (2012).
179. Jones, S. A., Shim, S.-H., He, J. & Zhuang, X. Fast, three-dimensional super-resolution imaging of live cells. *Nat Meth* **8,** 499–505 (2011).
180. Nikić, I. *et al.* Minimal Tags for Rapid Dual-Color Live-Cell Labeling and Super-Resolution Microscopy. *Angew. Chem. Int. Ed.* **53,** 2245–2249 (2014).

181. Kim, D., Curthoys, N. M., Parent, M. T. & Hess, S. T. Bleed-through correction for rendering and correlation analysis in multi-colour localization microscopy. *J. Opt.* **15,** 094011 (2013).
182. Widengren, J. & Schwille, P. Characterization of Photoinduced Isomerization and Back-Isomerization of the Cyanine Dye Cy5 by Fluorescence Correlation Spectroscopy. *J. Phys. Chem. A* **104,** 6416–6428 (2000).
183. Muddana, H. S., Morgan, T. T., Adair, J. H. & Butler, P. J. Photophysics of Cy3-Encapsulated Calcium Phosphate Nanoparticles. *Nano Lett.* **9,** 1559–1566 (2009).
184. Prior, I. A., Muncke, C., Parton, R. G. & Hancock, J. F. Direct visualization of Ras proteins in spatially distinct cell surface microdomains. *J. Cell Biol.* **160,** 165–170 (2003).
185. Sherman, E. *et al.* Functional Nanoscale Organization of Signaling Molecules Downstream of the T Cell Antigen Receptor. *Immunity* **35,** 705–720 (2011).
186. Huang, F. *et al.* Video-rate nanoscopy using sCMOS camera-specific single-molecule localization algorithms. *Nat. Methods* **10,** 653–658 (2013).
187. Comeau, J. W. D., Costantino, S. & Wiseman, P. W. A Guide to Accurate Fluorescence Microscopy Colocalization Measurements. *Biophys. J.* **91,** 4611–4622 (2006).
188. Di Rienzo, C., Gratton, E., Beltram, F. & Cardarelli, F. Fast spatiotemporal correlation spectroscopy to determine protein lateral diffusion laws in live cell membranes. *Proc. Natl. Acad. Sci. U. S. A.* **110,** 12307–12312 (2013).
189. Veatch, S. L., Chiang, E. N., Sengupta, P., Holowka, D. A. & Baird, B. A. Quantitative Nano-Scale Analysis of IgE-FcεRI Clustering and Coupling to Early Signaling Proteins. *J. Phys. Chem. B* (2012). doi:10.1021/jp300197p
190. Annibale, P., Vanni, S., Scarselli, M., Rothlisberger, U. & Radenovic, A. Quantitative Photo Activated Localization Microscopy: Unraveling the Effects of Photoblinking. *PLoS ONE* **6,** e22678 (2011).
191. Coltharp, C., Kessler, R. P. & Xiao, J. Accurate construction of photoactivated localization microscopy (PALM) images for quantitative measurements. *PloS One* **7,** e51725 (2012).
192. Rollins, G. C., Shin, J. Y., Bustamante, C. & Pressé, S. Stochastic approach to the molecular counting problem in superresolution microscopy. *Proc. Natl. Acad. Sci.* **112,** E110–E118 (2015).
193. Lee, S.-H., Shin, J. Y., Lee, A. & Bustamante, C. Counting single photoactivatable fluorescent molecules by photoactivated localization microscopy (PALM). *Proc. Natl. Acad. Sci.* **109,** 17436–17441 (2012).
194. Mattila, P. K. *et al.* The Actin and Tetraspanin Networks Organize Receptor Nanoclusters to Regulate B Cell Receptor-Mediated Signaling. *Immunity* **38,** 461–474 (2013).
195. Cambi, A. & Lidke, D. S. *Cell Membrane Nanodomains: From Biochemistry to Nanoscopy*. (CRC Press, 2014).
196. Burkhardt, A. L., Brunswick, M., Bolen, J. B. & Mond, J. J. Anti-immunoglobulin stimulation of B lymphocytes activates src-related protein-tyrosine kinases. *Proc. Natl. Acad. Sci.* **88,** 7410–7414 (1991).
197. Campbell, M. A. & Sefton, B. M. Protein tyrosine phosphorylation is induced in murine B lymphocytes in response to stimulation with anti-immunoglobulin. *EMBO J.* **9,** 2125–2131 (1990).
198. Pierce, S. K. & Liu, W. The tipping points in the initiation of B cell signalling: how small changes make big differences. *Nat Rev Immunol* **10,** 767–777 (2010).

199. Semrau, S. & Schmidt, T. Particle Image Correlation Spectroscopy (PICS): Retrieving Nanometer-Scale Correlations from High-Density Single-Molecule Position Data. *Biophys. J.* **92,** 613–621 (2007).
200. Stone, M. B. & Veatch, S. L. Steady-state cross-correlations for live two-colour super-resolution localization data sets. *Nat. Commun.* **6,** (2015).
201. Gray, E., Karslake, J., Machta, B. B. & Veatch, S. L. Liquid General Anesthetics Lower Critical Temperatures in Plasma Membrane Vesicles. *Biophys. J.* **105,** 2751–2759 (2013).
202. Larson, D. R., Gosse, J. A., Holowka, D. A., Baird, B. A. & Webb, W. W. Temporally resolved interactions between antigen-stimulated IgE receptors and Lyn kinase on living cells. *J. Cell Biol.* **171,** 527 –536 (2005).
203. Shelby, S. A., Holowka, D., Baird, B. & Veatch, S. L. Distinct Stages of Stimulated FcεRI Receptor Clustering and Immobilization Are Identified through Superresolution Imaging. *Biophys. J.* **105,** 2343–2354 (2013).
204. Ganguly, S., Clayton, A. H. A. & Chattopadhyay, A. Fixation alters fluorescence lifetime and anisotropy of cells expressing EYFP-tagged serotonin1A receptor. *Biochem. Biophys. Res. Commun.* **405,** 234–237 (2011).
205. Gupta, N. & DeFranco, A. L. Lipid rafts and B cell signaling. *Semin. Cell Dev. Biol.* **18,** 616–626 (2007).
206. Stoddart, A. *et al.* Lipid Rafts Unite Signaling Cascades with Clathrin to Regulate BCR Internalization. *Immunity* **17,** 451–462 (2002).
207. Schmidt, C. *et al.* Signalling of the BCR is regulated by a lipid rafts-localised transcription factor, Bright. *EMBO J.* **28,** 711–724 (2009).
208. Katkere, B., Rosa, S., Caballero, A., Repasky, E. A. & Drake, J. R. Physiological-range temperature changes modulate cognate antigen processing and presentation mediated by lipid raft-restricted ubiquitinated B cell receptor molecules. *J. Immunol. Baltim. Md 1950* **185,** 5032–5039 (2010).
209. Mielenz, D. *et al.* Lipid rafts associate with intracellular B cell receptors and exhibit a B cell stage-specific protein composition. *J. Immunol. Baltim. Md 1950* **174,** 3508–3517 (2005).
210. Dykstra, M., Cherukuri, A., Sohn, H. W., Tzeng, S.-J. & Pierce, S. K. Location is everything: lipid rafts and immune cell signaling. *Annu. Rev. Immunol.* **21,** 457–481 (2003).
211. Janes, P. W., Ley, S. C. & Magee, A. I. Aggregation of Lipid Rafts Accompanies Signaling via the T Cell Antigen Receptor. *J. Cell Biol.* **147,** 447 –461 (1999).
212. Katsumata, O. *et al.* Association of FcgammaRII with low-density detergent-resistant membranes is important for cross-linking-dependent initiation of the tyrosine phosphorylation pathway and superoxide generation. *J. Immunol. Baltim. Md 1950* **167,** 5814–5823 (2001).
213. Munro, S. Lipid rafts: elusive or illusive? *Cell* **115,** 377–388 (2003).
214. Jacobson, K., Mouritsen, O. G. & Anderson, R. G. W. Lipid rafts: at a crossroad between cell biology and physics. *Nat. Cell Biol.* **9,** 7–14 (2007).
215. Shaw, A. S. Lipid rafts: now you see them, now you don't. *Nat. Immunol.* **7,** 1139–1142 (2006).
216. Huang, B., Bates, M. & Zhuang, X. Super resolution fluorescence microscopy. *Annu. Rev. Biochem.* **78,** 993–1016 (2009).

217. Owen, D. M., Magenau, A., Williamson, D. & Gaus, K. The lipid raft hypothesis revisited – New insights on raft composition and function from super-resolution fluorescence microscopy. *BioEssays* **34,** 739–747 (2012).
218. Takata, M. & Kurosaki, T. A role for Bruton's tyrosine kinase in B cell antigen receptor-mediated activation of phospholipase C-gamma 2. *J. Exp. Med.* **184,** 31–40 (1996).
219. Nishizuka, Y. Intracellular signaling by hydrolysis of phospholipids and activation of protein kinase C. *Science* **258,** 607–614 (1992).
220. Hanke, J. H. *et al.* Discovery of a Novel, Potent, and Src Family-selective Tyrosine Kinase Inhibitor STUDY OF Lck- AND FynT-DEPENDENT T CELL ACTIVATION. *J. Biol. Chem.* **271,** 695–701 (1996).
221. Kurosaki, T. *et al.* Syk activation by the Src-family tyrosine kinase in the B cell receptor signaling. *J. Exp. Med.* **179,** 1725–1729 (1994).
222. Hermiston, M. L., Xu, Z. & Weiss, A. CD45: A Critical Regulator of Signaling Thresholds in Immune Cells. *Annu. Rev. Immunol.* **21,** 107–137 (2003).
223. Shrivastava, P., Katagiri, T., Ogimoto, M., Mizuno, K. & Yakura, H. Dynamic regulation of Src-family kinases by CD45 in B cells. *Blood* **103,** 1425–1432 (2004).
224. Veatch, S. L. & Keller, S. L. Separation of Liquid Phases in Giant Vesicles of Ternary Mixtures of Phospholipids and Cholesterol. *Biophys. J.* **85,** 3074–3083 (2003).
225. Awasthi-Kalia, M., Schnetkamp, P. P. M. & Deans, J. P. Differential Effects of Filipin and Methyl-β-cyclodextrin on B Cell Receptor Signaling. *Biochem. Biophys. Res. Commun.* **287,** 77–82 (2001).
226. Petrie, R. J., Schnetkamp, P. P. M., Patel, K. D., Awasthi-Kalia, M. & Deans, J. P. Transient Translocation of the B Cell Receptor and Src Homology 2 Domain-Containing Inositol Phosphatase to Lipid Rafts: Evidence Toward a Role in Calcium Regulation. Available at: http://www.jimmunol.org. (Accessed: 1st September 2015)
227. Sohn, H. W., Tolar, P., Jin, T. & Pierce, S. K. Fluorescence resonance energy transfer in living cells reveals dynamic membrane changes in the initiation of B cell signaling. *Proc. Natl. Acad. Sci. U. S. A.* **103,** 8143–8148 (2006).
228. Hancock, J. F. Ras proteins: different signals from different locations. *Nat. Rev. Mol. Cell Biol.* **4,** 373–385 (2003).
229. Guan, X. M., Kobilka, T. S. & Kobilka, B. K. Enhancement of membrane insertion and function in a type IIIb membrane protein following introduction of a cleavable signal peptide. *J. Biol. Chem.* **267,** 21995–21998 (1992).
230. Olszowy, M. W., Leuchtmann, P. L., Veillette, A. & Shaw, A. S. Comparison of p56lck and p59fyn protein expression in thymocyte subsets, peripheral T cells, NK cells, and lymphoid cell lines. *J. Immunol. Baltim. Md 1950* **155,** 4236–4240 (1995).
231. Hui, E. & Vale, R. D. In vitro membrane reconstitution of the T-cell receptor proximal signaling network. *Nat. Struct. Mol. Biol.* **21,** 133–142 (2014).
232. Hartley, S. B. *et al.* Elimination from peripheral lymphoid tissues of self-reactive B lymphocytes recognizing membrane-bound antigens. *Nature* **353,** 765–769 (1991).
233. Treanor, B., Depoil, D., Bruckbauer, A. & Batista, F. D. Dynamic cortical actin remodeling by ERM proteins controls BCR microcluster organization and integrity. *J. Exp. Med.* **208,** 1055 –1068 (2011).
234. Saci, A. & Carpenter, C. L. RhoA GTPase Regulates B Cell Receptor Signaling. *Mol. Cell* **17,** 205–214 (2005).

235. Burbage, M. *et al.* Cdc42 is a key regulator of B cell differentiation and is required for antiviral humoral immunity. *J. Exp. Med.* **212,** 53–72 (2015).
236. Clarke, S. Protein Isoprenylation and Methylation at Carboxyl-Terminal Cysteine Residues. *Annu. Rev. Biochem.* **61,** 355–386 (1992).
237. Michaelson, D. *et al.* Differential Localization of Rho Gtpases in Live Cells Regulation by Hypervariable Regions and Rhogdi Binding. *J. Cell Biol.* **152,** 111–126 (2001).
238. Fleire, S. J. *et al.* B Cell Ligand Discrimination Through a Spreading and Contraction Response. *Science* **312,** 738 –741 (2006).
239. Chazeau, A. *et al.* Nanoscale segregation of actin nucleation and elongation factors determines dendritic spine protrusion. *EMBO J.* **33,** 2745–2764 (2014).
240. Kono, H. *et al.* FcgammaRIIB Ile232Thr transmembrane polymorphism associated with human systemic lupus erythematosus decreases affinity to lipid rafts and attenuates inhibitory effects on B cell receptor signaling. *Hum. Mol. Genet.* **14,** 2881–2892 (2005).
241. Kawabuchi, M. *et al.* Transmembrane phosphoprotein Cbp regulates the activities of Src-family tyrosine kinases. *Nature* **404,** 999–1003 (2000).
242. Yanagi, S. *et al.* CD45 modulates phosphorylation of both autophosphorylation and negative regulatory tyrosines of Lyn in B cells. *J. Biol. Chem.* **271,** 30487–30492 (1996).
243. Namba, T. *et al.* Pioneering axons regulate neuronal polarization in the developing cerebral cortex. *Neuron* **81,** 814–829 (2014).
244. Morgan, B. P., van den Berg, C. W., Davies, E. V., Hallett, M. B. & Horejsi, V. Cross-linking of CD59 and of other glycosyl phosphatidylinositol-anchored molecules on neutrophils triggers cell activation via tyrosine kinase. *Eur. J. Immunol.* **23,** 2841–2850 (1993).
245. Stefanová, I., Horejsí, V., Ansotegui, I. J., Knapp, W. & Stockinger, H. GPI-anchored cell-surface molecules complexed to protein tyrosine kinases. *Science* **254,** 1016–1019 (1991).
246. Suzuki, K. G. N. *et al.* GPI-anchored receptor clusters transiently recruit Lyn and Gα for temporary cluster immobilization and Lyn activation: single-molecule tracking study 1. *J. Cell Biol.* **177,** 717 –730 (2007).
247. Valensin, S. *et al.* F-actin dynamics control segregation of the TCR signaling cascade to clustered lipid rafts. *Eur. J. Immunol.* **32,** 435–446 (2002).
248. Seong, J. *et al.* Detection of focal adhesion kinase activation at membrane microdomains by fluorescence resonance energy transfer. *Nat. Commun.* **2,** 406 (2011).
249. Slade, M. S., Simmons, R. L., Yunis, E. & Greenberg, L. J. Immunodepression after major surgery in normal patients. *Surgery* **78,** 363–372 (1975).
250. Inada, T. *et al.* Effect of propofol and isoflurane anaesthesia on the immune response to surgery. *Anaesthesia* **59,** 954–959 (2004).
251. Visvabharathy, L., Xayarath, B., Weinberg, G., Shilling, R. A. & Freitag, N. E. Propofol Increases Host Susceptibility to Microbial Infection by Reducing Subpopulations of Mature Immune Effector Cells at Sites of Infection. *PLOS ONE* **10,** e0138043 (2015).
252. Krumholz, W., Endrass, J. & Hempelmann, G. Propofol inhibits phagocytosis and killing ofStaphylococcus aureus andEscherichia coli by polymorphonuclear leukocytesin vitro. *Can. J. Anaesth.* **41,** 446–449 (1994).
253. Taniguchi, T., Kanakura, H. & Yamamoto, K. Effects of posttreatment with propofol on mortality and cytokine responses to endotoxin-induced shock in rats*. *Crit. Care Med.* **30,** 904–907 (2002).

254. Hsu, B. G., Yang, F. L., Lee, R. P., Peng, T. C. & Chen, H. I. Effects of post-treatment with low-dose propofol on inflammatory responses to lipopolysaccharide-induced shock in conscious rats. *Clin. Exp. Pharmacol. Physiol.* **32,** 24–29 (2005).
255. Lorent, J. H. & Levental, I. Structural determinants of protein partitioning into ordered membrane domains and lipid rafts. *Chem. Phys. Lipids* **192,** 23–32 (2015).
256. Holowka, D., Sheets, E. D. & Baird, B. Interactions between Fc(epsilon)RI and lipid raft components are regulated by the actin cytoskeleton. *J. Cell Sci.* **113 (Pt 6),** 1009–1019 (2000).
257. Greicius, G. *et al.* Microvilli structures on B lymphocytes: inducible functional domains? *Int. Immunol.* **16,** 353–364 (2004).